QUANTUM EFFECTS OF THE MASSLESS SPIN ONE-HALF FIELD IN STATIC SPHERICALLY SYMMETRIC BLACK HOLE AND WORMHOLE SPACETIMES

By

William H. Hirsch

A Thesis Submitted to the Graduate Faculty of
WAKE FOREST UNIVERSITY
in Partial Fulfillment of the Requirements
for the Degree of
DOCTOR OF PHILOSOPHY
in the Department of Physics
August 2009
Winston-Salem, North Carolina

Approved By:
Eric Carlson, Ph.D., Advisor _____
Examining Committee:
Greg Cook, Ph.D. _____
Paul Anderson, Ph.D. _____
Richard Williams, Ph.D. _____
Stephen Robinson, Ph.D. _____

I give my utmost thanks to my thesis advisor Dr. Eric Carlson for his excellent teaching and the valuable discussions we shared in the progress of this work.

In addition, I would like to thank Dr. Paul Anderson for sharing his wealth of knowledge relevant to this field of research.

Also, I express my deepest gratitude to my wife Susan whose love, thoughtful conversations, and companionship have helped make this journey possible.

Lastly, I would like I share my most sincere thanks to all my family and friends for their support in this accomplishment.

William H. Hirsch

QUANTUM EFFECTS OF THE MASSLESS SPIN ONE-HALF FIELD IN STATIC SPHERICALLY SYMMETRIC BLACK HOLE AND WORMHOLE SPACETIMES

Thesis under the direction of Eric D. Carlson, Ph.D., Professor of Physics

The full renormalized stress-energy tensor for the massless spin one-half field is numerically computed on and outside the event horizon of an extreme Reissner-Nordström black hole and on and outside the throat of three static spherically symmetric Lorentzian wormhole spacetimes. The field and all spacetimes studied are in a zero temperature vacuum state. We treat the field quantum mechanically on a classical background spacetime governed by general relativity. The full stress-energy tensor is found to be finite and regular for all spacetimes. We make comparisons between the numerical calculation and the analytic approximation found by Groves *et al.* for the full stress-energy tensor. We find that the approximation is very poor in most cases, even getting the wrong sign for many components. For the extreme Reissner-Nordström black hole, divergences predicted by the analytic approximation of are shown to be nonexistent. Lastly, the results for the full stress-energy tensors for wormholes are analyzed in terms of an arbitrary renormalization parameter μ to see if the "exotic" energy condition needed to keep such an object from collapsing are met. No wormhole geometry studied is found to be a self-consistent solution when quantum fluctuations of the spin one-half field are considered. This is in contrast to the results found using the analytic approximation for the massless spin-one half field which predicts that one of the wormholes might have a self-consistent solution, since the stress-energy tensor found satisfies the exotic energy condition.

Contents

List of Figures

Chapter 1

Introduction

1.1 Motivation

The wonderfully successful Standard Model of particle physics incorporates three of the four fundamental forces into the common framework of quantum field theory (QFT). This includes the electromagnetic force in the form of quantum electrodynamics (QED), its extension to include the weak force in the form of the Glashow-Salam-Weinberg electroweak theory, and the strong nuclear force in the form of quantum chromodynamics (QCD).

The success of Feynman diagrams in the Standard Model prompted the application of such techniques to gravity, yet when constructing a QFT of the gravitational field, problems arose. First of all, the closed graviton loops, unlike closed loops in QED or QCD, yielded results that violated unitarity [1]. This was shown to be a consequence of general relativity's gauge independence by Feynman, DeWitt, Fadeev, and Popov [2, 3]. The unitarity of the theory was later fixed by the addition of additional Feynman diagrams containing a virtual particle called a ghost particle [4]. Covariant rules for calculating Feynman diagrams were developed by considering the mediator of the gravitation force to be a spin 2 particle (graviton), then as in QED or QCD a Lagrangian density for the gravitational field is written down and then the appropriate Feynman rules and diagrams were derived [3, 2, 4] (for a review see [5]). Researchers found that in attempting to implement these Feynman diagrams to calculate reaction rates or cross-sections, divergent integrals occur that, unlike those in QED, cannot be removed using a finite number of counterterms. This left QFT for gravity unrenormalizable.

The nonrenormalizability of a quantum field theory of gravity were not surprising because of the coupling constant present. Using dimensional analysis Weinberg [6] showed that if a field theory has a coupling constant of dimensions [mass]^d (in units where $\hbar = c = 1$) then at order N a Feynman diagram of the theory will have an associated momentum integral of the form

$$\int p^{A-Nd} dp, \tag{1.1}$$

where A is a positive parameter that depends only on what external legs are present and is independent of the number of loops in the diagram in question. It can be seen from Eq. (1.1) that higher order diagrams with $d < 0$ prove increasingly divergent. The coupling constant for gravity is Newton's constant, which can be written in the form $G = \hbar c M_p^{-2}$, where M_p is the Planck mass. The parameter d is therefore -2 for gravity and will cause a high order divergence in Eq. (1.1). This notion was solidified by the full calculations associated with such diagrams by others [7, 8, 9, 10, 11]. The QFT of gravity was therefore found unrenormalizable in particular because the dimensionality of G requires that an infinite number of counterterms be added to the gravitational Lagrangian. In contrast, renormalization can easily be achieved in QED, because the coupling constant is dimensionless, therefore only a finite number of counterterms must be added. The coupling constant in this case is the fine structure constant α. In cgs units it is

$$\alpha = \frac{e^2}{\hbar c}. \tag{1.2}$$

For an informative historical account of renormalization techniques in physics see [12].

Researchers have turned to many alternatives to glean information from the interplay of general relativity and QFT. Some of the more popular theories include string theory which has its proponents such as Greene [13] and skeptics including Smolin [14], a quantum theory of geometry or loop quantum gravity [15], braneworld physics [16], and supergravity [17]. For an informative discussion of the historical advancement and current state of a quantum theory of gravity see the review article by Ashtekar [18].

One can also utilize theories that do not attempt to quantize the gravitational field, but determine quantum effects near strong gravitational sources. Quantum field theory in curved spacetimes (QFTCS) is such a theory as well as the main research area of this work. One can calculate using QFTCS the effects gravitationally

strong sources have on fluctuating quantum fields. Specifically, we can access the quantum effects of a quantized field in the presence of a strong gravitational source by calculation of the expectation value of the full renormalized stress-energy tensor operator $\langle T_{\mu\nu} \rangle_{\rm ren}$ more simply referred to as the full stress-energy tensor. This quantity includes the effects from vacuum polarization and physical particles. The calculation of the full stress-energy tensor for the massless fermion field in the extreme Reissner-Nordström black hole spacetime (ERN) and three static spherically symmetric Lorentzian wormhole spacetimes is the main focus of this dissertation. Both the fields, and the ERN black hole are at zero temperature.

Classically, the way in which the geometry of a spacetime is affected by matter and energy is determined by the Einstein field equations [19]

$$G_{\mu\nu} = 8\pi T_{\mu\nu}. \tag{1.3}$$

We employ the sign conventions of Misner, Thorne, and Wheeler [19] and choose units such that $G = c = \hbar = k_b = 1$. In general, Einstein's field equations can be solved in one of two ways, the first being to choose a particular matter and energy distribution for $T_{\mu\nu}$ and then solve Eq. (1.3) for the metric tensor $g_{\mu\nu}$. Then we can determine the metric or square of the proper distance interval ds for a general curved spacetime

$$ds^2 = g_{\mu\nu} dx^\mu dx^\nu. \tag{1.4}$$

When one uses the stress-energy tensor for the vacuum ($T_{\mu\nu} = 0$) and assumes a static spherically symmetric uncharged solution, the Schwarzschild black hole metric is the result [19]. If this calculation assumes a charged black hole, the Reissner-Nordström (RN) black hole metric [20, 21, 19] results. The extreme Reissner-Nordström black hole is obtained from the RN metric when the charge Q and the black hole's mass M are equal [22]. The metrics for RN and ERN will be explicitly shown below.

A way in which the Einstein field equations can be solved while taking into account quantum effects is the loop expansion. The loop expansion is an expansion of the effective action for a given field in $\hbar$. For a free quantum field, this expansion is exact to first order in $\hbar$. The effective action is then varied with respect to the background metric g_{ab}. When the effective action for gravity is varied we obtain to order $\hbar^0$ the Einstein tensor G_{ab} and to order $\hbar$ the quantum stress-energy tensor for gravitons $\langle T_{ab} \rangle_{\rm graviton}$. Next, when we vary the effective action for the matter fields, we find at

order $\hbar^0$ the classical stress-energy tensor T^c_{ab} and to order $\hbar$ the quantum contribution $\langle T_{ab}\rangle_{\rm matter}$. After varying the total effective action of gravity and the matter fields together, we arrive at

$$G_{ab} = 8\pi \left(T^c_{ab} + \langle T_{ab}\rangle_{\rm graviton} + \langle T_{ab}\rangle_{\rm matter}\right), \tag{1.5}$$

where the terms $\langle T_{ab}\rangle_{\rm graviton}$ and $\langle T_{ab}\rangle_{\rm matter}$ are of order $\hbar$. Now we expand g_{ab} in powers of $\hbar$ such that

$$g_{ab} = \gamma_{ab} + \delta g_{ab}, \tag{1.6}$$

where the $\hbar$ in the second term on the right has been set equal to one. Substitution of Eq. (1.6) into G_{ab} in Eq. (1.5) and expanding to first order in $\hbar$ yields

$$G_{ab}\left[\gamma\right] + \delta G_{ab}\left[\gamma, \delta g\right] = 8\pi \left(T^c_{ab} + \langle T_{ab}\rangle_{\rm graviton} + \langle T_{ab}\rangle_{\rm matter}\right). \tag{1.7}$$

Separating the terms of order $\hbar^0$ and $\hbar$ in Eq. (1.7) respectively leads to the two equations

$$G_{ab}\left[\gamma\right] = 8\pi T^c_{ab}, \tag{1.8}$$

$$\delta G_{ab}\left[\gamma, \delta g\right] = 8\pi \left(\langle T_{ab}\rangle_{\rm graviton} + \langle T_{ab}\rangle_{\rm matter}\right). \tag{1.9}$$

One now solves Eq. (1.8) for γ to obtain the classical metric tensor for ERN. Next, to find the perturbation of the metric caused by quantum effects, we solve Eq. (1.9) for δg after substitution of γ. For the loop expansion method to be valid as one goes to higher orders in $\hbar$, the terms on the left hand side of Eq. (1.9) must get smaller. This means that if the quantum contribution is too large the loop approximation breaks down, as discussed next.

We have calculated $\langle T_{ab}\rangle_{\rm matter}$ for the massless fermion field for the ERN black hole in this work. What we have not done though is calculate $\langle T_{ab}\rangle_{\rm graviton}$ or attempted to solve Eq. (1.9) for the perturbation of the metric. It is possible that the form of $\langle T_{ab}\rangle_{\rm matter}$ alone may suggest a breakdown of the loop expansion. The loop expansion may break down if a component of the quantum stress-energy tensor in an orthonormal frame diverges on the event horizon. In such a case, it is possible that this type of black hole solution to the semi-classical equations above would not exist. A fine example of this possible exclusion is the prediction of a divergence in one component of the stress-energy tensor, related to the energy density observed by

a freely falling observer, near the event horizon of the ERN black hole by various analytic approximations for the massless spin 0, 1/2, and 1 fields [23, 26, 33].

Another way in which the Einstein field equations may be solved classically is to first construct an interesting spacetime metric and then determine what matter source is responsible for that respective geometry. This is precisely the method used in the classic paper by Morris and Thorne [27] that reinvigorated the study of wormholes in the 1980's. They found that wormholes require matter satisfying "exotic" energy conditions to create their geometry. This matter is named exotic because it must satisfy an energy condition which violates the weak energy condition.

This exotic energy suggests that perhaps fluctuating quantum fields could be the source of the wormhole metric, since quantum effects can violate the weak energy condition. One's ideal goal would be to find a self-consistent solution to the semi-classical Einstein field equations

$$G_{ab}[g] = 8\pi N \langle T_{ab} \rangle \tag{1.10}$$

for a given wormhole in the context of the large N expansion [28], where N is the number of fields. Notice that T^c_{ab} is absent from Eq. (1.10), because it is zero for wormholes. We would like to find a solution where the quantum fluctuations caused by curved spacetime $\langle T_{\mu\nu} \rangle$ actually create the wormhole metric we want.

The large N approximation assumes that the number of specific fields (fermions for example) is large and therefore completely dominate the quantum contribution to the stress-energy tensor. Quantum effects can be as large as classical effects as long as N is large enough, although as mentioned above $T^c_{ab} = 0$ for wormholes. One can then ignore the quantum effects of the graviton field. To determine a self-consistent solution, one attempts to find a metric such that when the terms in Eq. (1.10) are calculated both sides of the equation are equal. Employing this approach does not make sense for the ERN black hole, since the primary source or curvature is a background classical electric field. To solve Eq. (1.10), one could first choose a metric g_{ab} and then compute $\langle T_{ab} \rangle$ to see if a self-consistent solution could be found. We have not done this, but our calculations of $\langle T_{ab} \rangle$ for wormholes could be used as a starting point for searching for self-consistent wormholes. For example, if $\langle T_{ab} \rangle$ satisfies the exotic energy conditions required for a wormhole, a self-consistent solution may be possible. A self-consistent wormhole solution using an analytic approximation for

the full stress-energy tensor for a massive scalar field has been found by Hochberg, Popov, and Sushkov [29]. The current work, however, casts doubt on the validity of this type of analytic approximation, because as we will see, at least for fermions, this approximation is often substantially in error.

We utilize numerical techniques to compute the full stress-energy tensor and an analytic approximation for the full stress-energy tensor using a method developed by Groves *et al.* [30]. This method for finding the analytic approximation has been shown to be equivalent to that of Frolov and Zel'nikov [23]. We have chosen to utilize a massless non-interacting fermion field for our calculations. The reason we use fermions is because they make up a substantial majority of the types of known fundamental particles in nature. All the elementary particles that make up the Standard Model are fermions except the gauge particles, which are spin-one bosons, and the scalar Higgs boson. In addition, most of the work that has been done in this research area has been for physically unrealistic scalar fields. We perform the calculation for the massless field, since this reduces the number of parameters by one, and for a very small mass black hole or wormhole all known particles are close to massless. This is because the mass is unimportant on scales much smaller than the Compton wavelength of the particle [31]. Lastly, we are assuming non-interacting fields which implies the fields are not electrically charged, because otherwise the calculations become much too difficult. Our method should therefore be viewed as an approximation to this more realistic case.

Let's discuss relevant calculations of the full stress-energy tensor that have been performed for the ERN black hole. A full calculation by Trivedi [32] in two dimensions for the massless scalar field finds one component of $\langle T_{\mu\nu} \rangle$ related to the energy density observed by a freely falling observer passing through the event horizon of a ERN black hole divergent. Anderson, Hiscock, and Loranz calculated full numerical results for the stress-energy tensor for the massless spin-0 field near an ERN black hole finding all components of $\langle T_{\mu\nu} \rangle$ regular on the event horizon [26]. Lastly, Carlson *et al.* [33] performed calculations of the full stress-energy tensor for the fermion field in Schwarzschild, RN, and ERN spacetimes.

To our knowledge no previous computation of the full stress-energy tensor has been completed for any quantized field in any wormhole spacetime, although some other

calculations have been done as discussed below. Taylor, Hiscock, and Anderson [34], used an analytic approximation for the minimally and conformally coupled scalar field to determine the stress-energy tensor for the same wormhole metrics studied in this work. They found the stress-energy tensor failed to satisfy the exotic energy condition for minimal and covariant coupling. In contrast, the analytic approximation for $\langle T_{\mu\nu} \rangle$ derived in [34] for the massless scalar field was used to find the first self-consistent wormhole solution to the semi-classical Einstein equations [29]. A self-consistent solution was also found for the massive scalar field with non conformal coupling around a short-throat flat space wormhole using zeta renormalization [35]. Lastly, the analytic approximation found by Popov [36] for $\langle T_{\mu\nu} \rangle$ utilizing the arbitrary mass scalar field predicts that the wormholes studied here meet the exotic energy conditions for some values of the scalar coupling constant. The work of Popov was built upon the results of Barcelo and Visser [37] in which a general argument is made that the scalar field should be able to satisfy the exotic energy conditions for a general spherically symmetric wormhole spacetime for some value of the scalar coupling constant.

Our results for ERN show all components of $\langle T_{\mu\nu} \rangle$ to be finite on the event horizon, in contrast to the results of Frolov and Zel'nikov [23] and Trivedi [32] mentioned above. In addition, we find the analytic approximation to be very poor, not even getting the proper sign of the components of the stress-tensor correct far from the horizon. Our results were also found to be in agreement with a massless fermion field calculation for Reissner-Nordström spacetime in the limit $Q/M \to 1$ found in Carlson *et al.* [33]. Lastly, our results for ERN indicate that all components of the full stress-energy tensor fall off as M/r^5 at large distances from the horizon.

We find that none of the full stress-energy tensors calculated for the three wormholes studied have the form necessary to imply a self-consistent solution in the presence of a massless spin one-half field. Also, we again find that the analytic approximation yields poor results except in the proximal Schwarzschild case, where it yields the same qualitative behavior at least and it does get the sign correct for the energy density near the throat. In addition, the analytic approximation correctly predicts that two of the three wormholes are not self-consistent.

The rest of this introduction will contain first a review of general spherically symmetric metrics, and then a section on classical static spherically symmetric black

holes and Lorentzian wormholes. Then we shall review the field of quantum field theory in curved space including special historical results.

In Chapter 2 we shall discuss the theory behind performing quantum field theory calculations with fermions in flat spacetime and then curved spacetime. This will lead to the way in which we will calculate the full stress-energy tensor. In Chapter 3 we present the numerical techniques utilized in computing the full stress-energy tensor, leading to results for the extreme Reissner-Nordström spacetime and three static spherically symmetric wormholes. Lastly, in Chapter 4 we review our main results.

1.2 General spherically symmetric metrics

To obtain a general stationary spherically symmetric metric, consider first a spacetime in coordinates (t, r, θ, ϕ) that is time independent and isotropic. To preserve these conditions, the time and radial components must not depend on either angular coordinate. Also, the only differentials in for θ and ϕ should be $d\theta^2$ and $d\phi^2$ to preserve spherical symmetry of the metric. This follows from the fact that for reflections across the cartesian xy and xz planes we have $d\theta \to -d\theta$ and $d\phi \to -d\phi$ respectively, so provided we stay at fixed r and t the metric must look like the surface of a sphere

$$R^2(r)(d\theta^2 + \sin^2\theta d\phi^2). \tag{1.11}$$

One can therefore write the most general static spherically symmetric metric as [38]

$$ds^2 = -f(r)dt^2 + h(r)dr^2 + 2j(r)drdt + R^2(r)(d\theta^2 + \sin^2\theta d\phi^2), \tag{1.12}$$

in which the functions of r are called metric functions.

Let us at this point rewrite Eq. (1.12) in a cleaner form through a series of substitutions. First assume $R(r)$ is continuous and single valued, and therefore has an inverse. We are free to redefine the radial coordinate and choose $r' = R(r)$ and hence $r = R^{-1}(r')$. Next write Eq. (1.12) in terms of r', redefine the new metric functions with their previous names, and rename r' as r, so that

$$ds^2 = -f(r)dt^2 + h(r)dr^2 + 2j(r)drdt + r^2(d\theta^2 + \sin^2\theta d\phi^2). \tag{1.13}$$

One would like to remove the off diagonal terms in the metric. To do so, shift time in a radial dependent way,

$$t = t' + F(r), \tag{1.14}$$

and recast Eq. (1.13) as

$$ds^2 = -f dt'^2 + 2\left(j - f\frac{dF}{dr}\right) dr dt' + \left(h + 2j\frac{dF}{dr} - f\left(\frac{dF}{dr}\right)^2\right) dr^2 + r^2(d\theta^2 + \sin^2\theta d\phi^2), \tag{1.15}$$

where explicit r dependance has been suppressed. If we pick $F(r)$ such that $f(r)F'(r) = j(r)$, namely

$$F(r) = \int \frac{j(r)}{f(r)} dr, \tag{1.16}$$

then the off diagonal term in Eq. (1.15) will vanish:

$$ds^2 = -f dt'^2 + \left(h + \frac{j^2}{f}\right) dr^2 + r^2(d\theta^2 + \sin^2\theta d\phi^2). \tag{1.17}$$

All that remains to do is to rename t' as t and $h + j^2/f$ as h to arrive at the standard form of a static spherically symmetric spacetime metric

$$ds^2 = -f(r)dt^2 + h(r)dr^2 + r^2 d\Omega^2, \tag{1.18}$$

in which $d\Omega^2 = d\theta^2 + \sin^2\theta d\phi^2$. All spacetimes studied in this work are of the form of Eq. (1.18).

1.2.1 Reissner-Nordström and the extreme Reissner-Nordström black hole

When one takes as a source for the Einstein field equations the stress-energy tensor of a radial electric field with no matter present outside the event horizon and assumes a static, spherically symmetric gravitational field, the metric for a Reissner-Nordström black hole is obtained. The metric functions have the form

$$f(r) = h^{-1}(r) = \left(1 - \frac{2M}{r} + \frac{Q^2}{r^2}\right), \tag{1.19}$$

in which M and Q are the total mass and total charge respectively of the black hole as measured by an observer at a distance $r \gg 2M$. The charge of the RN black hole lies in the range $0 \leq |Q| \leq M$. The limits of the charge lead to the electrically

neutral Schwarzschild black hole ($Q = 0$) and the extreme Reissner-Nordström black hole ($|Q| = M$).

An interesting property of all black hole spacetimes is that they contain an event horizon. The event horizon represents a boundary at $r = r_+$ that once crossed cannot be crossed again. Consider a radially directed light beam originating at r_+ aimed at an observer at infinity. Recalling that the path of a light beam has zero proper time, $d\tau^2 = -ds^2 = 0$, the amount of coordinate time that it takes light from $r = r_+$ to reach an observer at $r = R$ is

$$t = \int_{r_+}^{R} \sqrt{\frac{h(r)}{f(r)}}\, dr = \int_{r_+}^{R} \frac{dr}{f(r)}. \tag{1.20}$$

When $f(r)$ vanishes linearly or more strongly at $r = r_+$, the time for the light beam to escape from r_+ will diverge, so the light never reaches the distant observer. This suggests the existence of an event horizon at $r = r_+$. Solving $f(r_+) = 0$ for r_+, we find that the RN spacetime has an event horizon at

$$r_+ = M + \sqrt{M^2 - Q^2}. \tag{1.21}$$

It is interesting to note that for $|Q| > M$ the spacetime contains no event horizon and a physical singularity at $r = 0$. Such an object has been given the name "naked singularity" and is thought by some researchers to not exist in nature since it would contradict Penrose's Cosmic Censorship hypothesis that states that a singularity is always surrounded by an event horizon [39]. The ERN black hole has the explicit metric functions

$$f(r) = h^{-1}(r) = \left(1 - \frac{M}{r}\right)^2, \tag{1.22}$$

and therefore an event horizon at $r_+ = M$.

We can also assign a value to the acceleration due to gravity at a black hole's event horizon. This is called the surface gravity [19]

$$\kappa = \lim_{r \to r_+} \frac{1}{2} \frac{f'(r)}{\sqrt{f(r)h(r)}}. \tag{1.23}$$

It is interesting to note that the ERN black hole has a surface gravity of zero for our later discussion of the Hawking effect. It therefore makes an interesting testing ground for QFTCS calculations. In addition, the ERN black hole has received a lot of attention in braneworld physics, (see for example [40, 41]) and string theorists have calculated their entropy in agreement with Hawking's semiclassical result [42].

1.2.2 Wormholes

Most simply put, a wormhole is a short-cut or tunnel through space and time. The name wormhole was coined by John Archibald Wheeler in 1957. It can be thought of as a warping of space to traverse a very large distance in an otherwise impossibly small amount of local time as measured by the traveller. Although wormholes are speculative, a very large body of serious research has accumulated on the subject over the years. This spans basically the entire past century starting with Einstein and Rosen's early paper on the Einstein-Rosen bridge [43] that consists of a Schwarzschild black hole connected to a white hole. The hypothesis was that one way travel could occur into the black hole and then out of the white hole. This configuration was shown later to be unstable by Wheeler and Fuller, with the bridge connecting the two spacetimes collapsing before any signal could pass through [44]. In the 1950's Wheeler utilized a wormhole as the framework for a new elementary entity called a geon that was a bundle of electromagnetic waves held together by gravity [45]. After the work of Wheeler, the field of wormholes mostly lay dormant until a paper by Morris and Thorne reinvigorated the field in the 1980's [27]. They explored what kind of energy and matter would be required to hold open a wormhole metric satisfying Einstein's field equations and if such a wormhole could be made safely traversable by people in a finite amount of time. Two reviews of the field include the text by Visser [46] covering up to 1995, and the comprehensive review article by Lobo [47] completed in 2008.

The simplest Lorentzian manifold one can consider for a wormhole is a bridge connecting two asymptotically flat spacetimes that contain no horizons. This is in constrast to work that has been done with Euclidean wormholes [46]. The metric for a static, spherically symmetric wormhole spacetime can be parameterized in the Morris and Thorne form as [27]

$$ds^2 = -e^{2\phi_{1,2}(r)}dt^2 + \left(1 - \frac{b_{1,2}(r)}{r}\right)^{-1} dr^2 + r^2 d\Omega^2, \tag{1.24}$$

where we can make a connection to the metric functions employed in Eq. (1.18) by

$$\begin{aligned} f(r) &= e^{2\phi_{1,2}(r)}, \\ h(r) &= \left(1 - \frac{b_{1,2}(r)}{r}\right)^{-1}. \end{aligned} \tag{1.25}$$

In Eq. (1.24), $\phi(r)$ is called the redshift function, because it determines the gravitational redshift of an observer travelling through the wormhole, and $b(r)$ is the shape function, since it is directly related to the spatial shape of the wormhole. The coordinate r lies in the range $r_0 \leq r < \infty$ with $2\pi r_0$ being the circumference of a circle centered on the wormhole's throat at $r = r_0$ which we assume to be the minimum radius. This metric includes two coordinate patches designated 1 and 2 joined at the throat. For simplicity in this work we assume that time runs at the same rate in both universes and that both openings have the same spatial shape. In other words, the two mouths of the wormhole are the same spatially and temporally. Mathematically this corresponds to

$$\phi_1(r) = \phi_2(r), \tag{1.26}$$

$$b_1(r) = b_2(r); \tag{1.27}$$

hence the subscripts 1 and 2 will be dropped, and we will refer to the functions as simply $\phi(r)$ and $b(r)$.

The metric appearing in Eq. (1.24) does not represent a wormhole unless we place some restrictions on the functions $\phi(r)$ and $b(r)$. The spatial geometry must become flat as r approaches infinity; therefore, the following limits must hold [27]

$$\lim_{r\to\infty} \phi(r) = 0, \tag{1.28}$$

$$\lim_{r\to\infty} \frac{b(r)}{r} = 0. \tag{1.29}$$

Also, a wormhole, unlike a black hole, will not have an event horizon or a singularity. One cannot assign a Hawking temperature to a wormhole, since it does not have a horizon. We are simply assuming that the universes in which the wormholes reside are at zero temperature. To ensure there is not an event horizon at $r = r_0$, we must demand that

$$\lim_{r\to r_0} \phi(r) > -\infty. \tag{1.30}$$

The function $b(r)$ must be chosen so that

$$\lim_{r\to r_0} h(r) = \infty. \tag{1.31}$$

Then the wormhole has a throat at $r = r_0$. Equation (1.31) implies that

$$b(r_0) = r_0, \tag{1.32}$$

however we want $h(r)$ to be positive and finite as r increases above r_0 which requires

$$\frac{d}{dr}\left(\frac{1}{h(r)}\right)_{r=r_0} > 0. \tag{1.33}$$

Substituting the metric function for $h(r)$ from Eq. (1.25) into Eq. (1.33), and making use of Eq. (1.32) leads to the inequality

$$\frac{1}{r_0^2} - \frac{b'(r_0)}{r_0^2} > 0, \tag{1.34}$$

where a prime denotes a derivative with respect to r. We will now rewrite Eq. 1.34 in terms of the energy density and radial tension at $r = r_0$. Utilizing the classical Einstein field equations, the energy density at the throat is then expressed as

$$\begin{aligned} \rho_0 &= -\frac{1}{8\pi} G_t{}^t = -T_t{}^t \\ &= \frac{1}{8\pi}\frac{b'(r_0)}{r_0^2}, \end{aligned} \tag{1.35}$$

and the radial tension at the throat is written

$$\begin{aligned} \tau_0 &= -\frac{1}{8\pi} G_r{}^r = -T_r{}^r \\ &= \frac{1}{8\pi}\frac{1}{r_0^2}, \end{aligned} \tag{1.36}$$

Substitution of these results into Eq. (1.34) yields the inequality for the "exotic" energy condition first derived by Morris and Thorne [27]

$$\tau_0 - \rho_0 > 0, \tag{1.37}$$

and we must also have

$$\tau_0 > 0, \tag{1.38}$$

to satisfy Eq. (1.36). Eq. (1.37) is simultaneously troublesome and interesting. Classical matter can easily satisfy $\tau_0 > 0$, but can not satisfy $\tau_0 - \rho_0 > 0$ since such matter would violate the weak energy condition. The weak energy condition states that the local energy density as viewed by any observer is non-negative so that [48]

$$T_{\mu\nu}U^\mu U^\nu \geq 0, \tag{1.39}$$

for all time like vectors U^μ. Equation (1.37) implies that an observer travelling though the wormhole's throat with a radial velocity close to the speed of light ($\gamma \gg 1$) will

observe negative energy density. To demonstrate this effect, we project the stress-energy tensor onto the orthonormal frame attached to the observer yielding, from her point of view, an energy density of [27]

$$\rho' = \gamma^2(\rho_0 - \tau_0) + \tau_0. \tag{1.40}$$

Since ρ' must be positive in the limit $\gamma \to \infty$, we conclude that

$$\rho_0 - \tau_0 \geq 0. \tag{1.41}$$

This stress-energy tensor required by a wormhole violates the weak energy condition; therefore, matter that satisfies Eq. (1.37) has been given the name exotic.

No known classical matter or fields satisfy the exotic energy condition; therefore, wormholes are a perfect candidate for studying quantum effects, since such exotic energies have been encountered in QFTCS calculations like the Casimir effect. One goal of this research is to determine if quantum fluctuations of the massless spin one-half field will generate a full stress-energy tensor that satisfies the exotic energy condition in Eq. (1.37). The full stress-energy tensor then might be a self-consistent solution to the semi-classical Einstein field equations. None of the wormholes studied in this work were found to simultaneously satisfy the exotic energy inequality and the condition $\tau_0 > 0$; therefore, no self-consistent solution was found.

1.2.3 Specific wormhole metrics analyzed in this work

Recall the form of a wormhole spacetime from Eq. (1.24)

$$ds^2 = -e^{2\phi(r)}dt^2 + \left(1 - \frac{b(r)}{r}\right)^{-1} dr^2 + r^2 d\Omega^2. \tag{1.42}$$

A wormhole spacetime can be found by choosing the functions $b(r)$ and $\phi(r)$ such that the formerly mentioned criteria are met. We will here enumerate the wormholes studied numerically as part of this work. The reader should note that all wormholes metrics classically satisfy the exotic energy condition (Eq. (1.37)) by construction. Also, in 1996 Ford and Roman showed using QFT that inequalities can be derived that severely limit the size of a wormhole [49]. They showed that either the wormhole must be Planck scale or the exotic matter must be confined to a thin shell around the wormhole's throat.

The first wormhole considered is called the zero tidal force wormhole [27], since an observer passing through the hole would experience no tidal forces. It has the form

$$\text{case 1:} \quad b(r) = r_0 \qquad \text{and} \qquad \phi(r) = 0. \tag{1.43}$$

This wormhole has the same spatial form as a Schwarzschild black hole and classically it has no background energy density via Eq. (1.35). The second wormhole considered is the so called "simple wormhole" [27]. It was given as part of a final exam on general relativity at Caltech. Its relevant functions are

$$\text{case 2:} \quad b(r) = \frac{r_0^2}{r} \qquad \text{and} \qquad \phi(r) = 0. \tag{1.44}$$

It is interesting to note that this wormhole has energy density equal in magnitude to its radial tension, but of opposite sign. Lastly we numerically compute the full stress-energy tensor for the proximal Schwarzschild wormhole [27]:

$$\text{case 3:} \quad b(r) = r_0 \qquad \text{and} \qquad \phi(r) = \frac{1}{2}\ln\left(1 - \frac{r_0}{r} + \frac{\epsilon r_0^2}{r^2}\right), \tag{1.45}$$

where ϵ is a small positive constant. An observer a large distance form this wormhole would be unable to distinguish it from a Schwarzschild black hole. As the observer moves closer to the throat, she would realize that the object is actually a wormhole with no event horizon because of the small ϵ term.

1.3 Quantum field theory in curved spacetimes

The main objective of QFTCS calculations lies in determining what new physical effects occur when doing QFT on a curved spacetime background or a flat spacetime background with nontrivial topology. Most of the prominent phenomena were first summarized in the article by DeWitt [50]. Much of the formalism of QFTCS can be found in the standard text by Birrell and Davies [31], and two more focused texts by Wald [51], and Fulling [52]. Also a few good recent review articles exist [53, 54]. The new physical processes found utilizing QFTCS methods include the creation of particles in expanding cosmological spacetimes such as in the Robertson-Walker space [55, 31] or de Sitter universes [56, 57, 58, 59]. The famous Hawking radiation effect [60] was another achievement of QFTCS. The Hawking effect predicts that a

black hole will produce particles near its event horizon, via conversion of gravitational energy into mass, causing it to slowly evaporate at an emission temperature of [31]

$$T_H = \left(\frac{\hbar c^3}{8\pi G k_b}\right)\kappa, \tag{1.46}$$

where κ is the surface gravity of the black hole, and k_B is Boltzmann's constant. Recall that for the ERN black hole $\kappa = 0$. This means that the ERN black hole has a zero temperature and therefore the Hawking effect does not occur. There still is particle production though in the ERN spacetime due to the Schwinger effect [61] if the fields are charged. This effect predicts particle production in a vacuum near a strong electric field. Therefore the only way to not have particle production near a ERN wormhole is to consider electrically neutral fields, which we have done.

Of note are also a few important flat spacetime phenomena, namely the Casimir and Unruh effects. The first of these, first predicted by Casimir in 1948 [62], is that two flat, parallel, neutral conducting plates in a vacuum attract one another by a small attractive force proportional to the inverse fourth power of the distance that separates them. If one calculates the total energy between the plates it is found to be negative

$$E = -\frac{\hbar c \pi^2}{720 x^3} A. \tag{1.47}$$

In Eq. (1.47), x and A are the distance between the plates and their area respectively. This implies that there is an attractive force between the plates

$$F = -\frac{dE}{dx} = -\frac{\hbar c \pi^2}{240 x^4} A, \tag{1.48}$$

and negative energy density

$$\rho = -\frac{\hbar c \pi^2}{720 x^4}. \tag{1.49}$$

We see that the vacuum energy with the plates present is less than the energy without the plates. Physically, it is the observable part of zero point energy created by the electromagnetic field. The Casimir force has been tested experimentally, first at Philips Laboratories where it was verified to within 15% of the predicted result [63], and more recently to within 5% [64]. The negative Casimir energy density is therefore experimental evidence that the weak energy condition, Eq. (1.39), can be violated by quantum effects. Experimental results such as these give credibility to QFTCS

calculations, since the Casimir effect can also be derived using QFTCS techniques in flat space with boundaries (see [65, 66]). This lends credence to the validity of QFTCS calculations.

Lastly, the still experimentally unconfirmed Unruh effect [67] shows that observers undergoing constant acceleration will observe black body radiation of temperature

$$T = \frac{a\hbar}{2\pi c k_B}, \tag{1.50}$$

where a is the proper acceleration. This effect occurs because the vacuum of a non-inertial observer is different than that of an inertial observer when treated in the formalism of QFTCS, though the vacua are related by a Bogolubov transformation [68]. Another consequence of the Unruh effect is that the decay rate for accelerating particles will differ from their inertial counterparts [69].

Quantum field theory in curved space calculations are performed by using gravity as a classical background field; namely, the metric of Einstein's general theory of relativity. The matter fields are then quantized upon that background akin to what one would do in flat space. The hope is that the results of such a theory approximate an actual theory of quantum gravity. This concept is similar to the now dated implementation of the electromagnetic field as a classical background field interacting with matter as an approximation for what we now call QED [70].

The goal of this research is to calculate and subsequently study the expectation value of the full renormalized stress-energy tensor operator, $\langle T_{\mu\nu} \rangle_{\text{ren}}$, for the massless fermion field for a variety of static spherically symmetric spacetimes. This full stress-energy tensor can be used as a tool to approximate quantum effects in the presence of strong gravitational fields. Like many objects in QFT, it is divergent and must be renormalized to get a finite, physical result. This was done by the method of point splitting in the time direction [71, 72], but the details will be left to a later section. Furthermore, we must specify a state for our quantum fields. We have chosen a zero temperature vacuum state.

When the specific quantum state utilized respects the symmetries of a static spherically symmetric metric, $\langle T_\mu{}^\nu \rangle$ has only diagonal nonzero components of the form

$$\langle T_\mu{}^\nu \rangle = \begin{pmatrix} -\rho & 0 & 0 & 0 \\ 0 & P_r & 0 & 0 \\ 0 & 0 & P & 0 \\ 0 & 0 & 0 & P \end{pmatrix}. \tag{1.51}$$

The quantities ρ and P_r in Eq. (1.51) designate the energy density and radial pressure. The pressures in the θ and ϕ directions are equal, so $\langle T_\theta{}^\theta \rangle = \langle T_\phi{}^\phi \rangle = P$. In addition, the negative of each pressure is a tension in the appropriate direction. For example, the radial tension is $\tau = -P_r$. We will always express our numerical results for the full stress-energy tensor with one index up and one down. This is nearly the same as working in an orthonormal basis (designated by indices with a hat: $\hat{\mu}$). The orthonormal basis corresponds to having a locally flat coordinate system. It is straightforward to show that when the metric tensor is diagonal,

$$\langle T_{\hat{t}\hat{t}} \rangle = -\langle T_t{}^t \rangle, \tag{1.52}$$

$$\langle T_{\hat{i}\hat{j}} \rangle = \langle T_i{}^j \rangle, \tag{1.53}$$

where Latin indices run from 1 to 3. As we will see in more detail in Chapter 2, the stress-energy tensor is first written in terms of the quantized fermion field. Then the expectation value of $\langle T_{\mu\nu} \rangle$ is taken. The expectation value of the stress-energy tensor operator is used because otherwise we cannot assign meaning to Einstein's equations, because the Einstein curvature tensor $G_{\mu\nu}$ on the left hand side is not an operator. This choice leads to the semiclassical Einstein equations in Eq. (1.10).

The quantum contribution to the stress-energy tensor was shown by Wald [73], to be physically meaningful and unique up to a local conserved tensor if it satisfied a number of postulates. The first is that the quantum stress-energy tensor should be covariantly conserved,

$$\nabla_\nu \langle T_\mu{}^\nu \rangle = 0, \tag{1.54}$$

to be an appropriate choice for the right side of Eq. (1.10). The second and third are that the stress-energy tensor should not violate causality and yield standard results for off-diagonal elements. In addition, the calculated stress-energy tensor should lead to standard results in Minkowski space.

Chapter 2

Fermion fields in flat and curved spacetimes

2.1 Flat spacetime

Before considering the formalism for finding the full stress-energy tensor we should first take a look at fermion fields in flat spacetime and then curved spacetime. In this way we will work our way up to the relevant expressions for our numerical computations. Consider the Lagrangian density for the fermion field ψ in Minkowski space

$$\mathcal{L} = \frac{1}{2} i \left(\overline{\psi} \gamma^{\alpha} \partial_{\alpha} \psi - \partial_{\alpha} \overline{\psi} \gamma^{\alpha} \psi \right) - m \overline{\psi} \psi. \tag{2.1}$$

In Eq. (2.1), m is the mass of the field, $\overline{\psi}$ is the Dirac adjoint of ψ, namely

$$\overline{\psi} = \psi^{\dagger} \gamma^{0}, \tag{2.2}$$

γ^{α} are the Dirac matrices [74], and $\partial_{\alpha} \equiv \frac{\partial}{\partial x_{\alpha}}$. The reader should note that we utilize the Dirac representation for the these matrices. The Dirac matrices are

$$\gamma^{0} = \begin{pmatrix} \mathbf{1} & \mathbf{0} \\ \mathbf{0} & \mathbf{-1} \end{pmatrix}, \qquad \gamma^{i} = \begin{pmatrix} \mathbf{0} & \sigma_{i} \\ -\sigma_{i} & \mathbf{0} \end{pmatrix}, \qquad i = 1, 2, 3, \tag{2.3}$$

in which the σ_i are the Pauli spin matrices

$$\sigma_1 = \begin{pmatrix} 0 & 1 \\ 1 & 0 \end{pmatrix}, \qquad \sigma_2 = \begin{pmatrix} 0 & -i \\ i & 0 \end{pmatrix}, \qquad \sigma_3 = \begin{pmatrix} 1 & 0 \\ 0 & -1 \end{pmatrix}. \tag{2.4}$$

The Dirac matrices are 4×4 matrices; therefore, $\mathbf{0}$ and $\mathbf{1}$ represent the 2×2 trivial and identity matrices respectively. The Dirac matrices also satisfy the anti-commutation relations

$$\{\gamma^{\alpha}, \gamma^{\beta}\} = -2\eta^{\alpha\beta}. \tag{2.5}$$

Here $\eta^{\alpha\beta}$ is the metric for Minkowski space. In Cartesian coordinates it has the form

$$\eta^{\alpha\beta} = \begin{pmatrix} -1 & 0 & 0 & 0 \\ 0 & 1 & 0 & 0 \\ 0 & 0 & 1 & 0 \\ 0 & 0 & 0 & 1 \end{pmatrix}. \tag{2.6}$$

Variation of the action,

$$\mathcal{S} = \int \mathcal{L} d^4x, \tag{2.7}$$

with respect to $\bar{\psi}$ yields the familiar Dirac equation for fermions in flat space

$$i\gamma^\alpha \partial_\alpha \psi - m\psi = 0. \tag{2.8}$$

The Dirac equation has both positive and negative energy solutions which look like [74]

$$\begin{aligned} \psi(x) &= u_k(\vec{x}) e^{-i\omega_k t}, \\ \psi(x) &= v_k(\vec{x}) e^{i\omega_k t}, \end{aligned} \tag{2.9}$$

where k is an index labelling a complete, orthonormal set of wave functions. When we quantize the field, the u_k solutions will correspond to particles, and the v_k solutions to anti-particles.

The fact that the fields ψ are spinor fields deserves some attention. A spinor transforms under a coordinate change very differently than a tensor does. A rank 1 covariant tensor (covector) transforms according to the Lorentz transformation rule

$$W'_\alpha(x') = \Lambda_\alpha{}^\mu W_\mu(x), \tag{2.10}$$

where

$$\Lambda^\mu{}_\alpha = \frac{\partial x^\mu}{\partial x'^\alpha}. \tag{2.11}$$

In flat space a Lorentz transformation infinitesimally close to the identity can be written

$$\Lambda^\alpha{}_\beta = \delta^\alpha_\beta + \omega^\alpha{}_\beta, \tag{2.12}$$

where $\omega_{\alpha\beta}$ is an arbitrary anti-symmetric tensor and δ^α_β is the usual Kronecker tensor. The transformation rule for a spinor can be written as

$$\psi'(x) = \mathcal{D}(\Lambda)\psi(x). \tag{2.13}$$

$\mathcal{D}(\Lambda)$ is a spinor representation of the Lorentz group, $(\frac{1}{2},0)\oplus(0,\frac{1}{2})$, in which $\oplus$ is the direct sum symbol. It is a matrix with the explicit form

$$\mathcal{D}(\Lambda) = \mathbf{1} + \frac{1}{2}\omega_{\alpha\beta}\sigma^{\alpha\beta}. \tag{2.14}$$

The anti-symmetric tensors $\sigma^{\alpha\beta}$ are the generators of the Lorentz group and are constant matrices. They are found from the requirement that the $\mathcal{D}$'s satisfy the group multiplication rule

$$\mathcal{D}(\Lambda_1)\mathcal{D}(\Lambda_2) = \mathcal{D}(\Lambda_1\Lambda_2). \tag{2.15}$$

This group multiplication rule demands that the following anti-commutation rule is true for the fermion field

$$\left[\sigma^{\alpha\beta}, \sigma^{\gamma\delta}\right] = \eta^{\gamma\beta}\sigma^{\alpha\delta} - \eta^{\gamma\alpha}\sigma^{\beta\delta} + \eta^{\delta\beta}\sigma^{\gamma\alpha} - \eta^{\delta\alpha}\sigma^{\gamma\beta}. \tag{2.16}$$

We can satisfy Eq. (2.16) if the generators of the group are

$$\sigma^{\alpha\beta} = -\frac{1}{4}\left[\gamma^{\alpha}, \gamma^{\beta}\right]. \tag{2.17}$$

We now wish to promote our field ψ to a quantum operator which satisfies the canonical anti-commutation relations [74]

$$\left\{\psi(t;\vec{x}), \bar{\psi}(t;\vec{x'})\right\} = \gamma^0\delta^3(\vec{x}-\vec{x'}). \tag{2.18}$$

This equation is satisfied if we write

$$\psi(x) = \sum_k \left(u_k(\vec{x})e^{-i\omega_k t}a_k + v_k(\vec{x})e^{i\omega_k t}b_k^{\dagger}\right), \tag{2.19}$$

where a_k and b_k ($a_k^{\dagger}$ and $b_k^{\dagger}$) are annihilation operators (creation operators) for particles and anti-particles whose anti-commutators vanish, except for the combinations

$$\{a_k, a_{k'}^{\dagger}\} = \{b_k, b_{k'}^{\dagger}\} = \delta_{k,k'}. \tag{2.20}$$

The operator ψ will then satisfy the Dirac equation,

$$i\gamma^{\alpha}\partial_{\alpha}\psi - m\psi = 0. \tag{2.21}$$

Now that we have introduced fermions we should review Green's functions in flat space. They are of prime interest to our later curved space methods. Finding S_F

(or equivalently, S_E) will prove sufficient to determine the expectation value of the full stress-energy tensor $\langle T_{\mu\nu}\rangle$. These functions are used in QFT much like in electromagnetism to solve field equations that are subject to certain boundary conditions. The Green's function describes a wave at point x produced by a source at x' and is written in terms of products of ψ in a vacuum state. This makes it suitable for the zero temperature state calculations we are interested in. The unrenormalized stress-energy tensor can be written in terms of the Green's functions. Then renormalization is achieved by the method of point splitting which is easily handled in this formalism by separating the points in the Green's function. The Green's function for the fermion field, $S_F(x,x')$, also known as the spinor Feynman propagator, is defined as the expectation value of the time ordered product of the operators ψ and $\bar{\psi}$

$$\begin{aligned} S_F(x,x') &= -i\langle 0|T\left[\psi(x)\bar{\psi}(x')\right]|0\rangle \\ &= -i\theta(t-t')\langle 0|\psi(x)\bar{\psi}(x')|0\rangle + i\theta(t'-t)\langle 0|\bar{\psi}(x')\psi(x)|0\rangle\ . \end{aligned} \tag{2.22}$$

We are taking a tensor product in the second term in Eq. (2.22); therefore, it is a 4×4 matrix. The function $\theta(x)$ is the Heaviside step function. It has the property

$$\theta(x) = \begin{cases} 0, & x<0 \\ 1, & x>0. \end{cases} \tag{2.23}$$

Now we shall determine the form of Eq. (2.8) for $S_F(x,x')$ by acting upon it with the operator $(i\gamma^\alpha\partial_\alpha - m)$

$$\begin{aligned} (i\gamma^\alpha\partial_\alpha - m)\,S_F(x,x') &= -i\,(i\gamma^\alpha\partial_\alpha - m)\left[\theta(t-t')\langle 0|\psi(x)\bar{\psi}(x')|0\rangle\right] \\ &+ i\,(i\gamma^\alpha\partial_\alpha - m)\left[\theta(t'-t)\langle 0|\bar{\psi}(x')\psi(x)\right]|0\rangle. \end{aligned} \tag{2.24}$$

The derivative operators can act on either the Heaviside functions or the expectation values in which case we can use Eq. (2.21) for simplifications. This leads us to

$$\begin{aligned} (i\gamma^\alpha\partial_\alpha - m)\,S_F(x,x') &= -i\left[i\gamma^\alpha\partial_\alpha\theta(t-t')\right]\langle 0|\psi(x)\bar{\psi}(x')|0\rangle \\ &+ i\left[i\gamma^\alpha\partial_\alpha\theta(t'-t)\right]\langle 0|\bar{\psi}(x')\psi(x)|0\rangle. \end{aligned} \tag{2.25}$$

The derivative of the Heaviside function is the Dirac delta function, and we get an extra minus sign from the second term. This is because its argument is switched. We now have

$$
\begin{aligned}
\left(i\gamma^{\alpha}\partial_{\alpha} - m\right) S_F(x,x') &= \gamma^0\delta(t-t')\langle 0|\psi(x)\bar{\psi}(x')|0\rangle + \gamma^0\delta(t'-t)\langle 0|\bar{\psi}(x')\psi(x)|0\rangle \\
&= \gamma^0\delta(t-t')\langle 0|\left\{\psi(x),\bar{\psi}(x')\right\}|0\rangle \\
&= \delta^4(x-x'), \qquad (2.26)
\end{aligned}
$$

where we have used Eq. (2.18) to simplify our expression.

We will later find that working in Euclidean space is computationally helpful for our curved space numerics. The switch from 4-dimensional spacetime to 4-dimensional Euclidean space is achieved by switching to imaginary time, that is

$$t = -i\tau, \qquad (2.27)$$

hence rewriting the spacetime metric in Euclidean form:

$$ds^2 = d\tau^2 + dr^2 + r^2 d\theta^2 + r^2\sin^2\theta d\phi^2. \qquad (2.28)$$

Let us also define a Euclidean Green's function, $S_E(\tau,\vec{x};\tau',\vec{x'})$, in terms of the spinor Feynman propagator

$$S_F(t,\vec{x};t',\vec{x'}) = -iS_E(\tau,\vec{x};\tau',\vec{x'}), \qquad (2.29)$$

in which $\vec{x}$ and $\vec{x'}$ only refer to spatial coordinates. The preceding relationship was shown to be valid in general static spherically symmetric spacetimes in appendix D of Groves *et al.* [30]. By direct substitution of Eq. (2.29) into Eq. (2.26) we see that $S_E(\tau,\vec{x};\tau',\vec{x'})$ for a massless fermion field must satisfy

$$\gamma_E^{\alpha}\partial_{\alpha}S_E(\tau,\vec{x};\tau',\vec{x'}) = \mathbf{1}\delta^4(x-x'), \qquad (2.30)$$

where γ_E^{α} are the Euclidean Dirac matrices which are related in a simple way to the ordinary Dirac matrices:

$$\gamma_E^0 \equiv \gamma^0 \quad \gamma_E^i \equiv -i\gamma^i. \qquad (2.31)$$

Similarly, we can write down a Euclidean Dirac equation for massless fermions:

$$-\gamma_E^{\mu}\partial_{\mu}\psi = 0. \qquad (2.32)$$

2.2 Curved Spacetime

Now we must determine how to handle fermions in curved spacetime. Normally if one wants to change a flat space equation into the curved space formalism of general relativity one simply replaces all partial derivatives, ∂_α, with a covariant derivative, ∇_α, and substitutes the curved metric tensor $g_{\mu\nu}$ for the Minkowski tensor $\eta_{\mu\nu}$ everywhere. This prescription works fine for tensor objects, but not for a spinor field, since this method only works for mathematical objects that behave like tensors under Lorentz transformations. Therefore, we can't simply replace the partial derivatives in the above flat space expressions with a covariant derivative. Recall that the covariant derivative of a rank 1 tensor transforms like a rank 2 covariant tensor under a Lorentz transformation:

$$\nabla'_\theta W'_\alpha(x') = \Lambda_\theta{}^\mu \Lambda_\alpha{}^\nu \nabla_\mu W_\nu(x). \tag{2.33}$$

Now consider the Lorentz transformation of the partial derivative of the fermion field in flat space

$$\partial'_\alpha \psi'(x') = \Lambda_\alpha{}^\beta \mathcal{D}(\Lambda)\, \partial_\beta \psi(x). \tag{2.34}$$

The quantity $\partial_\alpha \psi(x)$ transforms like a spinor, $\mathcal{D}(\Lambda)$, and a tensor, $\Lambda^\beta{}_\alpha$. We would like to write the transformation from Eq. (2.34) in curved space as

$$\mathcal{H}'_a \psi'(x') = \Lambda_a{}^b \mathcal{D}(\Lambda) \mathcal{H}_b \psi(x), \tag{2.35}$$

in which $\mathcal{H}_a$ is a differential operator that will be specified below after we develop some more concepts.

Since the method for using spinors in Minkowski space is well understood, let's adopt the vierbein (literally German for four-leg) or tetrad formalism [38] for curved space calculations. This allows us to retain a connection to the Lorentz group of flat space. Space is locally flat at a small enough scale even in curved space, so by the Equivalence Principle we can erect a set of locally flat coordinates ξ^a at every point that are referenced to the spacetime coordinates x^μ. For this discussion Latin indices are associated with the locally flat coordinates at a point X, and Greek indices are associated with the spacetime coordinates at a point x. The vierbein functions are defined as

$$e^a{}_\mu(X) \equiv \left(\frac{\partial \xi^a(x)}{\partial x^\mu} \right)_{x=X}. \tag{2.36}$$

The reader should note that the function $e^a{}_\mu(X)$ is not a tensor, but a set of four vector fields (Latin index) with four components (Greek index). In addition, Latin indices and Greek indices are raised and lowered with η_{ab} and $g_{\mu\nu}$ respectively. The vierbeins must satisfy

$$g_{\mu\nu}(x) = e^a{}_\mu(x) e^b{}_\nu(x) \eta_{ab}. \tag{2.37}$$

It is useful to define the inverse of $e^a{}_\mu$ as

$$e_a{}^\mu(x) \equiv \eta_{ab} g^{\mu\nu}(x) e^b{}_\nu(x) \tag{2.38}$$

hence, we can also write

$$\eta_{ab} = e_a{}^\mu(x) e_b{}^\nu(x) g_{\mu\nu}(x). \tag{2.39}$$

When two vierbeins are contracted with each other by either their locally flat or spacetime coordinates, it is simple to prove using Eq. (2.37), Eq. (2.39) and Eq. (2.38) that the following statements are true:

$$\begin{aligned} \delta^\beta_\mu &= e^a{}_\mu(x) e_a{}^\beta(x), \\ \delta^c_a &= e_a{}^\gamma(x) e^c{}_\gamma(x). \end{aligned} \tag{2.40}$$

This discussion is applicable generically to any spacetime, but we specifically are interested in static spherically symmetric spacetimes, Eq. (1.18). The vierbein we used is [30]

$$\begin{aligned} e_a{}^t &= \begin{pmatrix} f^{-\frac{1}{2}} \\ 0 \\ 0 \\ 0 \end{pmatrix}, \qquad e_a{}^r = \begin{pmatrix} 0 \\ h^{-\frac{1}{2}} \sin\theta\cos\phi \\ h^{-\frac{1}{2}} \sin\theta\sin\phi \\ h^{-\frac{1}{2}} \cos\theta \end{pmatrix}, \\ e_a{}^\theta &= \begin{pmatrix} 0 \\ r^{-1}\cos\theta\cos\phi \\ r^{-1}\cos\theta\sin\phi \\ -r^{-1}\sin\theta \end{pmatrix}, \qquad e_a{}^\phi = \begin{pmatrix} 0 \\ -r^{-1}\csc\theta\sin\phi \\ r^{-1}\csc\theta\cos\phi \\ 0 \end{pmatrix}. \end{aligned} \tag{2.41}$$

We are now in a position to specify the function $\mathcal{H}_a$ from Eq. (2.35) and write our flat space equations for fermions in curved space. We want $\mathcal{H}_a\psi(x)$ to transform like a spinor and a vector just as $\partial_\alpha\psi(x)$ does in flat space; therefore, we need a transformation rule of the form

$$\mathcal{H}_a\psi(x) \to \Lambda_a{}^b \mathcal{D}(\Lambda) \mathcal{H}_b\psi(x). \tag{2.42}$$

Suppose we define

$$\mathcal{H}_a \equiv e_a{}^\mu[\partial_\mu + \Gamma_\mu], \tag{2.43}$$

where Γ_μ is a matrix connection with Lorentz transformation rule

$$\Gamma_\mu(x) \to \mathcal{D}(\Lambda)\,\Gamma_\mu(x)\mathcal{D}^{-1}(\Lambda) - [\partial_\mu \mathcal{D}(\Lambda)]\mathcal{D}^{-1}(\Lambda). \tag{2.44}$$

It then can be shown that Eq. (2.43) and Eq. (2.44) together yield Eq. (2.42). For infinitesimal transformations the inverse of $\mathcal{D}$ is

$$\mathcal{D}^{-1}(\Lambda) = \mathbf{1} - \frac{1}{2}\omega_{\alpha\beta}\sigma^{\alpha\beta}. \tag{2.45}$$

The proper connection for infinitesimal transformations, can be proven to be

$$\Gamma_\mu(x) = \frac{1}{2}\sigma^{ab}e_a{}^\gamma\nabla_\mu e_{b\gamma}, \tag{2.46}$$

by direct substitution. In Eq. (2.46), ∇_μ is the normal covariant derivative from general relativity. We could have just as easily worked out Euclidean versions of the above expressions. The logic is the same as the preceding for Euclidean space, and we arrive at the following expressions:

$$\mathcal{H}_a^E \equiv e_a{}^\mu[\partial_\mu + \Gamma_\mu^E], \tag{2.47}$$

with

$$\Gamma_\mu^E(x) = \frac{1}{2}\sigma_E^{ab}e_a{}^\gamma\nabla_\mu e_{b\gamma}. \tag{2.48}$$

The Euclidean generators of the Lorentz group are written in terms of the commutator of the previously defined Euclidean Dirac matrices

$$\sigma_E^{ab} = \frac{1}{4}[\gamma_E^a, \gamma_E^b]. \tag{2.49}$$

Replacing ∂_α by $\mathcal{H}_a^E$ in Eq. (2.30) and Eq. (2.32) yields the Euclideanized curved space versions of the Green's equation for $S_E(\tau, \vec{x}; \tau', \vec{x'})$ and the Dirac equation for massless fermions respectively:

$$-\gamma_E^a\mathcal{H}_a^E S_E(\tau, \vec{x}; \tau', \vec{x'}) = \mathbf{1}\frac{\delta^4(x-x')}{\sqrt{g_E}}, \tag{2.50}$$

$$-\gamma_E^a\mathcal{H}_a^E\psi(x) = 0. \tag{2.51}$$

The factor of the determinant of the Euclideanized metric g_E must be included, since the 4 dimensional delta function is now a tensor density.

2.2.1 Determination of the quantum stress-energy tensor: theory

Recall our goal is to numerically compute the expectation value of the full renormalized stress-energy tensor operator, $\langle T_{\mu\nu}(x)\rangle_{\rm ren}$, for the massless fermion field for a variety of static spherically symmetric spacetimes. The unrenormalized stress-energy tensor can be written in terms of $S_E(\tau,\vec{x};\tau',\vec{x'})$ which in turn can be written in terms of solutions to the radial equation obtained when the Euclidean Dirac equation is solved [30]. Once a form for $\langle T_{\mu\nu}(x)\rangle_{\rm unren}$ is found, we must identify the divergences it contains (regularization) and then remove the divergent terms in a Lorentz invariant manner (renormalization). Using separation of variables in spherical coordinates, the solutions to the Euclidean Dirac equation are found to consist of two, four component solutions [30]:

$$\begin{aligned}
\psi_1(x) &= \frac{e^{i\omega\tau}}{rf^{1/4}}\begin{pmatrix} F_{\omega,j}(r)\Psi^m_{j,+}(\theta,\phi) \\ G_{\omega,j}(r)\Psi^m_{j,-}(\theta,\phi)\end{pmatrix} \\
\psi_2(x) &= \frac{e^{i\omega\tau}}{rf^{1/4}}\begin{pmatrix} G_{\omega,j}(r)\Psi^m_{j,-}(\theta,\phi) \\ F_{\omega,j}(r)\Psi^m_{j,+}(\theta,\phi)\end{pmatrix},
\end{aligned} \tag{2.52}$$

where the indices can take on the values $j=\frac{1}{2},\frac{3}{2},...$ and $m=-j,-j+1,...,j$. The angular functions have a known form [75, 76] in terms of the normal spherical harmonics $Y^{m\pm1/2}_{j\pm1/2}$:

$$\begin{aligned}
\Psi^m_{j,+}(\theta,\phi) &= \begin{pmatrix} \sqrt{\frac{j+m}{2j}}Y^{m-1/2}_{j-1/2} \\ \sqrt{\frac{j-m}{2j}}Y^{m+1/2}_{j-1/2}\end{pmatrix} \\
\Psi^m_{j,-}(\theta,\phi) &= \begin{pmatrix} \sqrt{\frac{j+1-m}{2j+2}}Y^{m-1/2}_{j+1/2} \\ -\sqrt{\frac{j+1+m}{2j+2}}Y^{m+1/2}_{j+1/2}\end{pmatrix}.
\end{aligned} \tag{2.53}$$

Substituting the solutions Eq. (2.52) back into Eq. (2.51), we find the that the mode solutions satisfy a pair of coupled linear first order differential equations

$$\begin{aligned}
\frac{\omega}{\sqrt{f(r)}}F_{\omega,\ell} &= \frac{1}{\sqrt{h(r)}}\partial_r G_{\omega,\ell}+\frac{\ell}{r}G_{\omega,\ell} \\
\frac{\omega}{\sqrt{f(r)}}G_{\omega,\ell} &= \frac{1}{\sqrt{h(r)}}\partial_r F_{\omega,\ell}-\frac{\ell}{r}F_{\omega,\ell},
\end{aligned} \tag{2.54}$$

in which $\ell=j+1/2$. There will be two sets of linearly independent solutions that exist at every value of r. We designate them the p solutions yielding $F^p_{\omega,\ell}$ and $G^p_{\omega,\ell}$,

and the q solutions yielding $F^q_{\omega,\ell}$ and $G^q_{\omega,\ell}$. We choose boundary conditions such that the p solutions are finite at some "inner boundary", whether it's an event horizon for a black hole or spatial infinity on the other side of a wormhole. Similarly the boundary conditions are such that the q solutions are finite at infinity. The normalizations of the solutions are chosen to satisfy the Wronskian condition

$$\omega[G^q_{\omega,\ell}(r)F^p_{\omega,\ell}(r) - F^q_{\omega,\ell}(r)G^p_{\omega,\ell}(r)] = 1. \tag{2.55}$$

We will discuss numerically solving Eq. (2.54) in the next chapter.

The Euclidean Green's function for the massless spin one-half field has been constructed by Groves *et al.* [30, 77]. The result is

$$\begin{aligned} S_E(\tau,\vec{x};\tau',\vec{x}\,') = i\int_{-\infty}^{\infty}\frac{d\omega\,\omega e^{i\omega(\tau-\tau')}}{2\pi r r' f(r)^{1/4}f(r')^{1/4}}\sum_{j=\frac{1}{2}}^{\infty}\sum_{m=-j}^{j} \\ \Bigg\{ \quad \theta(r-r')\left[\begin{pmatrix} F^q_{\omega,j}(r)\Psi^m_{j,+}(\theta,\phi) \\ G^q_{\omega,j}(r)\Psi^m_{j,-}(\theta,\phi)\end{pmatrix}\otimes\begin{pmatrix} F^p_{\omega,j}(r')\Psi^{m\dagger}_{j,+}(\theta',\phi') & G^p_{\omega,j}(r')\Psi^{m\dagger}_{j,-}(\theta',\phi')\end{pmatrix}\right. \\ - \quad \left.\begin{pmatrix} G^q_{\omega,j}(r)\Psi^m_{j,-}(\theta,\phi) \\ F^q_{\omega,j}(r)\Psi^m_{j,+}(\theta,\phi)\end{pmatrix}\otimes\begin{pmatrix} G^p_{\omega,j}(r')\Psi^{m\dagger}_{j,-}(\theta',\phi') & F^p_{\omega,j}(r')\Psi^{m\dagger}_{j,+}(\theta',\phi')\end{pmatrix}\right] \\ + \quad \theta(r'-r)\Big[p\leftrightarrow q\Big]\Bigg\}\,. \end{aligned} \tag{2.56}$$

In the above expression, $\otimes$ designates a direct product and, the notation $[p \leftrightarrow q]$ means take the entire previous term in brackets and rewrite it swapping p with q. Notice that Eq. (2.56) contains a sum over all possible j values that is performed first and an integral over ω that is computed second.

In addition, we must write the unrenormalized stress-energy tensor in terms of the Euclidean Green's function. This procedure is handled in detail in the appendices of Groves *et al.* [30], so only a general scheme is given here. First one can show

$$T_{\mu\nu}(x) = \frac{i}{4}\mathrm{Tr}\left(\gamma_{(\mu}\left[\nabla_{\nu)}\psi(x),\overline{\psi}(x)\right] + \gamma_{(\mu}\left[\nabla_{\nu)}\overline{\psi}(x),\psi(x)\right]\right)\,. \tag{2.57}$$

If one just naively calculates $T_{\mu\nu}(x)$ utilizing Eq. (2.57), it diverges and hence needs to be renormalized in some fashion to yield a physical result. We therefore must also write the stress-energy tensor in a form useful for renormalization. We shall utilize the method of point splitting where we split the points in $T_{\mu\nu}(x)$. Renormalization

counterterms (also with points split) are then subtracted from $T_{\mu\nu}(x)$ and the points are brought together afterwards. Splitting the points symmetrically in Eq. (2.57) we obtain [71, 72]

$$\begin{aligned} T_{\mu\nu}(x) &= \frac{i}{8}\lim_{x'\to x}\mathrm{Tr}\left\{\gamma_{(\mu}\left(\nabla_{\nu)}\left[\psi(x),\overline{\psi}(x')\right]\right)I(x',x)+\gamma_{(\mu}I(x,x')\nabla_{\nu)}\left[\overline{\psi}(x),\psi(x')\right]\right. \\ &\left.+\gamma_{(\mu}g_{\nu)}{}^{\lambda'}\left(\nabla_{\lambda'}\left[\overline{\psi}(x'),\psi(x)\right]\right)I(x',x)+\gamma_{(\mu}g_{\nu)}{}^{\lambda'}I(x,x')\nabla_{\lambda'}\left[\psi(x'),\overline{\psi}(x)\right]\right\}, \end{aligned} \tag{2.58}$$

in which $g_{\nu}{}^{\lambda'}$ is a bivector of parallel transport. The two point functions $I(x,x')$ and $I(x',x)$ are bispinors of parallel transport. A bivector behaves as a vector under Lorentz transformations at x and x' while a bispinor behaves as a spinor at these two same points under such transformations. These bivectors and bispinors are needed to parallel transport the terms in Eq. (2.58) that are vectors and spinors along the shortest geodesic connecting the points x and x'.

Now we are ready to write the the unrenormalized stress-energy tensor in terms of the Euclidean Green's function. Groves *et al.* [30] first quantize the field ψ at this point and reinterpret Eq. (2.58) as an equation for the stress-energy tensor operator. Then an expectation value of $T_{\mu\nu}$ can be calculated. The result is [30]

$$\langle T_{\mu\nu}(x)\rangle_{\mathrm{unren}} = -\tfrac{1}{4}\lim_{x'\to x}\mathrm{Im}\left\{\mathrm{Tr}\left[\gamma_{(\mu}\left(\nabla_{\nu)}\left[S_E+S_E^c\right]-g_{\nu)}{}^{\lambda'}\nabla_{\lambda'}\left[S_E+S_E^c\right]\right)I(x',x)\right]\right\}, \tag{2.59}$$

where S_E is understood to stand for $S_E(x,x')$, and c stands for the charge conjugation operation such that

$$S_E^c = C(\bar{S}_E^c)^T C^\dagger, \tag{2.60}$$

where $C = i\gamma^2\gamma^0$ in the Dirac representation. The unrenormalized stress-energy tensor from Eq. (2.59) is still infinite and the DeWitt-Schwinger renormalization counterterms [72] must be subtracted to render it finite. This yields $\langle T_{\mu\nu}(x)\rangle_{\mathrm{ren}}$ as discussed in detail in Groves *et al.* [30] and references therein.

We are now prepared to write an expression for full renormalized stress-energy tensor as

$$\langle T_{\mu\nu}(x)\rangle_{\mathrm{ren}} \equiv \langle T_{\mu\nu}(x)\rangle_{\mathrm{numeric}} + \langle T_{\mu\nu}(x)\rangle_{\mathrm{analytic}}. \tag{2.61}$$

The numeric portion of the full stress-energy tensor is [30]

$$\langle T_t{}^t(x)\rangle_{\rm num} = \frac{1}{\pi^2}\int_0^\infty \frac{d\omega}{r^2 f}\left[\omega^2 A_1 - \frac{r^2\omega^3}{f} - \omega\left(\frac{1}{12} - \frac{1}{12h} + \frac{rf'}{6fh} - \frac{5r^2f'^2}{48f^2h}\right.\right.$$
$$\left.\left. + \frac{rh'}{12h^2} - \frac{r^2f'h'}{24fh^2} + \frac{r^2f''}{12fh}\right)\right] + \frac{1}{4\pi^2}\int_\lambda^\infty \frac{d\omega}{\omega} U_t{}^t \qquad (2.62)$$

$$\langle T_r{}^r(x)\rangle_{\rm num} = \frac{1}{\pi^2}\int_0^\infty \frac{d\omega}{r^2 f}\left[\frac{\omega A_2 f^{1/2}}{r} - \omega^2 A_1 + \frac{r^2\omega^3}{3f} + \omega\left(\frac{1}{12} - \frac{1}{12h} + \frac{rf'}{12fh}\right.\right.$$
$$\left.\left. - \frac{r^2f'^2}{48f^2h}\right)\right] + \frac{1}{4\pi^2}\int_\lambda^\infty \frac{d\omega}{\omega} U_r{}^r \qquad (2.63)$$

$$\langle T_\theta{}^\theta(x)\rangle_{\rm num} = \langle T_\phi{}^\phi(x)\rangle_{\rm num} = \frac{1}{2\pi^2}\int_0^\infty \frac{d\omega}{r^2 f}\left[-\frac{\omega A_2 f^{1/2}}{r} + \frac{2r^2\omega^3}{3f} + \omega\left(\frac{rf'}{12fh}\right.\right.$$
$$\left.\left. - \frac{r^2f'^2}{12f^2h} + \frac{rh'}{12h^2} - \frac{r^2f'h'}{24fh^2} + \frac{r^2f''}{12fh}\right)\right] + \frac{1}{4\pi^2}\int_\lambda^\infty \frac{d\omega}{\omega} U_\theta{}^\theta\ , \qquad (2.64)$$

in which the tensor $U_\mu{}^\nu$ is

$$U_\mu{}^\nu \equiv \frac{1}{10}\left(R_{\rho\mu\tau}{}^\nu R^{\rho\tau} - \frac{1}{4}R^{\rho\tau}R_{\rho\tau}g_\mu{}^\nu\right) - \frac{1}{30}R\left(R_\mu{}^\nu - \frac{1}{4}Rg_\mu{}^\nu\right)$$
$$+ \frac{1}{20}(R_\mu{}^\nu)_{;\rho}{}^\rho - \frac{1}{60}R_{;\mu}{}^\nu - \frac{1}{120}R_{;\rho}{}^\rho g_\mu{}^\nu, \qquad (2.65)$$

λ is an infrared cutoff, and the functions A_1 and A_2 are given by

$$A_1 = \sum_{\ell=0}^\infty\left[(\ell{+}1)F^q_{\omega,\ell+\frac{1}{2}}(r)F^p_{\omega,\ell+\frac{1}{2}}(r) - \ell\, G^q_{\omega,\ell-\frac{1}{2}}(r)G^p_{\omega,\ell-\frac{1}{2}}(r) + \frac{r}{f^{1/2}}\right]$$
$$A_2 = \sum_{\ell=0}^\infty\left[\ell(\ell{+}1)\left(G^q_{\omega,\ell+\frac{1}{2}}(r)F^p_{\omega,\ell+\frac{1}{2}}(r) + F^q_{\omega,\ell-\frac{1}{2}}(r)G^p_{\omega,\ell-\frac{1}{2}}(r)\right) - \frac{\ell(\ell{+}1)}{\omega} + \frac{r^2\omega}{2f}\right]\ .$$

The analytic portion, as the name implies, can be derived analytically [30]

$$\langle T_{\mu\nu}(x)\rangle_{\rm analytic} = (T_{\mu\nu})_0 + (T_{\mu\nu})_{\log} \qquad (2.66)$$

where

$$
\begin{aligned}
\left(T_t{}^t\right)_0 &= \frac{1}{240\pi^2}\left[\frac{1}{r^4}-\frac{1}{r^4h^2}+\frac{43f'^2}{24r^2f^2h^2}-\frac{5f'^2}{8r^2f^2h}-\frac{19f'^3}{12rf^3h^2}+\frac{77f'^4}{192f^4h^2}-\frac{2h'}{r^3h^3}\right.\\
&+ \frac{15f'h'}{4r^2fh^3}-\frac{5f'h'}{12r^2fh^2}-\frac{15f'^2h'}{8rf^2h^3}+\frac{f'^3h'}{24f^3h^3}-\frac{7h'^2}{4r^2h^4}-\frac{3f'h'^2}{2rfh^4}-\frac{19f'^2h'^2}{32f^2h^4}\\
&+ \frac{7h'^3}{rh^5}-\frac{7f'h'^3}{4fh^5}-\frac{5f''}{6r^2fh^2}+\frac{5f''}{6r^2fh}+\frac{5f'f''}{6rf^2h^2}-\frac{f'^2f''}{12f^3h^2}-\frac{2h'f''}{rfh^3}+\frac{9f'h'f''}{8f^2h^3}\\
&+ \frac{19h'^2f''}{8fh^4}-\frac{3f''^2}{8f^2h^2}+\frac{h''}{r^2h^3}+\frac{f'h''}{2rfh^3}+\frac{f'^2h''}{4f^2h^3}-\frac{13h'h''}{2rh^4}+\frac{13f'h'h''}{8fh^4}-\frac{f''h''}{fh^3}\\
&+ \left.\frac{2f'''}{rfh^2}-\frac{f'f'''}{2f^2h^2}-\frac{3h'f'''}{2fh^3}+\frac{h'''}{rh^3}-\frac{f'h'''}{4fh^3}+\frac{f''''}{2fh^2}\right] \qquad (2.67)
\end{aligned}
$$

$$
\begin{aligned}
\left(T_r{}^r\right)_0 &= \frac{1}{240\pi^2}\left[\frac{2f'}{r^3fh^2}-\frac{5f'^2}{8r^2f^2h^2}+\frac{5f'^2}{24r^2f^2h}-\frac{7f'^3}{24rf^3h^2}+\frac{f'^4}{192f^4h^2}+\frac{f'h'}{2r^2fh^3}\right.\\
&- \frac{f'^2h'}{4rf^2h^3}+\frac{f'^3h'}{16f^3h^3}-\frac{7f'h'^2}{4rfh^4}+\frac{7f'^2h'^2}{32f^2h^4}-\frac{2f''}{r^2fh^2}+\frac{2f'f''}{rf^2h^2}-\frac{f'^2f''}{8f^3h^2}+\frac{h'f''}{rfh^3}\\
&- \left.\frac{f'h'f''}{4f^2h^3}-\frac{f''^2}{8f^2h^2}+\frac{f'h''}{rfh^3}-\frac{f'^2h''}{8f^2h^3}-\frac{f'''}{rfh^2}+\frac{f'f'''}{4f^2h^2}\right] \qquad (2.68)
\end{aligned}
$$

$$
\begin{aligned}
\left(T_\theta{}^\theta\right)_0 &= \left(T_\phi{}^\phi\right)_0 = \frac{1}{240\pi^2}\left[-\frac{f'}{r^3fh^2}-\frac{3f'^3}{16rf^3h^2}+\frac{29f'^4}{64f^4h^2}-\frac{3f'h'}{2r^2fh^3}-\frac{7f'^2h'}{16rf^2h^3}\right.\\
&+ \frac{73f'^3h'}{96f^3h^3}-\frac{3f'h'^2}{4rfh^4}+\frac{31f'^2h'^2}{32f^2h^4}+\frac{7f'h'^3}{4fh^5}+\frac{f''}{r^2fh^2}+\frac{7f'f''}{12rf^2h^2}-\frac{73f'^2f''}{48f^3h^2}\\
&+ \frac{11h'f''}{4rfh^3}-\frac{2f'h'f''}{f^2h^3}-\frac{19h'^2f''}{8fh^4}+\frac{7f''^2}{8f^2h^2}+\frac{f'h''}{4rfh^3}-\frac{3f'^2h''}{8f^2h^3}-\frac{13f'h'h''}{8fh^4}\\
&+ \left.\frac{f''h''}{fh^3}-\frac{3f'''}{2rfh^2}+\frac{3f'f'''}{4f^2h^2}+\frac{3h'f'''}{2fh^3}+\frac{f'h'''}{4fh^3}-\frac{f''''}{2fh^2}\right] \qquad (2.69)
\end{aligned}
$$

$$
\left(T_\mu{}^\nu\right)_{\log} = -\frac{1}{4\pi^2}U_\mu{}^\nu\,\ln\left(\frac{\mu f^{1/2}}{2\lambda}\right). \qquad (2.70)
$$

In the logarithmic portion of the analytic stress-energy tensor, μ is an arbitrary renormalization parameter introduced in the logarithmic Dewitt-Schwinger counterterms. It should be noted that the above expression for $\langle T_{\mu\nu}(x,x')\rangle_{\text{analytic}}$ is for zero temperature objects such as in this work. For a nonzero temperature object there are extra terms as can be seen in [30]. The tensor $U_\mu{}^\nu$ vanishes and therefore the logarithmic term does as well for a Schwarzschild black hole, since all components of the Ricci tensor (and therefore the Ricci scalar) are zero. We do not have this luxury for the extreme Reissner-Nordström black hole, so we simply set $\mu M = 1$. For wormholes,

varying the parameter μ will give us the freedom to attempt to satisfy the exotic energy conditions required for a self-consistent wormhole solution discussed in chapter one.

The procedure for the derivation of $\langle T_{\mu\nu}(x)\rangle_{\rm analytic}$ described here is very similar to that used in the conformal scalar field calculation of $\langle T_{\mu\nu}(x)\rangle_{\rm ren}$ done by Howard and Candelas in [78], and the work of Jensen and Ottewill for the electromagnetic [79] field for general spherically symmetric spacetimes. The analytic part of $\langle T_{\mu\nu}(x)\rangle_{\rm ren}$ is separately conserved and has trace equal to the trace anomaly appearing in Eq. (2.78); hence, it has been frequently used in the past as an approximation for the full renormalized stress-energy tensor because of its ease of computation relative to the exact expression. The form of $\langle T_{\mu\nu}(x)\rangle_{\rm analytic}$ for the massless spin one-half field presented here and for the thermal case in [30] are in agreement with those derived by other authors in the case of a general static spherically symmetric spacetime [23] and for Schwarzschild spacetime [80]. In addition, recently Matyjasek has also found an analytic approximation for Schwarzschild spacetime that he shows is consistent with the one used here [81]. We will show the actual graphical results for $\langle T_{\mu\nu}(x)\rangle_{\rm analytic}$ in conjunction with those for $\langle T_{\mu\nu}(x)\rangle_{\rm ren}$ in the next chapter to elucidate how useful the analytic approximation actually is in comparison to the full calculation.

In practice, the above expression for $\langle T_{\mu\nu}(x)\rangle_{\rm ren}$ doesn't converge fast enough to the numerical accuracy we desired, since a cutoff must be used to truncate the sum over j and the integral over ω at large values of these parameters. We overcame this obstacle by implementing a high order WKB-like expansion for the mode functions at all ω and j values employed in finding the actual mode solutions. Utilizing higher and higher orders of this expansion allows for the inclusion of less modes and faster convergence. As we shall see in the next chapter, this procedure is implemented differently than a standard WKB expansion. We then add and subtract this enhanced WKB approximation from the quantity $\langle T_{\mu\nu}(x)\rangle_{\rm ren}$ so that

$$\langle T_{\mu\nu}(x)\rangle_{\rm num} = \langle T_{\mu\nu}(x)\rangle_{\rm modes} + \langle T_{\mu\nu}(x)\rangle_{\rm WKBfin}. \tag{2.71}$$

The quantity $\langle T_{\mu\nu}(x)\rangle_{\rm modes}$ is defined as the contribution from the difference between the actual modes and the WKB approximation. For example, the $T_t{}^t$ component is

$$\langle T_t{}^t(x)\rangle_{\rm modes} = \frac{1}{\pi^2 r^2 f}\int_0^\infty \omega^2\,(A_1 - A_{1\,\rm WKB})\,d\omega, \tag{2.72}$$

where $\langle T_{\mu\nu}(x)\rangle_{\rm WKBfin}$ is defined the same as $\langle T_{\mu\nu}(x)\rangle_{\rm num}$, but with A_1 and A_2 replaced by their WKB approximation so that, for example, the $T_t{}^t$ component is

$$\begin{aligned}\langle T_t{}^t(x)\rangle_{\rm WKBfin} &= \frac{1}{\pi^2 r^2 f}\int_0^\infty d\omega\left[\omega^2 A_{1\,\rm WKB} - \frac{r^2\omega^3}{f} - \omega\left(\frac{1}{12} - \frac{1}{12h} + \frac{rf'}{6fh}\right.\right.\\ &- \left.\left.\frac{5r^2 f'^2}{48f^2 h} + \frac{rh'}{12h^2} - \frac{r^2 f'h'}{24fh^2} + \frac{r^2 f''}{12fh}\right)\right] + \frac{1}{4\pi^2}\int_\lambda^\infty \frac{d\omega}{\omega} U_t{}^t. \quad (2.73)\end{aligned}$$

The sums and integrals in Eqs. (2.73), and the corresponding expressions can be performed analytically. We are then left with a final form for the way in which we shall compute the full renormalized stress-energy tensor as opposed to that in Eq. (2.61)

$$\langle T_{\mu\nu}(x)\rangle_{\rm ren} = \langle T_{\mu\nu}(x)\rangle_{\rm modes} + \langle T_{\mu\nu}(x)\rangle_{\rm WKBfin} + \langle T_{\mu\nu}(x)\rangle_{\rm analytic}, \quad (2.74)$$

taking note that all three of these quantities have been rendered finite. The modes portion of the full stress-energy tensor must be computed numerically, since the mode functions are not exactly known. Its computation as well as finding $\langle T_{\mu\nu}(x)\rangle_{\rm WKB}$ will be the subject of the next chapter.

Let's discuss a few important properties that $\langle T_{\mu\nu}\rangle_{\rm ren}$ should have in some detail. These properties will later be utilized to test the validity of our numerical results. First the classical stress-energy tensor is conserved. That is, its covariant derivative vanishes

$$\nabla_\nu T^\nu{}_\lambda = 0. \quad (2.75)$$

The covariant derivative of the left hand side of Einstein's equation vanishes, so for the quantum stress-energy tensor to be used as a source on the right side of that same equation it must also be covariantly conserved.

We also will examine the trace of $\langle T_{\mu\nu}\rangle_{\rm ren}$ in our numerical analysis. Classically the total action is invariant under conformal transformations of the metric of the form [31]

$$g_{\mu\nu}(x) \to \bar{g}_{\mu\nu}(x) = \Omega^2(x) g_{\mu\nu}(x) \quad (2.76)$$

as long as the operator ψ transforms as

$$\psi \to \Omega^{-3/2}(x)\psi, \quad (2.77)$$

where $\Omega(x)$ is a continuous, non-vanishing, finite, and real function. The effect of such transformation is to stretch or compress the spacetime manifold while leaving the geometry unchanged, and therefore the form of line element ds^2 unchanged. Our renormalization procedure breaks the conformal symmetry, in the massless four dimensional limit, leaving behind a nonzero trace. This is called the trace anomaly [82, 83]. If examined, one can see that the trace of the Dewitt-Schwinger counterterms is nonzero. We will be forming $\langle T_\rho{}^\rho \rangle_{\rm ren}$ by a subtraction of $\langle T_\rho{}^\rho \rangle_{\rm DS}$ from $\langle T_\rho{}^\rho \rangle_{\rm unren}$, therefore the trace anomaly will show up in our final result for the full stress-energy tensor. Christensen and Duff have derived a general expression for the trace anomaly for arbitrary spin fields [84], as well as specific results for the physically more important spins of 0, $\frac{1}{2}$, and 1 [85, 86]. By their derivation the trace anomaly for the massless spin one-half field is

$$\langle T_\mu{}^\mu(x) \rangle_{\rm ren} = \frac{1}{1440\pi^2} \left[\frac{7}{4} C_{\alpha\beta\gamma\delta} C^{\alpha\beta\gamma\delta} + \frac{11}{2} \left(R_{\alpha\beta} R^{\alpha\beta} - \frac{1}{3} R^2 \right) - 3 \Box R \right], \qquad (2.78)$$

in which $C_{\alpha\beta\gamma\delta}$ is the Weyl tensor [19]

$$\begin{aligned} C_{\alpha\beta\gamma\delta} &\equiv R_{\alpha\beta\gamma\delta} - \frac{1}{2} \left[g_{\alpha\gamma} R_{\beta\delta} + g_{\beta\delta} R_{\alpha\gamma} - g_{\alpha\delta} R_{\beta\gamma} - g_{\beta\gamma} R_{\alpha\delta} \right] \\ &+ \frac{1}{6} R \left[g_{\alpha\gamma} g_{\beta\delta} - g_{\alpha\delta} g_{\beta\gamma} \right]. \end{aligned} \qquad (2.79)$$

We also point out that the derivation by Christensen and Duff assumed 2 component spinors; therefore, we have multiplied their result by 2 for our 4 component spinors. We will see that when we arrive at numerical results later that for each spacetime considered the full stress-energy tensor satisfies the trace anomaly condition to the limits of quadruple precision.

Lastly, although not a general property of the full stress-energy tensor, we expect the components to have a specific form. This is because all spacetimes under study are time independent and spherically symmetric. Therefore the components of $\langle T_\mu{}^\nu(x) \rangle_{\rm ren}$ will satisfy

$$\begin{aligned} \langle T_\theta{}^\theta(x) \rangle_{\rm ren} &= \langle T_\phi{}^\phi(x) \rangle_{\rm ren}, \\ \langle T_\mu{}^\nu(x) \rangle_{\rm ren} &= 0 \quad \text{for} \quad \mu \neq \nu. \end{aligned} \qquad (2.80)$$

Chapter 3

Numerical computation of the quantum stress-energy tensor

Let us now discuss the relevant numerical techniques we employed in determining the full stress-energy tensor. In this chapter we shall first show how we numerically computed the solutions to the differential radial mode equations necessary for determining $\langle T_\mu{}^\nu(x)\rangle_{\rm modes}$. Then we will discuss the procedure utilized to find the WKB-like expansion for the mode functions needed for $\langle T_\mu{}^\nu(x)\rangle_{\rm WKB}$ and its implementation in finding $\langle T_\mu{}^\nu(x)\rangle_{\rm modes}$ and $\langle T_\mu{}^\nu(x)\rangle_{\rm WKBfin}$. Finally the results for $\langle T_\mu{}^\nu(x)\rangle_{\rm ren}$ will be discussed and compared to $\langle T_\mu{}^\nu(x)\rangle_{\rm analytic}$ for the extreme Reissner-Nordström black hole and the three wormhole spacetimes studied.

3.1 Solving the radial mode equations

Recall the coupled set of radial mode equations discussed in Chapter 2:

$$\begin{aligned}
\frac{\omega_M}{\sqrt{f(x)}}F_{\omega_M,\ell}(x) &= \frac{1}{\sqrt{h(x)}}\partial_x G_{\omega_M,\ell}(x) + \frac{\ell}{x}G_{\omega_M,\ell}(x) \\
\frac{\omega_M}{\sqrt{f(x)}}G_{\omega_M,\ell}(x) &= \frac{1}{\sqrt{h(x)}}\partial_x F_{\omega_M,\ell}(x) - \frac{\ell}{x}F_{\omega_M,\ell}(x),
\end{aligned} \tag{3.1}$$

where we have renamed the frequency ω_M and the radial coordinate x. Note that this x is not the x in the expressions in the previous section representing four spacetime coordinates. For the ERN black hole the mass M appears in the metric functions $f(x)$ and $h(x)$. Similarly for wormholes the throat radius r_0 appears. We want our calculations to be independent of these quantities so we shall scale them out of the

problem by defining for ERN

$$\omega \equiv \omega_M M, \quad r \equiv \frac{x}{M}, \tag{3.2}$$

and for wormholes

$$\omega \equiv \omega_M r_0, \quad r \equiv \frac{x}{r_0}. \tag{3.3}$$

Substituting either of the above sets of definitions into Eq. (3.1) yields

$$\begin{aligned} \frac{\omega}{\sqrt{f(r)}} F_{\omega,\ell}(r) &= \frac{1}{\sqrt{h(r)}} \partial_r G_{\omega,\ell}(r) + \frac{\ell}{r} G_{\omega,\ell}(r) \\ \frac{\omega}{\sqrt{f(r)}} G_{\omega,\ell}(r) &= \frac{1}{\sqrt{h(r)}} \partial_r F_{\omega,\ell}(r) - \frac{\ell}{r} F_{\omega,\ell}(r). \end{aligned} \tag{3.4}$$

We found the definition of a few new functions was helpful at this point. We will suppress the extra subscripts for the functions $F_{\omega,\ell}(r)$ and $G_{\omega,\ell}(r)$ in the following analysis. Let

$$\begin{aligned} A(r) &\equiv \frac{1}{2}(F+G), \\ B(r) &\equiv \frac{1}{2}(F-G), \end{aligned} \tag{3.5}$$

and their ratio be

$$z(r) \equiv \frac{B}{A} = \frac{F-G}{F+G}. \tag{3.6}$$

The function $z(r)$ is useful, since we can work with a single uncoupled expression as opposed to a coupled set. The relative normalization of the functions $F(r)$ and $G(r)$ is unimportant now, because of the use of the ratio in Eq. (3.6). We would like to get a differential equation for $z(r)$. This is achieved by taking the partial derivative with respect to r of $z(r)$, attaining an expression containing terms like $\partial_r F$ and $\partial_r G$, then using Eq. (3.4) one can derive the following differential equation for $z(r)$

$$\frac{dz(r)}{dr} = \frac{\ell\sqrt{h(r)}}{r}\left(1 - z(r)^2\right) - 2\omega\sqrt{\frac{h(r)}{f(r)}}\, z(r). \tag{3.7}$$

We need two solutions to Eq. (3.7), that keep $F(r)$ and $G(r)$ finite. One at the spacetime's inner boundary, and one at large r. We name these solutions $z^p(r)$ and $z^q(r)$ respectively. As will be demonstrated later, knowledge of $z^p(r)$ and $z^q(r)$ is sufficient to calculate the sums contained in the quantities A_1 and A_2 from Eq. (2.66). If ℓ or ω (or both) are large then the right side of Eq. (3.7) is much greater compared

to the left side, so we can approximate the left side as zero compared to the right. The differential equation for $z(r)$ then admits the approximate solutions

$$z_q^p(r) \approx Z_q^p(r) = -\frac{\omega r}{\ell\sqrt{f(r)}} \pm \sqrt{\frac{\omega^2 r^2}{\ell^2 f(r)} + 1}, \tag{3.8}$$

in which p refers to the upper sign and q refers to the lower sign. This approximation can be manipulated to show that

$$Z^p(r) = -\frac{1}{Z^q(r)}. \tag{3.9}$$

It is important to now notice that from Eq. (3.8) it can be seen that $0 < Z^p(r) \leq 1$ and $-\infty < Z^q(r) \leq -1$. For example, if $\omega = 0$ then $z^p(r) = 1$ exactly, or as $\frac{\omega r}{\ell\sqrt{f(r)}}$ becomes small then $z^p(r)$ approaches 1. Lastly, if $\frac{\omega r}{\ell\sqrt{f(r)}}$ is becoming large, then $z^p(r)$ approaches zero. Numerical results for the functions $z^p(r)$ and $z^q(r)$ shall be examined in a later section that will verify Eq. (3.8) and the conditions under which it is a good approximation.

3.1.1 The $z^q(r)$ solution

The method we practiced for determining $z^q(r)$ is the same for ERN and wormholes, so we shall discuss it first. For each value of ℓ and ω employed numerically we determine the value of $z^q(r)$ at every point r we are including. Define the value of our largest radial coordinate to be r_N. We could just employ Eq. (3.8) to calculate $z^q(r_N)$, but it is just an approximation. How do we know how accurate our result would be? What we actually do is start at a point higher than r_N, say R, such that when we integrate $z^q(R)$ down to $z^q(r_N)$ using Eq. (3.7), any error in the initial solution z^q value is damped away when we reach our first data point of interest $z^q(r_N)$. The logic for this procedure is as follows. Suppose our numerical solution for $z^q(r_N)$ is in error of the actual solution by δz. Then to linear order in δz we have

$$z_{\text{actual}}(r) = z^q(r) + \delta z. \tag{3.10}$$

Our goal is then to decrease any potential error in $z^q(r)$ by the fraction ϵ. Next using Eq. (3.7) and the fact that we are working at large r, so $h(r) \simeq f(r) \simeq 1$, we have

$$\frac{d\delta z}{dr} = -\frac{2\ell}{r} z^q \delta z - 2\omega\delta z, \tag{3.11}$$

in which we have kept only terms to linear order in δz. There are two cases to consider for this equation, $\frac{\ell}{r} \gg \omega$ and $\omega \gg \frac{\ell}{r}$. In the first case note that from Eq. (3.8), when $\frac{\ell}{r}$ is large $z^q \simeq -1$, and we get the differential equation

$$\frac{d\delta z}{dr} = \frac{2\ell}{r}\delta z; \tag{3.12}$$

therefore, $\delta z \propto r^{2\ell}$. Therefore to decrease δz by a small amount ϵ we should decrease the radial coordinate by $\epsilon^{1/2\ell}$. Notice that determining $z^q(r)$ numerically is stable for decreasing r, since δz is decreasing. Defining

$$\epsilon \equiv \frac{\delta z(r_N)}{\delta z(R)} = \left(\frac{r_N}{R}\right)^{2\ell}, \tag{3.13}$$

we see that we should start at the point

$$R = r_N \epsilon^{-\frac{1}{2\ell}}. \tag{3.14}$$

Following the same procedure for the case where $\omega \gg \frac{\ell}{r}$ one can show that the proper distance to start at is

$$R = r_N - \frac{\ln \epsilon}{2\omega}. \tag{3.15}$$

One can show that it is sufficient to use the smaller of Eq. (3.14) and Eq. (3.15) as the starting point. We used values of ϵ of 10^{-20} and 10^{-30} throughout these calculations and found no significant difference in the results. We therefore concluded that a value for ϵ of 10^{-20} was small enough to attain reliable results to quadruple precision.

We utilize a Bulirsch-Stoer integration routine that contains a Richardson extrapolation subroutine for extrapolation to zero step size [87] to integrate $z^q(R)$ for decreasing r using Eq. (3.7) to get the value of the function at the starting point $z^q(r_N)$. Once $z^q(r_N)$ is calculated we integrate in the decreasing r direction again to get $z^q(r_{N-1})$. This procedure continues until we have the value of $z^q(r)$ at all r to the desired accuracy. The Bulirsch-Stoer method involves first taking a giant step h from r using the relevant differential equation to calculate the function at the two points. This is obviously going to be very inaccurate, so now the region h is subdivided into progressively smaller regions. This region h is crossed with more steps using Richardson extrapolation until the step size is close to zero. If the extrapolation fails to converge or if too many subdivisions were needed for convergence a smaller step size is used. On the other hand, if the extrapolation converges quickly a larger step size is attempted. Graphical results of this procedure will be given after we discuss finding the $z^p(r)$ solution.

3.1.2 The $z^p(r)$ solution: ERN

The method employed for finding the $z^p(r)$ solution is quite different for ERN and wormholes, so we shall focus on each of them in turn. In general the method for ERN involves finding a very accurate value for $z^p(r)$ at our first radial point (close to the event horizon) via a series expansion, and then integrating upwards to get the value of $z^p(r)$ at the next point. The same integration technique is utilized as described in the previous section. Recall the metric functions for an ERN spacetime from Chapter 1:

$$f(x) = h^{-1}(x) = \left(1 - \frac{M}{x}\right)^2. \tag{3.16}$$

It is convenient to create a new radial coordinate s for this analysis to shift the location of the event horizon such that $s = x/M - 1$. Subsequently we write out the coupled set of differential equations (Eq. (3.4)) in terms of the functions A and B from Eq. (3.5) explicitly with the metric functions in terms of s

$$\begin{aligned} \frac{dA(s)}{ds} &= \omega \left(\frac{s+1}{s}\right)^2 A(s) + \frac{\ell}{s} B(s) \\ \frac{dB(s)}{ds} &= -\omega \left(\frac{s+1}{s}\right)^2 B(s) + \frac{\ell}{s} A(s). \end{aligned} \tag{3.17}$$

Solving the first of these equations for $B(s)$ followed by substituting the result into the other equation yields a second order differential equation for $A(s)$

$$\begin{aligned} s^4 \frac{d^2A(s)}{ds^2} + s^3 \frac{dA(s)}{ds} \\ - \left\{\omega^2 s^4 + \omega\left(4\omega + 1\right) s^3 + \left(6\omega^2 + \ell^2\right) s^2 + \omega\left(4\omega - 1\right) s + \omega^2\right\} A(s) = 0. \end{aligned} \tag{3.18}$$

It can be shown by direct substitution that the following series solution is appropriate

$$A(s) = \mathcal{A}(s) e^{\frac{-\omega(s^2+1)}{s}} s^{2\omega}, \tag{3.19}$$

where

$$\mathcal{A}(s) = \sum_{n=0}^{\infty} a_n s^n. \tag{3.20}$$

Substitution of Eq. (3.19) into Eq. (3.18) leads to the following recursion relation for the series coefficients a_n

$$-a_{n-2} 2\omega(n + 4\omega - 1) + a_{n-1}\left[(n-1)(n + 4\omega - 1) - 4\omega^2 - \ell^2\right] + a_n 2\omega n = 0, \tag{3.21}$$

where $n > 2$, and

$$a_1 = a_0 \frac{(4\omega^2 + \ell^2)}{2\omega}. \tag{3.22}$$

The lowest order coefficient a_0 is arbitrary; therefore, we can set it equal to 1 without loss of generality. The series solution for $B(s)$ is written in the same way as the $A(s)$ solution

$$B(s) = \mathcal{B}(s) e^{\frac{-\omega(s^2+1)}{s}} s^{2\omega}, \tag{3.23}$$

where

$$\mathcal{B}(s) = \sum_{n=0}^{\infty} b_n s^n. \tag{3.24}$$

We have a coupled set of differential equations; therefore, the coefficients b_n can be determined in terms of the a_n's. Substitution of the series solution for $A(s)$ into the first equation given in Eq. (3.17) yields

$$b_n - \frac{1}{\ell} n a_n + \frac{2\omega}{\ell} a_{n-1} = 0, \tag{3.25}$$

for $n > 1$. In addition $b_1 = \frac{\ell}{2\omega} a_0$, and $b_0 = 0$. Formally, the sums in Eqs. (3.20) and (3.24) are asymptotic series and never converge, but for sufficiently small s a terminated sum will work well as an estimate. A set of criteria were determined based on empirical data for how far a given value of s should be decreased such that the sums would converge to desired accuracy. These criteria were based on how large or small ℓ and ω were relative to each other. For example, when ℓ and ω were both small we found that the sum always converged if s was chosen to be the smaller .001 or $\omega/100$. The sums from Eqs. (3.20) and (3.24) were then computed until adding another term didn't change the result to thirty digit accuracy.

We calculated the z's as a function of distance from the event horizon using the scaled radial coordinate $s = x/M - 1$. This involved a large amount of bookkeeping and should be qualitatively described for clarity. It is also interesting to note that the Fortran code for this numerical process required the largest amount of computer time of any computations in this study. We first decided on a set of distances from the event horizon or throat, depending on the spacetime, at which we wanted to calculate the full stress-energy tensor and hence needed the z functions at those distances. The z functions were then computed for all ℓ and ω values desired. The specific range of distances s included were from 0.001 to 80.0. The large values for s were included to

study the large distance behavior of the full stress-energy tensor. This encompassed 470 total data points for s. This enabled the full stress-energy tensor to be studied near and very far from the event horizon, as we will discuss in a later section. At each distance, the z functions were computed for nearly 6000 ω values spanning from $\omega = 10^{-6}$ to $\omega = 80.0$ at each angular momentum quantum number specified. In particular, we included $\ell = 1$ to 100 in increments of 1 on the first trial, and then utilized $\ell = 200$ as the stopping point on the second trial. All computations were completed in quadruple precision. No difference was found in using the larger pool of ℓ's in computations of the full stress-energy tensor and served not only as a test of self-consistency, but also was used to determine where we could accurately truncate the infinite sum on ℓ later. In addition, care had to be taken as to how finely the ω values were clustered together, since the $z(r)$ functions are included in an integral over ω (see Eq. (3.81) below) which must be performed numerically. There will be more details of this integration later.

At this moment we shall examine some numerical results for the $z(r)$ functions for the ERN spacetime. Specifically we will address claims made earlier regarding the behavior of the $z(r)$ functions. Recall that when either ℓ or ω or both are large

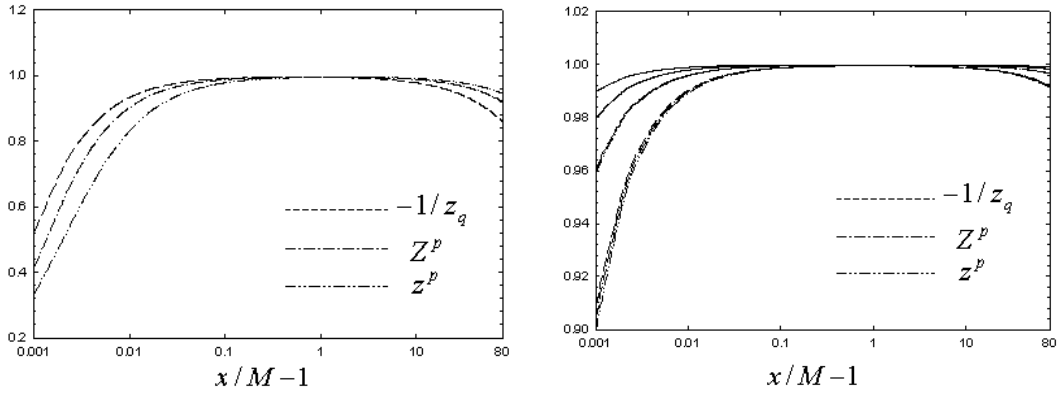

(a) ℓ=1 for $\omega = 0.001$.

(b) Starting from the bottom set of curves: $\ell =$ 10, 25, 50, and 100 for $\omega = 0.001$.

Figure 3.1: The z^p, $-1/z^q$, and the approximation Z^p for the ERN black hole plotted as a function of distance from the event horizon for progressively increasing ℓ for the entire data range.

$z^p(r)$ and $z^q(r)$ should tend towards their approximate values $Z^p(r)$ and $Z^q(r)$ given in Eq. (3.8) and $Z^p(r) = -1/Z^q(r)$. Figure 3.1 shows data for z^p, $-1/z^q$, and the

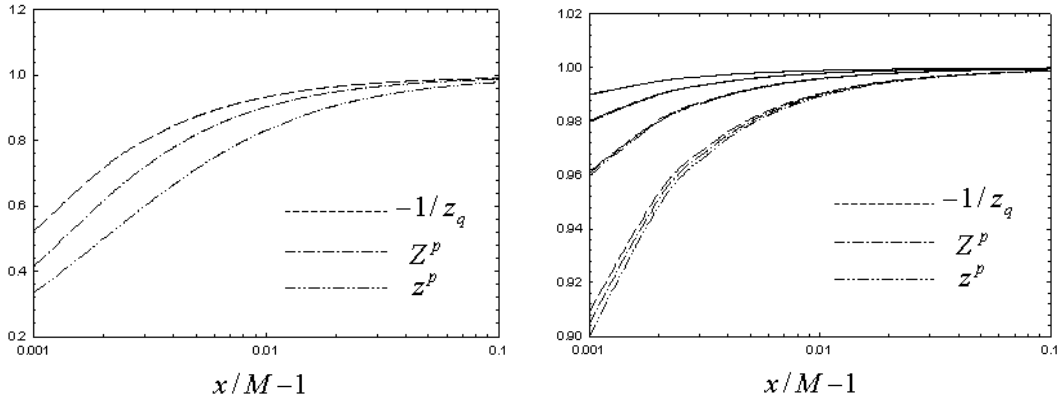

(a) ℓ=1.

(b) Starting from the bottom set of curves: ℓ = 10, 25, 50, and 100.

Figure 3.2: The z^p, $-1/z^q$, and the approximation Z^p for the ERN black hole plotted as a function of distance from the event horizon for progressively increasing ℓ. Here a smaller range of data is shown to illuminate the convergence of the respective sets of curves as ℓ is increased.

approximation Z^p plotted as a function of distance from the horizon at $\omega = 0.001$ for five different angular momentum quantum numbers. The $\ell = 1$ case is plotted separately from the other cases, because of the much different scale involved. Notice that as ℓ is increased the exact values of the z's approach the approximation making the three curves fall on top of one another. To better view this behavior, Fig. 3.2 shows the same results as Fig. 3.1, but with a much smaller data set. Also notice that as ℓ gets larger all three curves approach 1.0 for all distances from the horizon as expected from Eq. (3.8). Next we tested the behavior of the z functions for fixed ℓ and a progression of ω values. These results appear in Fig. 3.3. Looking at these graphs we affirm that as ω becomes large the results for z^p and z^q again become the same as the approximation. In addition, we see that as ω is increased, the z functions become closer to zero for all distances from the event horizon, as they should based on Eq. (3.8). In Fig. 3.3(d) the three respective data curves overlap for both the $\omega = 5.0$ and $\omega = 9.0$ cases. Lastly, we have checked that the expected results for the z's of ERN are attained when both ω and ℓ are increased. These results are shown in Fig. 3.4 below. Note that the only place where three curves can be resolved at this accuracy is the first case where $\omega = 0.00005$ and $\ell = 1$ in Fig. 3.4(a). A nice progression can be seen with the z's again in agreement with the approximate solution. Another important

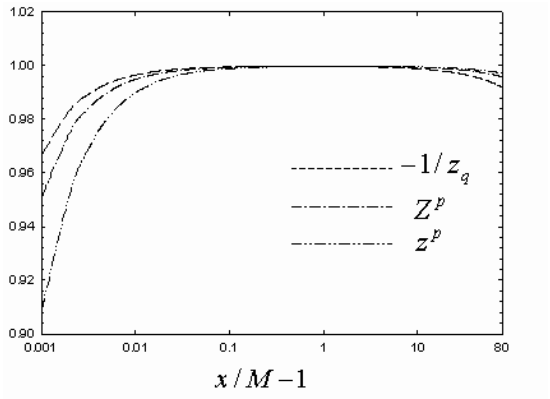

(a) $\omega = 5 \times 10^{-5}$ and $\ell = 1$.

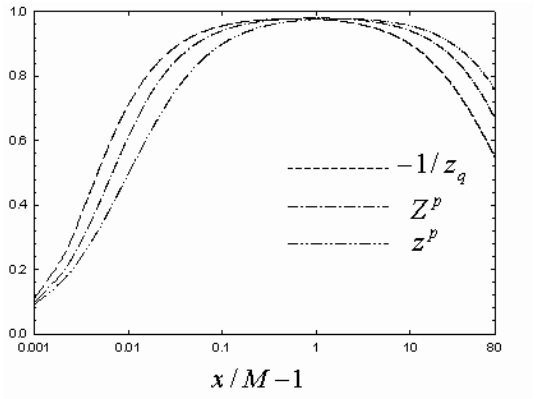

(b) $\omega = 5 \times 10^{-3}$ and $\ell = 1$.

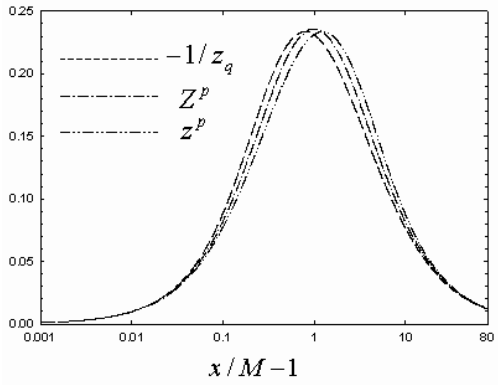

(c) $\omega = 0.5$ and $\ell = 1$.

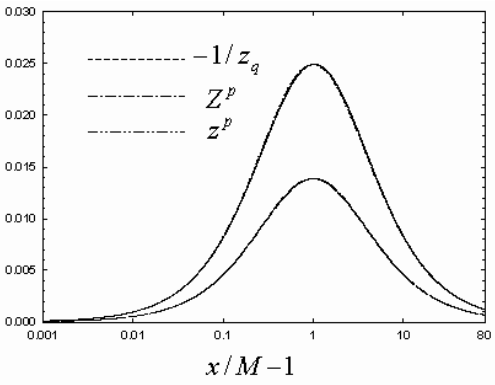

(d) $\omega = 5.0$ (top curve) and $\omega = 9.0$ (bottom curve) both with $\ell = 1$.

Figure 3.3: The z^p, $-1/z^q$, and the approximation Z^p for the ERN black hole plotted as a function of distance from the event horizon for $\ell = 1$ and progressively increasing ω.

result to point out is that the earlier claim that $0 < z^p(r) \leq 1$ and $\infty < z^q(r) \leq -1$ has been numerically verified as can be seen in the presented graphs.

3.1.3 The $z^p(r)$ solution: wormholes

Instead of determining a recursion relation to determine the solution at small r for each of the three wormholes studied in this work, we determine a boundary condition relating the $z^q(r)$ solution and the $z^p(r)$ solution used to calculate the $z^p(r)$ solution at the wormhole's throat $r = r_0$. Then the value of $z^p(r)$ at the throat can be integrated upwards to the next r value we want and so on using the same technique described earlier for ERN. One can begin by recalling the solutions to the Euclidean

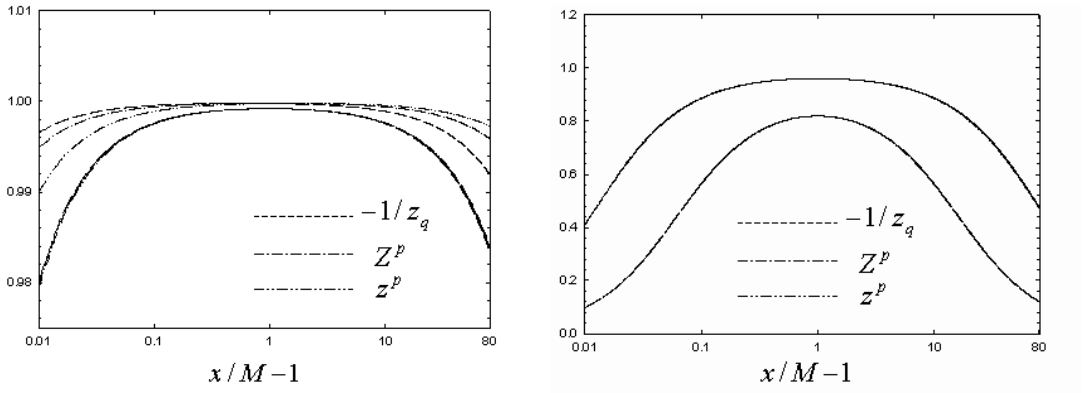

(a) $\omega = 0.00005$, $\ell = 1$ (top three curves) and $\omega = 0.005$, $\ell = 25$ (bottom curves).

(b) $\omega = 0.5$, $\ell = 50$ (top curves) and $\omega = 5.0$, $\ell = 100$ (bottom curves).

Figure 3.4: The z^p, $-1/z^q$, and the approximation Z^p for the ERN black hole plotted as a function of distance from the event horizon for progressively increasing ω and ℓ.

Dirac equation for massless fermions

$$\begin{aligned} \psi_1(x) &= \frac{e^{i\omega\tau}}{rf^{1/4}} \begin{pmatrix} F_{\omega,j}(r)\Psi^m_{j,+}(\theta,\phi) \\ G_{\omega,j}(r)\Psi^m_{j,-}(\theta,\phi) \end{pmatrix} \\ \psi_2(x) &= \frac{e^{i\omega\tau}}{rf^{1/4}} \begin{pmatrix} G_{\omega,j}(r)\Psi^m_{j,-}(\theta,\phi) \\ F_{\omega,j}(r)\Psi^m_{j,+}(\theta,\phi) \end{pmatrix}, \end{aligned} \tag{3.26}$$

where

$$\begin{aligned} \Psi^m_{j,+}(\theta,\phi) &= \begin{pmatrix} \sqrt{\frac{j+m}{2j}}Y^{m-1/2}_{j-1/2} \\ \sqrt{\frac{j-m}{2j}}Y^{m+1/2}_{j-1/2} \end{pmatrix} \\ \Psi^m_{j,-}(\theta,\phi) &= \begin{pmatrix} \sqrt{\frac{j+1-m}{2j+2}}Y^{m-1/2}_{j+1/2} \\ -\sqrt{\frac{j+1+m}{2j+2}}Y^{m+1/2}_{j+1/2} \end{pmatrix}. \end{aligned} \tag{3.27}$$

These solutions are both valid for each mouth of the wormhole, as we shall see solution $\psi_1(x)$ on one mouth of the wormhole will connect smoothly to $\psi_2(x)$ on the other side. Imagine an observer travelling in mouth one toward the wormhole's throat. In mouth one the observer has a right-handed Cartesian coordinate system, but when she crosses the throat and enters mouth two, her coordinate system changes to a left-handed Cartesian coordinate system. Locally the spherical coordinate unit vector $\hat{r}$ changes to $-\hat{r}$ while $\hat{\theta}$, and $\hat{\phi}$ remain unchanged at $r = r_0$. This corresponds in quantum field theory to a local parity transformation combined with a 180° rotation around the $\hat{r}$ axis. A local parity transformation [74] is accomplished by multiplying

our respective solution $\psi(x)$ by $\eta\gamma^0$, where η is an arbitrary phase and γ^0 is one of the Dirac matrices from Eq. (2.3).

A general rotation of a spinor field by an angle α in the $\hat{r}$ direction is handled by multiplying the spinor by [74]

$$\exp\left(\frac{i}{2}\vec{\alpha}\cdot\vec{\Sigma}\right), \tag{3.28}$$

where $\vec{\alpha} = \alpha\hat{r}$, and

$$\vec{\Sigma} = \begin{pmatrix} \vec{\sigma} & \mathbf{0} \\ \mathbf{0} & \vec{\sigma} \end{pmatrix}. \tag{3.29}$$

In Eq. (3.29) $\vec{\sigma}$ indicates

$$\vec{\sigma} = \sigma_1\hat{x} + \sigma_2\hat{y} + \sigma_3\hat{z}. \tag{3.30}$$

We can determine a more explicit form for Eq. (3.28) to be implemented in our analysis at this point. First substitute $\vec{\alpha} = \alpha\hat{r}$ into Eq. (3.28) and utilize the series expansion of e^x we arrive at

$$\exp\left(\frac{i}{2}\alpha\hat{r}\cdot\vec{\Sigma}\right) = \sum_{n=0}^{\infty}\frac{1}{n!}\left(\frac{i\alpha}{2}\right)^n\left(\hat{r}\cdot\vec{\Sigma}\right)^n. \tag{3.31}$$

We now wish to now write Eq. (3.31) in a more useful form, since it contains an infinite sum. We define

$$\mathbf{S}^n \equiv \left(\hat{r}\cdot\vec{\Sigma}\right)^n, \tag{3.32}$$

for the sake of brevity in the following discussion. Notice that if $n = 0$ or $n = 1$, $\mathbf{S}^n$ is $\mathbf{1}$ or $\mathbf{S}$ respectively. Now let's consider the case $n = 2$. From the definitions of $\hat{r}$ and $\vec{\sigma}$ we can work out

$$\mathbf{S}^2 = \mathbf{1}, \tag{3.33}$$

the 4×4 identity matrix. For $n = 3$ we get

$$\mathbf{S}^3 = \mathbf{S}\cdot\mathbf{S}^2 = \mathbf{S}. \tag{3.34}$$

Following this line of logic we can conclude that

$$\begin{aligned} \mathbf{S}^n &= \mathbf{1}, \quad \text{if} \quad n = 0, 2, 4, 6, \ldots, \\ \mathbf{S}^n &= \mathbf{S}, \quad \text{if} \quad n = 1, 3, 5, 7, \ldots. \end{aligned} \tag{3.35}$$

Breaking the infinite sum of Eq. (3.31) into even and odd parts and using the relations in Eq. (3.35) yields

$$\begin{aligned}
\exp\left(\frac{i}{2}\alpha\hat{r}\cdot\vec{\Sigma}\right) &= \sum_{n_{\text{even}}}^{\infty}\frac{1}{n!}\left(\frac{i\alpha}{2}\right)^n+\sum_{n_{\text{odd}}}^{\infty}\frac{1}{n!}\left(\frac{i\alpha}{2}\right)^n(\hat{r}\cdot\vec{\Sigma}) \\
&= \left[1-\frac{(\alpha/2)^2}{2!}+\frac{(\alpha/2)^4}{4!}-\cdots\right] \\
&+ i\left[\frac{\alpha}{2}-\frac{(\alpha/2)^3}{3!}+\frac{(\alpha/2)^5}{5!}\cdot..\right](\hat{r}\cdot\vec{\Sigma}). \qquad (3.36)
\end{aligned}$$

We Recognize that the first term in brackets is $\cos\left(\frac{\alpha}{2}\right)$ and the second is $\sin\left(\frac{\alpha}{2}\right)$, hence the general expression for the quantity used to rotate a spinor field around the $\hat{r}$ axis by an angle α is

$$\cos\left(\frac{\alpha}{2}\right)+i\sin\left(\frac{\alpha}{2}\right)(\hat{r}\cdot\vec{\Sigma}). \qquad (3.37)$$

For our case specifically $\alpha=\pi$ leaving simply $i\left(\hat{r}\cdot\vec{\Sigma}\right)$ for the transformation.

If we combine the rotation of our spinor field and the parity transformation into a single transformation M we have

$$\begin{aligned}
M &\equiv i\eta\gamma^0\left(\hat{r}\cdot\vec{\Sigma}\right)=i\eta\begin{pmatrix}1&0\\0&-1\end{pmatrix}\begin{pmatrix}\tilde{\sigma}&0\\0&\tilde{\sigma}\end{pmatrix} \\
&= i\eta\begin{pmatrix}\tilde{\sigma}&0\\0&-\tilde{\sigma}\end{pmatrix}, \qquad (3.38)
\end{aligned}$$

where we have defined the matrix $\tilde{\sigma}$ to be $(\hat{r}\cdot\vec{\sigma})$. It can be shown that [30]

$$\tilde{\sigma}\Psi^m_{j,\pm}=\Psi^m_{j,\mp}. \qquad (3.39)$$

The boundary condition between the two solutions of the massless Euclidean Dirac equation at the throat of the wormhole is therefore

$$M\Psi_1(x)|_{r=r_0}=\Psi_2(x)|_{r=r_0}. \qquad (3.40)$$

Utilizing the transformation matrix M derived above and the identity from Eq. (3.39), we arrive at

$$\begin{aligned}
i\eta F_1(r_0) &= G_2(r_0), \\
i\eta G_1(r_0) &= -F_2(r_0). \qquad (3.41)
\end{aligned}$$

Recall that we look for two solutions each for F and G, specifically the p solution that is finite near the inner boundary and the q solution that is finite at $r=\infty$.

Both the p and q solutions must solve the massless Euclidean Dirac equation for both mouths of the wormhole, so we will arbitrarily call the mouth 1 solution above q and the mouth 2 solution above p. Explicitly written out we have

$$\begin{aligned} i\eta F^q(r_0) &= G^p(r_0), \\ i\eta G^q(r_0) &= -F^p(r_0). \end{aligned} \tag{3.42}$$

Recall at this point our definition of our mode solutions for $z^p(r_0)$ and $z^q(r_0)$ in terms of the F and G functions from Eq. (3.6)

$$z^p(r_0) = \frac{F^p(r_0) - G^p(r_0)}{F^p(r_0) + G^p(r_0)}, \tag{3.43}$$

and

$$z^q(r_0) = \frac{F^q(r_0) - G^q(r_0)}{F^q(r_0) + G^q(r_0)}. \tag{3.44}$$

We can now take advantage of the boundary condition at the throat (Eq. (3.42)), and find the desired boundary condition for the $z(r)$ solutions at the throat:

$$z^p(r_0) = -\frac{1}{z^q(r_0)}. \tag{3.45}$$

Notice that the arbitrary phase η has now been removed from the problem. In addition there is a remarkable similarity to Eq. (3.9).

The method for finding the $z^p(r)$ and $z^q(r)$ solutions for wormholes has been completely described. We find the $z^q(r)$ solutions as detailed above for every value of r that interests us by integrating Eq. (3.7) downwards until we reach $r = r_0$. We then apply the boundary condition in Eq. (3.45) to find $z^p(r_0)$, and then integrate this solution upwards to find the value of $z^p(r)$ at every value of r desired. Notice that all the integration is performed on one side of the wormhole throat. Thanks to the boundary condition we determined, there is no need to integrate over to the other mouth of the wormhole.

The $z^p(r)$ and $z^q(r)$ functions were numerically computed as a function of distance from the throats of the wormholes in question. The numerical results for the z's are very qualitatively similar and exhibit the same trend, so we will be satisfied with only showing data for case 3, the proximal Schwarzschild wormhole. The radial coordinate was transformed in this, and all of the wormhole cases studied, such that Eq. (3.7) was easier to handle for numerical integration. This is done because r is a bad coordinate

at the throat, causing an apparent singularity. Our solution was to redefine the radial coordinate in a way that made both terms in Eq. (3.7) finite at the wormhole's throat. To see the utility of this substitution first recall the metric functions for the proximal Schwarzschild wormhole spacetime from Chapter 1:

$$f(x) = \left(1 - \frac{r_0}{x} + \frac{\epsilon r_0^2}{x^2}\right) \qquad \text{and} \qquad h(x) = \left[1 - \frac{x}{r_0}\right]^{-1}. \tag{3.46}$$

Substitution of these metric functions into Eq. (3.7) yields

$$\frac{dz(r)}{dr} = \frac{\ell}{r}\sqrt{\frac{r}{r-1}}\left(1 - z^2(r)\right) - 2\omega r z(r)\sqrt{\frac{r}{(r^2 - r + \epsilon)(r-1)}}, \tag{3.47}$$

where again $r = x/r_0$. Notice that both terms in this differential equation diverge at $r = 1$. This divergence is removed by the above described switch to a new radial coordinate s. We implemented

$$s = \left(1 + \sqrt{r-1}\right)^2, \tag{3.48}$$

which is by no means unique, but was satisfactory. Then placing the above definition into Eq. (3.47) yields

$$\frac{dz(s)}{ds} = \frac{\ell}{\sqrt{r}}\frac{(1 - z^2(s))}{\sqrt{r-1}+1} - 2\omega z(s)\left(\frac{r}{\sqrt{r-1}+1}\right)\sqrt{\frac{r}{r^2 - r + \epsilon}}, \tag{3.49}$$

which is well behaved at the wormhole's throat ($s = r = 1$).

The actual parameters utilized in the numerical computation of the $z(r)$ functions for the proximal Schwarzschild wormhole included 136 scaled distances from the throat including values of s from 1.0 (the throat radius) to 10.0. This corresponds to a range of x/r_0 of 1.0 to 5.67. Similar to the ERN computations, over 5000 ω values were included spanning $\omega = 0.00001$ to 20.0. Lastly, we utilized $\ell = 1$ to 200, and like the ERN calculations we found that going to $\ell = 100$ was sufficient. A value of 0.10 was implemented for the small parameter ϵ. Numerical results for z^p, $-1/z^q$, and the approximation Z^q for the proximal Schwarzschild wormhole appear below. Figures 3.5 and 3.6 display the progression of the z functions as ℓ is increased at fixed ω and the progression of the z functions as ω is increased at fixed ℓ respectively. Lastly, Fig. 3.7 contains the computed z functions for progressively increasing ω and ℓ. Again we found that our approximation for the $z(r)$ functions was confirmed by the behavior of ℓ and ω or both at large values just like in the ERN spacetime

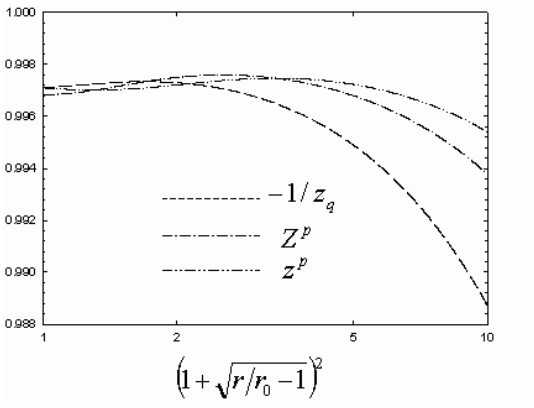

(a) $\ell = 1$.

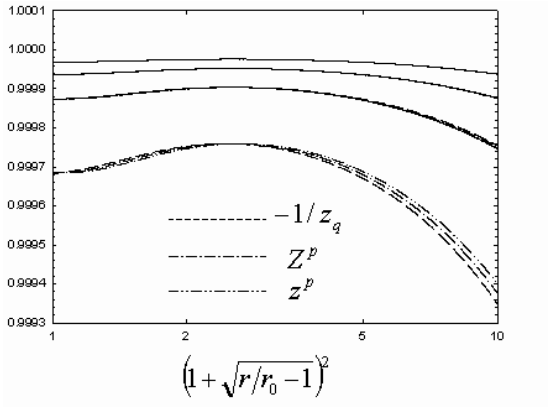

(b) Starting from the bottom set of curves: $\ell =$ 10, 25, 50, and 100.

Figure 3.5: The z^p, $-1/z^q$, and the approximation Z^p for the proximal Schwarzschild wormhole at $\omega = 0.001$ plotted as a function of distance from the throat for progressively increasing ℓ.

calculations and the other two wormholes in question as well. We therefore concluded that our results thus far could be relied upon. These results will be implemented in the calculation of $\langle T_{\mu\nu} \rangle_{\text{modes}}$ after the full WKB expansion for the mode functions is discussed.

3.2 The WKB expansion for $\langle T_\mu{}^\nu(x) \rangle_{\text{WKB}}$

Let us tackle the method in which we determined the WKB-like expansions for the full stress-energy tensor. This requires finding a WKB expansion that can be employed iteratively for $z^p(r)$ and $z^q(r)$. The general scheme is to write $z(r)$ in terms of another function $\theta(r)$ that can be expanded and iterated to whatever order desired. The function $\theta(r)$ will be written in terms of an approximation $\phi(r)$. The first order WKB expansion of $\theta(r)$ will have the form

$$\theta_1(r) = \phi(r) + K\left[\phi(r)\right], \tag{3.50}$$

in which K is an as of yet unspecified operator which we substitute $\theta_0(r)$ into. We can now generalize our nth order WKB expansion for $\theta(r)$ as

$$\theta_n(r) = \phi(r) + K\left[\theta_{n-1}(r)\right], \tag{3.51}$$

where $n \geq 1$, and $\theta_0(r) = \phi(r)$.

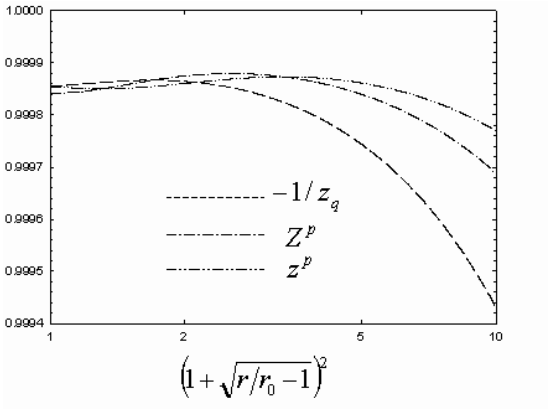

(a) $\omega = 5 \times 10^{-5}$ and $\ell = 1$.

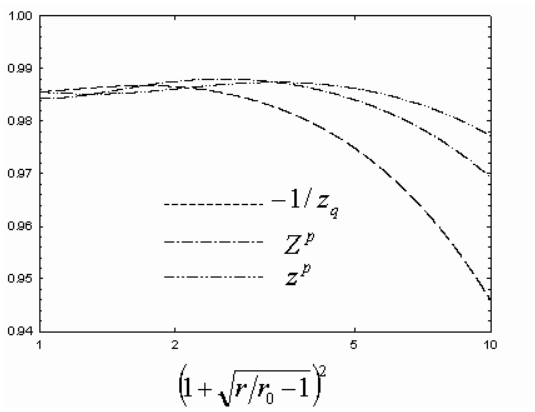

(b) $\omega = 5 \times 10^{-3}$ and $\ell = 1$.

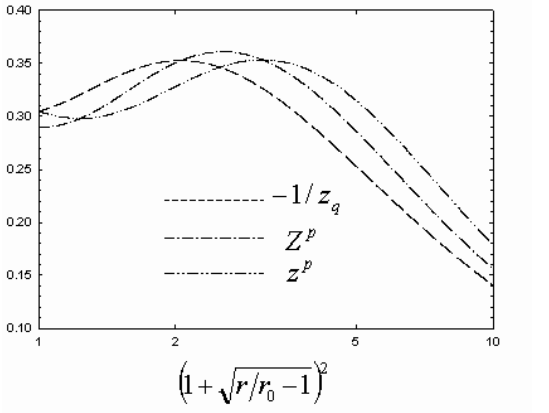

(c) $\omega = 0.5$ and $\ell = 1$.

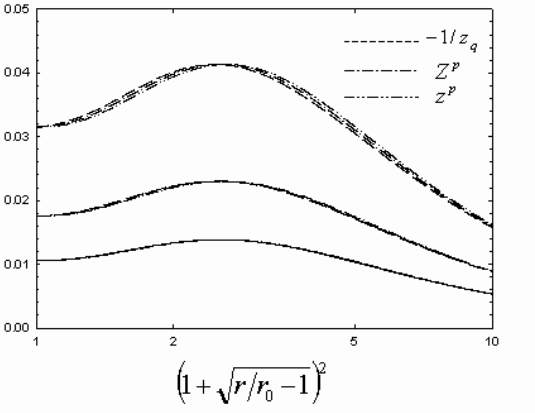

(d) Starting with the top set of curves: $\omega = 5.0$, 10.0, and $\omega = 15.0$ all with $\ell = 1$.

Figure 3.6: The z^p, $-1/z^q$, and the approximation Z^p for the proximal Schwarzschild wormhole plotted as a function of distance from the throat for $\ell = 1$ and progressively increasing ω.

Next we shall recast the differential equation for the $z(r)$ functions (Eq. (3.7)) in yet another form by defining new relations that depend on the metric functions $f(r)$ and $h(r)$. With the definitions

$$g(r) \equiv \frac{f(r)}{h(r)} \quad \text{and} \quad v(r) \equiv \frac{\sqrt{f(r)}}{r}, \tag{3.52}$$

Eq. (3.7) becomes

$$\frac{dz(r)}{dr} = \frac{\ell\, v(r)}{\sqrt{g(r)}}\left(1 - z^2(r)\right) - \frac{2\omega}{\sqrt{g(r)}} z(r). \tag{3.53}$$

The implementation of the new functions $g(r)$ and $v(r)$ wasn't a necessity, it just simplified the coding in the first computation performed, ERN, in which $f(r) =$

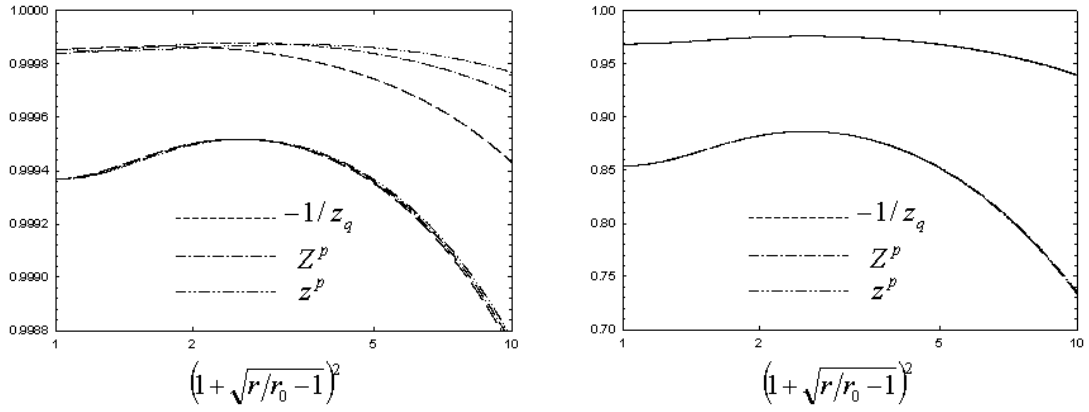

(a) $\omega = 0.00005$, $\ell = 1$ (top three curves) and $\omega = 0.005$, $\ell = 25$ (bottom set of curves).

(b) $\omega = 0.5$, $\ell = 50$ (top curves) and $\omega = 5.0$, $\ell = 100$ (bottom curves).

Figure 3.7: The z^p, $-1/z^q$, and the approximation Z^p for the proximal Schwarzschild wormhole plotted as a function of distance from the throat for progressively increasing ω and ℓ.

$1/h(r)$. To continue, let us define $\theta(r)$ as:

$$z(r) \equiv \tan\left(\frac{\theta(r)}{2}\right) = \frac{\sin\left[\theta(r)\right]}{1+\cos\left[\theta(r)\right]}. \tag{3.54}$$

Notice that the range of $z(r)$ required by earlier discussions is preserved if we restrict $\theta(r)$ to the domain $-\pi \leq \theta(r) \leq \pi$. This retains the range of $z(r)$ as $-\infty \leq z(r) \leq \infty$. The extension to determining the separate p and q solutions is achieved by now splitting the above domain for $\theta(r)$ into a range for $z^p(r)$ and $z^q(r)$; in particular, $0 < \theta^p(r) \leq \frac{\pi}{2}$ and $-\pi < \theta^q(r) \leq -\frac{\pi}{2}$, respectively. We will also need the derivative with respect to r of Eq. (3.54)

$$\frac{dz(r)}{dr} = \frac{1}{2}\sec^2\left(\frac{\theta(r)}{2}\right)\frac{d\theta(r)}{dr}. \tag{3.55}$$

Now we substitute Eq. (3.54) and its derivative into Eq. (3.53), eliminating $z(r)$ in favor of $\theta(r)$. After some rearranging of terms and making use of the half angle formulas for the sine and cosine functions

$$\begin{aligned} \cos\frac{\theta}{2} &= \sqrt{\frac{1}{2}\left(1+\cos\theta\right)}, \\ \sin\frac{\theta}{2} &= \sqrt{\frac{1}{2}\left(1-\cos\theta\right)}, \end{aligned} \tag{3.56}$$

we arrive at

$$\frac{\sqrt{g(r)}}{2}\frac{d\theta(r)}{dr} = v(r)\ell\cos\left[\theta(r)\right] - \omega\sin\left[\theta(r)\right]. \tag{3.57}$$

The introduction of our approximation $\phi(r)$ is achieved by the substitutions

$$\cos[\phi(r)] \equiv \frac{\omega}{N(r)}, \quad \text{and} \quad \sin[\phi(r)] \equiv \frac{v(r)\ell}{N(r)}, \tag{3.58}$$

where $N(r)$ is explicitly determined by utilizing the trigonometric identity $\cos^2[\phi(r)] + \sin^2[\phi(r)] = 1$ and solving for $N(r)$. The function $N(r)$ is hence known, and is simply

$$N(r) = \sqrt{v^2(r)\ell^2 + \omega^2}. \tag{3.59}$$

If we take the ratio of the two relationships for $\phi(r)$ given in Eq. (3.58) we readily obtain an explicit expression for the zeroth order WKB approximation

$$\phi(r) = \tan^{-1}\left(\frac{v(r)\ell}{\omega}\right). \tag{3.60}$$

It will be important for a later discussion to note that $\phi(r)$ strictly falls in the domain $0 < \phi < \frac{\pi}{2}$, because $v(r)$, ℓ, and ω are always positive. We can now recast Eq. (3.57) by substituting the $\phi(r)$ relationships from Eq. (3.58) arriving at

$$\begin{aligned}\frac{\sqrt{g(r)}}{2}\frac{d\theta(r)}{dr} &= N(r)\sin\left[\phi(r)\right]\cos\left[\theta(r)\right] - N(r)\cos\left[\phi(r)\right]\sin\left[\theta(r)\right], \\ &= N(r)\sin\left[\phi(r) - \theta(r)\right].\end{aligned} \tag{3.61}$$

Then solving for $\theta(r)$ we obtain the result

$$\theta(r) = \phi(r) - \sin^{-1}\left(\frac{\sqrt{g(r)}}{2N(r)}\frac{d\theta(r)}{dr}\right), \tag{3.62}$$

which has the desired form of Eq. (3.51). Notice that the zeroth order solution to our expansion would simply be $\theta(r) \approx \phi(r)$, with the zeroth order approximations for $z^p(r)$ or $z^q(r)$ given by Eq. (3.54) with the appropriate range for $\theta(r)$.

To perform the WKB expansion in Eq. (3.62), we include an expansion parameter a so that

$$\theta(r) = \phi(r) - \sin^{-1}\left(\frac{a\sqrt{g(r)}}{2N(r)}\frac{d\theta(r)}{dr}\right), \tag{3.63}$$

Then $\sin^{-1}\left(\frac{a\sqrt{g(r)}}{2N(r)}\frac{d\theta(r)}{dr}\right)$ is expanded in a polynomial series around $a = 0$ (Maclaurin Series) using symbolic manipulation software yielding a power series in a. The series

expansion utilized for $\sin^{-1}(x)$ is explicitly [88]

$$\sin^{-1}(x) = x + \sum_{n=1}^{\infty} \frac{1 \cdot 3 \cdot 5 \cdots (2n-1)}{2 \cdot 4 \cdot 6 \cdots (2n)} \cdot \frac{x^{2n+1}}{2n+1}, \tag{3.64}$$

when $|x| < 1$. Then Eq. (3.63) is repeatedly substituted into itself continuing to expand in powers of a with each iteration. This must only be done a finite number of times, since the expansion of the arcsine function gives repeated powers of a. We then obtain a power series in inverse powers of $N(r)$.

The q solution for $\theta(r)$ can be found by first realizing that arcsine is a double valued function, therefore if we replace $\sin^{-1}(x)$ with $\pi - \sin^{-1}(x)$ in Eq. (3.62) we obtain

$$\theta(r) = \phi(r) - \pi + \sin^{-1}\left(\frac{a\sqrt{g(r)}}{2N(r)}\frac{d\theta(r)}{dr}\right), \tag{3.65}$$

which has the desired domain. Notice that as we iteratively substitute into this equation the π vanishes from the derivative term inside the arcsine, so in effect the only thing we are doing is letting $\phi(r) \to \phi(r) - \pi$ and $a \to -a$.

We utilized Maple in the actual procedure to get the WKB expansions for $z^p(r)$ and $z^q(r)$ in the following way. We recursively expanded the above expressions for $\theta^p(r)$ and $\theta^q(r)$ eight times using Eq. (3.58) to replace cosine and sine functions of $\phi(r)$ for the p solution, and

$$\cos[\phi(r)] = -\frac{\omega}{N(r)}, \quad \sin[\phi(r)] = -\frac{v(r)\ell}{N(r)}, \tag{3.66}$$

and $a \to -a$ for the cosine and sine functions for the q solution. The minus signs in Eq. (3.66) come from the fact that in the q solution, we let $\phi(r) \to \phi(r) - \pi$. In addition, at each iteration $N(r)$ and its first derivative appear as well as the first derivative of $\phi(r)$. These are replaced at each step in terms of ℓ, $v(r)$, and ω using the above relationship for $N(r)$ (Eq. (3.59)), and its first derivative

$$\frac{dN(r)}{dr} = \frac{\ell^2 v(r)}{N(r)}\frac{dv(r)}{dr}, \tag{3.67}$$

and

$$\frac{d\phi(r)}{dr} = \frac{\ell\omega}{N^2(r)}\frac{dv(r)}{dr}. \tag{3.68}$$

These expressions are easily verified from the preceding equations. With the WKB-like expansions for the $\theta(r)$ functions in hand we then substituted them into

$$z(r) = \frac{\sin\theta(r)}{1 + \cos\theta(r)}, \tag{3.69}$$

to determine the expansions for $z^p(r)$ and $z^q(r)$. As will be shown soon, the following combinations of $z^p(r)$ and $z^q(r)$ are necessary to determine $\langle T_\mu{}^\nu(x)\rangle_{\rm modes}$:

$$\frac{z^p + z^q}{z^p - z^q}, \tag{3.70}$$

$$\frac{1 - z^p z^q}{z^p - z^q}, \tag{3.71}$$

therefore these two expressions were then expanded in powers of a. Then in the end the expansion parameter a is set to one. This expansion results in leading order terms followed by terms that only contain even powers of a. The highest power of a present corresponded to the order of the WKB-like approximation used. Only including the zeroth order term makes the sums on ℓ convergent, if enough values of ℓ are implemented, but leaves the integrals over ω divergent. Including up to the fourth order term is just enough to make the integrals over ω converge. In our calculations, we implemented an eighth order expansion to allow for high accuracy without having to use more ℓ values. We also computed the sixth order expansion for comparison. No significant difference was seen in the results for $\langle T_\mu{}^\nu(x)\rangle_{\rm modes}$, to the limits of quadruple precision, in the implementation of the sixth versus the eight order expansion. We obtained polynomials in powers of r, ω, ℓ, and the functions $g(r)$ and $v(r)$ and their derivatives divided by powers of $N(r)$. Explicit expressions for these extremely lengthy results will not be shown. These terms were then outputted from Maple in Fortran code format for computing ease.

3.3 The calculation of $\langle T_\mu{}^\nu(x)\rangle_{\rm modes}$

We need to write our previous expressions for the functions A_1 and A_2 (Eq. (2.66)) in terms of the $z(r)$ functions so that the data generated for the $z(r)$ functions is easily utilized in determining $\langle T_\mu{}^\nu(x)\rangle_{\rm unren}$ and to use with our WKB-like expansion for $\langle T_\mu{}^\nu(x)\rangle_{\rm WKB}$. This is achieved by writing the A's in a slightly different form. We can shift the sums on ℓ on the first term in the relation for A_1 to $\ell + 1$ and find after some manipulation that

$$A_1 = \frac{r}{2\sqrt{f}} + \sum_{\ell=1}^{\infty}\left[\ell\left(F^p_{\omega,\ell-1/2}F^q_{\omega,\ell-1/2} - G^p_{\omega,\ell-1/2}G^q_{\omega,\ell-1/2}\right) + \frac{r}{\sqrt{f}}\right]. \tag{3.72}$$

Similarly we can shift the sums on ℓ to $\ell - 1$ on all terms except the second in the equation for A_2 above and employ the Wronskian condition

$$\omega[G^q_{\omega,\ell}(r)F^p_{\omega,\ell}(r) - F^q_{\omega,\ell}(r)G^p_{\omega,\ell}(r)] = 1, \tag{3.73}$$

to get

$$A_2 = \frac{\omega r^2}{4f} + \sum_{\ell=1}^{\infty}\left[\ell^2\left(G^q_{\omega,\ell-1/2}F^p_{\omega,\ell-1/2} + F^q_{\omega,\ell-1/2}G^p_{\omega,\ell-1/2}\right) - \frac{\ell^2}{\omega} + \frac{\omega r^2}{2f}\right]. \tag{3.74}$$

After some algebraic manipulations, and again taking advantage of the Wronskian and Eq. (3.6), one finally arrives at the following results for the functions A_1 and A_2 in terms of $z^p(r)$ and $z^q(r)$

$$A_1 = \frac{r}{2\sqrt{f}} + \frac{1}{\omega}\sum_{\ell=1}^{\infty}\left[\ell\left(\frac{z^p + z^q}{z^p - z^q}\right) + \frac{r}{\sqrt{f}}\right], \tag{3.75}$$

$$A_2 = \frac{\omega r^2}{4f} + \frac{1}{\omega}\sum_{\ell=1}^{\infty}\left[\ell^2\left(\frac{1 - z^p z^q}{z^p - z^q} - 1\right) + \frac{\omega r^2}{2f}\right]. \tag{3.76}$$

Notice that the ratios for the $z(r)$ functions in parentheses in Eqs. (3.75) and (3.76) are the same used in the eighth order WKB-like expansion. We therefore define $A_{1\,\mathrm{WKB}}$ and $A_{2\,\mathrm{WKB}}$ as

$$A_{1\,\mathrm{WKB}} = \frac{r}{2\sqrt{f}} + \frac{1}{\omega}\sum_{\ell=1}^{\infty}\left[\ell\left(\frac{z^p + z^q}{z^p - z^q}\right)_{\mathrm{WKB}} + \frac{r}{\sqrt{f}}\right], \tag{3.77}$$

$$A_{2\,\mathrm{WKB}} = \frac{\omega r^2}{4f} + \frac{1}{\omega}\sum_{\ell=1}^{\infty}\left[\ell^2\left(\frac{1 - z^p z^q}{z^p - z^q} - 1\right)_{\mathrm{WKB}} + \frac{\omega r^2}{2f}\right], \tag{3.78}$$

where the subscript WKB on the terms in parentheses denotes the WKB-like expansion used for those quantities.

Substituting Eqs. (3.75), (3.76), (3.77), and (3.78) into Eq. (2.72) we can now write $\langle T_\mu{}^\nu(x)\rangle_{\mathrm{modes}}$ as

$$\langle T_t{}^t(x)\rangle_{\mathrm{modes}} = \frac{1}{\pi^2 r^2}\int_0^\infty a_1 d\omega, \tag{3.79}$$

$$\langle T_r{}^r(x)\rangle_{\mathrm{modes}} = \frac{1}{\pi^2 r^2}\int_0^\infty (a_2 - a_1)\, d\omega \tag{3.80}$$

$$\langle T_\theta{}^\theta(x)\rangle_{\mathrm{modes}} = \langle T_\phi{}^\phi(x)\rangle_{\mathrm{unren}} = -\frac{1}{2\pi^2 r^2}\int_0^\infty a_2 d\omega, \tag{3.81}$$

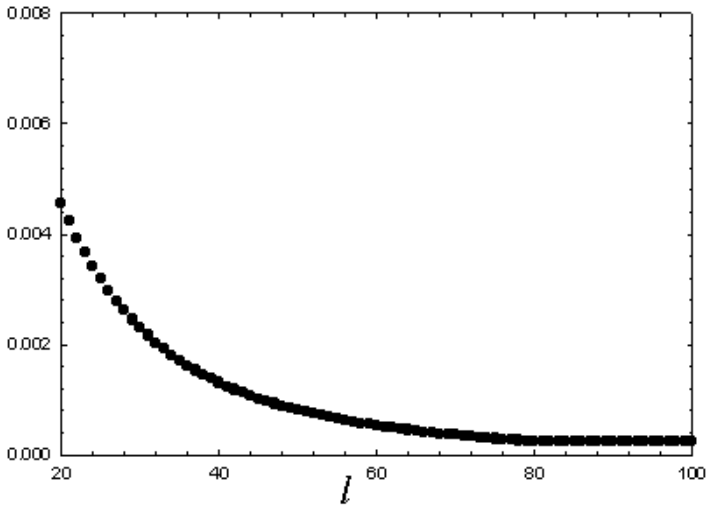

Figure 3.8: The data for the function $a_1\ell^{10}$ (not summed) for the zero tidal force wormhole as a function of ℓ for $\omega = 0.20$ and $s = 4.0$.

where

$$a_1 \equiv \sum_{\ell=1}^{\infty} \frac{\omega\ell}{f}\left[\left(\frac{z^p+z^q}{z^p-z^q}\right) - \left(\frac{z^p+z^q}{z^p-z^q}\right)_{\rm WKB}\right] \tag{3.82}$$

$$a_2 \equiv \sum_{\ell=1}^{\infty} \frac{\ell^2}{r\sqrt{f}}\left[\left(\frac{1-z^pz^q}{z^p-z^q}\right) - \left(\frac{1-z^pz^q}{z^p-z^q}\right)_{\rm WKB}\right] \tag{3.83}$$

Next we shall show numerical results for the summation over ℓ in the above expressions. We will only show results for the sums relevant to $\langle T_t{}^t(x)\rangle_{\rm modes}$ and $\langle T_\theta{}^\theta(x)\rangle_{\rm modes}$, since the sum necessary for $\langle T_r{}^r(x)\rangle_{\rm modes}$ is just a linear combination of the other two. The quantities a_1 and a_2 were numerically summed over ℓ for every ω and r value utilized in computing the $z(r)$ functions previously. To test the convergence of our WKB expansions, we looked at the quantities a_1 and a_2 (without summing over ℓ) at fixed ω and r as a function of ℓ. For eighth order, the WKB expansion terms appearing in Eqs. (3.82) and (3.83) should fall off as $1/\ell^{10}$ for large ℓ. Figure 3.8 shows this behavior for the zero tidal force wormhole displaying $a_1\ell^{10}$. Notice that the results approach a constant value. This observation, and others like it, told us that our procedure for computing the WKB expansion for the mode solutions was working.

Obviously, the infinite sums in Eq. (2.66) must be truncated. The absolute error was estimated as the last term utilized times $\ell/(n+1)$, where n is the order of the WKB expansion implemented [87]. This error was always less than 10^{-20} for distances

close to the event horizon or throat of the relevant black hole or wormhole. It turned out that summing to $\ell = 100$ was sufficient, since after redoing the sums with a cutoff of $\ell = 200$ no difference was observed. The main challenge in computing these sums was clustering the ω values close enough together to allow reliable numerical integration at the next step without using so many that the computations became exceedingly long. In particular at low frequencies ($\omega \ll 1$) this was most important, since the functions a_1 and a_2 vary most rapidly in this region. This choice of ω values was already determined by the data generated for the $z(r)$ functions; therefore, adding more ω values at this step could only be achieved by calculating more values of $z(r)$. This process was repeated until graphs that looked reliably integrable were obtained. This process was checked by only including every other value of ω in the integration, and finding that the end result differed by a fractional error of 10^{-10} or less. We display some of our results for a_1 and a_2 for the extreme Reissner-Nordström black hole and the three wormhole geometries studied in Figs. (3.9), (3.10), (3.11), and (3.12). The functions a_1 and a_2 are shown in these figures only to the point at which they become very small, but we calculated them all out to $\omega = 20.0$ to be sure of convergence for integration. They are all finite at the respective throat for wormholes (or event horizon for ERN) and go to zero as s becomes large. It also can be seen that a_1 and a_2 are nearly equal, and all except the proximal Schwarzschild wormhole exhibit four characteristic extrema in their spectrum. The reason behind this is yet to be understood. Lastly, we found that quantum effects for each gravitational source got smaller and smaller as the distance from the source was increased. This is evident by the area under each of the curves decreasing as s increases for a given gravitational source.

The next task was to evaluate the integrals over ω in Eqs. (3.79), (3.80), and (3.81) numerically using Simpson's rule to obtain the nonzero components of $\langle T_\mu{}^\nu(x)\rangle_{\text{modes}}$ after substitution of the results for a_1 and a_2. Simpson's rule of the definite integral $\int_a^b f(x)dx$ is implemented by partitioning the interval $[a, b]$ into n even equal length subintervals. The approximation is [88, 87]

$$\begin{aligned}\int_a^b f(x)dx &\simeq \frac{\Delta x}{3}\left[f(a) + 4f(a+\Delta x) + 2f(a+2\Delta x) + 4f(a+3\Delta x) + 2f(4\Delta x) + \cdots\right.\\ &+ \left. 2f(a+(n-2)\Delta x) + 4f(a+(n-1)\Delta x) + f(a+n\Delta x)\right], \qquad (3.84)\end{aligned}$$

in which $\Delta x = (b-a)/n$. The only way to get the symmetric pattern of coefficients

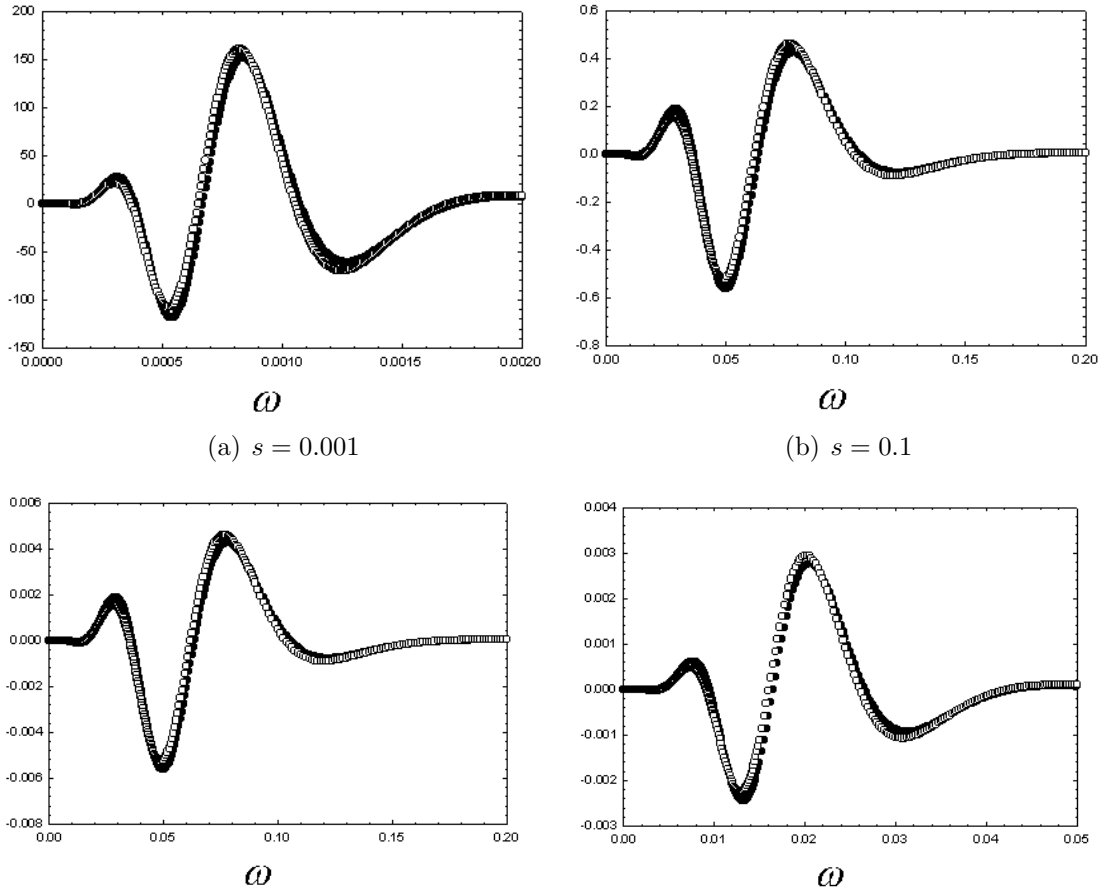

(a) $s = 0.001$ (b) $s = 0.1$

(c) $s = 10.0$ (d) $s = 40.0$

Figure 3.9: The functions a_1 and a_2 for the extreme Reissner-Nordström black hole summed over ℓ as a function of ω for various distances from the event horizon. Here $s = r/M - 1$, and solid dots and open dots are the data for a_1 and a_2 respectively.

in Eq. (3.84) is for n to be even. The number of points in each region was generally at least 10. The numerical integration was truncated such that including the next point would not significantly alter the result. For large values of ω, the contributions to a_1 and a_2 were sometimes so small and difficult to estimate that they made little difference. We terminated the sums whenever these contributions could not be estimated with an accuracy better than one percent. In regions near the event horizon for ERN or throat for the wormholes (within 1 for a given radial coordinate) the absolute errors in $\langle T_\mu{}^\nu(x)\rangle_{\rm modes}$ were always a few orders of magnitude less than for areas much farther away. This lower error is due to the inclusion of many more ω values, and hence smoother integrands in that region. For ERN and the case 1,

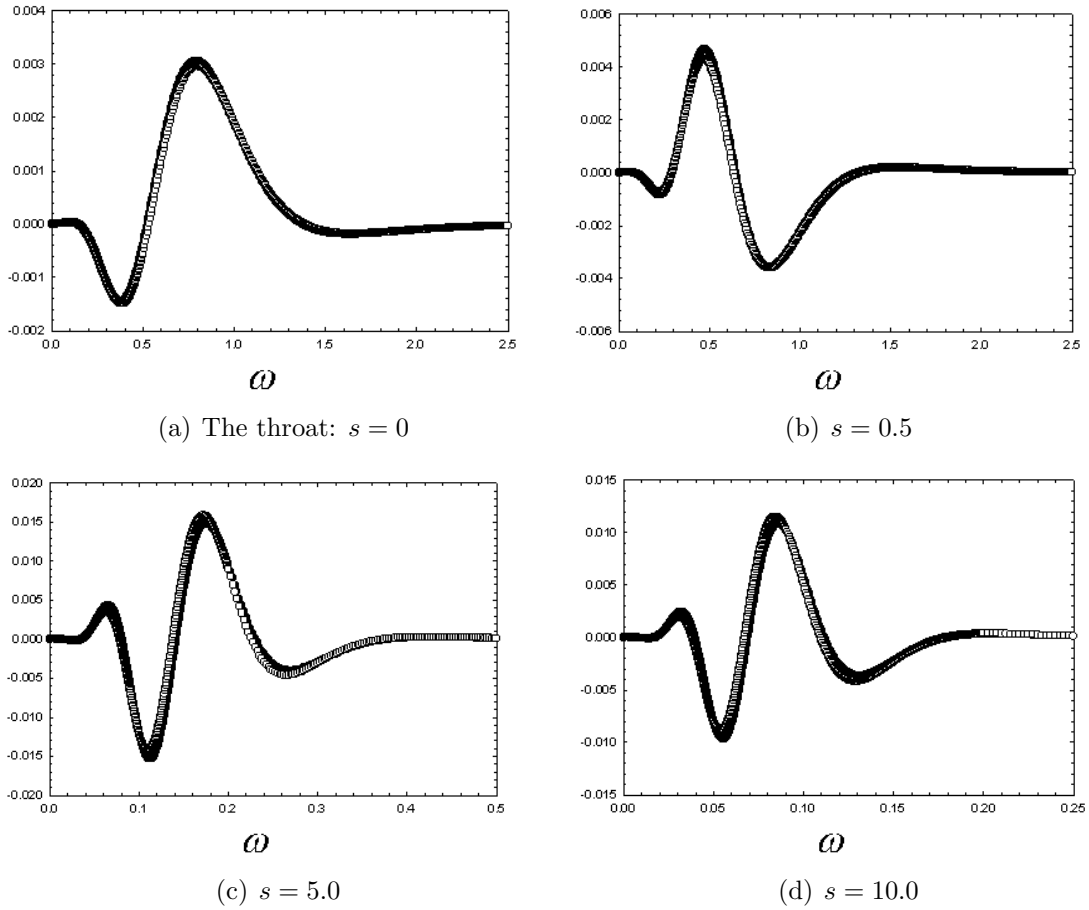

(a) The throat: $s = 0$

(b) $s = 0.5$

(c) $s = 5.0$

(d) $s = 10.0$

Figure 3.10: The functions a_1 and a_2 for the zero tidal force wormhole (case 1) summed over ℓ as a function of ω for various distances from the throat. Here $s = \sqrt{r/r_0 - 1}$, and solid dots and open dots are the data for a_1 and a_2 respectively.

2, and 3 wormholes studied, the absolute errors in $\langle T_\mu{}^\nu(x)\rangle_{\rm modes}$ in the near throat (or event horizon) region were of order $10^{-17}, 10^{-14}, 10^{-12}$, and 10^{-13} respectively. In the far from throat (or event horizon) region the absolute errors in $\langle T_\mu{}^\nu(x)\rangle_{\rm modes}$ for these same objects were of order $10^{-10}, 10^{-11}, 10^{-9}$, and 10^{-8} respectively. In general, errors were greatest for the case 3 proximal Schwarzschild wormhole due to the apparent need to include even more values of ω in the radial mode functions, and hence in the latter integration. Our results for the non-zero components of $\langle T_\mu{}^\nu(x)\rangle_{\rm modes}$ calculated for each spacetime studied in this work appear in Fig. 3.13. In all of these results, the mass for the ERN spacetime and the throat radius for wormholes has been scaled out of the problem appearing as an overall factor at the end. Also, all results have been scaled by the conventional factor of $90(8^4)\pi^2$.

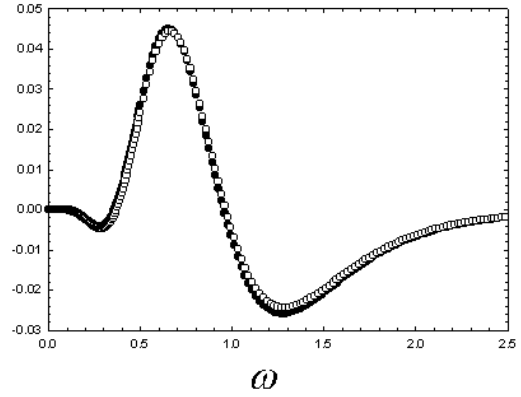

(a) The throat: $s = 1.0$

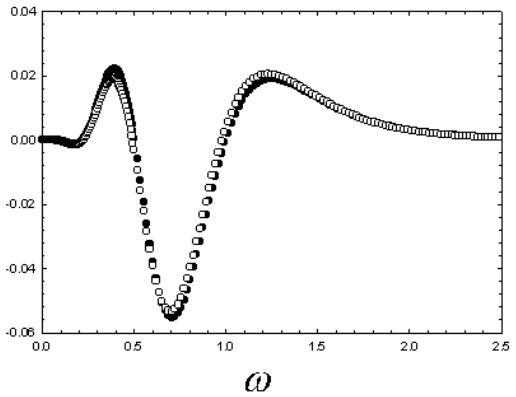

(b) $s = 1.5$

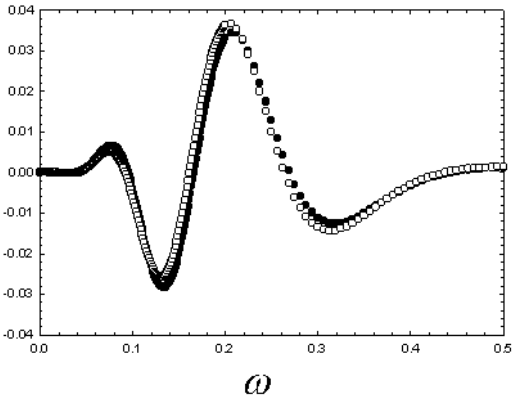

(c) $s = 5.0$

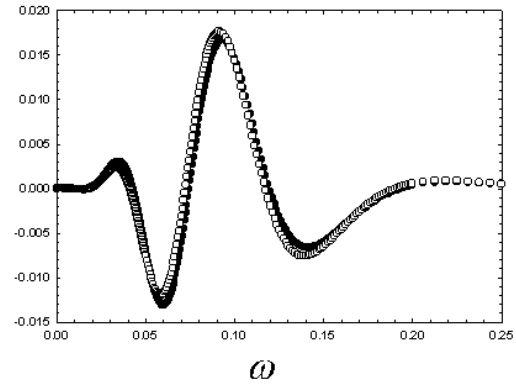

(d) $s = 10.0$

Figure 3.11: The functions a_1 and a_2 for the simple wormhole (case 2) summed over ℓ as a function of ω for various distances from the throat. Here $s = \sqrt{r/r_0 - 1} + 1$, and solid dots and open dots are the data for a_1 and a_2 respectively.

Examining the results for $\langle T_\mu{}^\nu(x)\rangle_{\rm modes}$, we see that as desired this quantity is finite at all distances studied, including near the throats of the wormholes or the event horizon of ERN. In addition, all components fall off to zero at large distances. It is also interesting to note that these results foreshadow our final results for $\langle T_\mu{}^\nu(x)\rangle_{\rm ren}$ in that the energy density is negative close to the object for all the spacetimes except the simple wormhole, since using our sign conventions results in $\rho = -\langle T_t{}^t\rangle$. Recall the only difference between the zero radial tide and simple wormhole is the form of their shape functions $b(r)$, namely $b(r) = r_0$ and $b(r) = r_0^2/r$. This minor difference interestingly changes the sign of each component of $\langle T_\mu{}^\nu(x)\rangle_{\rm modes}$ near the wormhole's throat.

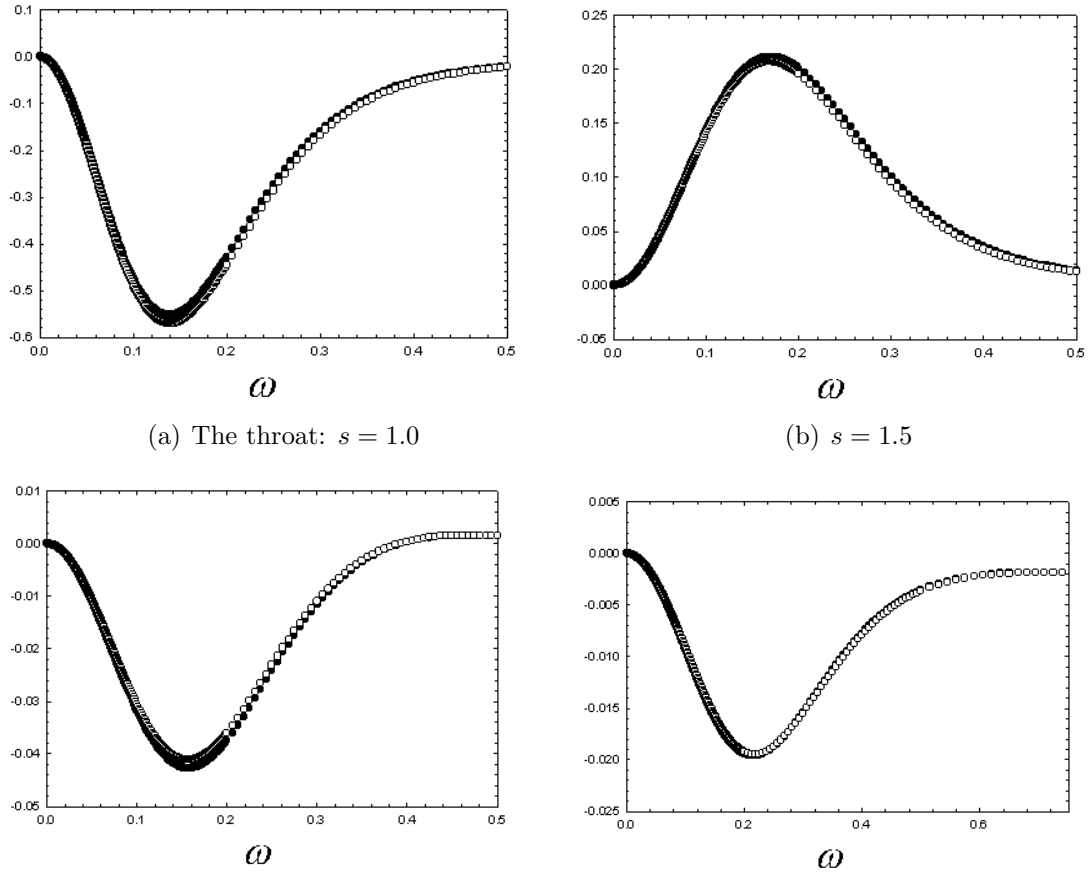

(a) The throat: $s = 1.0$

(b) $s = 1.5$

(c) $s = 2.0$

(d) $s = 2.5$

Figure 3.12: The functions a_1 and a_2 for the proximal Schwarzschild wormhole (case 3) summed over ℓ as a function of ω for various distances from the throat. Here $s = \left(\sqrt{r/r_0 - 1} + 1\right)^2$, and solid dots and open dots are the data for a_1 and a_2 respectively.

3.4 Results for $\langle T_\mu{}^\nu(x)\rangle_{\rm WKBfin}$

Now, with the procedure completed to determine the eighth order WKB-like expansion for the mode functions, the numerical results for the quantity $\langle T_\mu{}^\nu(x)\rangle_{\rm WKBfin}$ were determined. Recalling Eq. (2.73), for $\langle T_\mu{}^\nu(x)\rangle_{\rm WKBfin}$ and Eqs. (3.77) and (3.78) for $A_{1\,\rm WKB}$ and $A_{2\,\rm WKB}$, the sums over ℓ and integration over ω are done analytically. The results for $\langle T_\mu{}^\nu(x)\rangle_{\rm WKBfin}$ appear in Fig. 3.14. Again we note that as needed all these results are finite and go to zero at large distances from the given gravitational source in question.

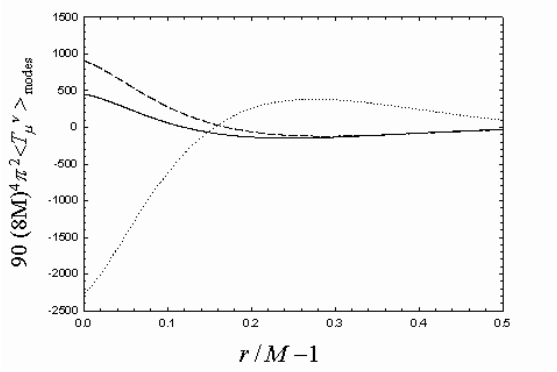

(a) The extreme Reissner-Nordström black hole.

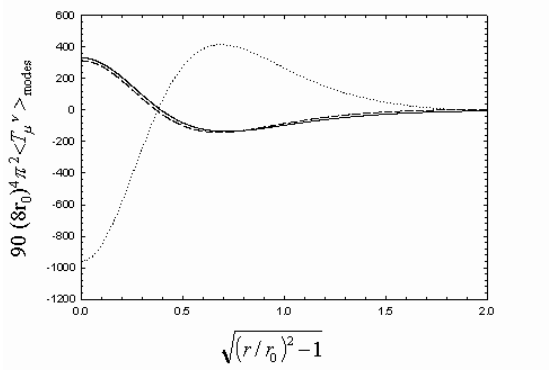

(b) The zero radial tides wormhole.

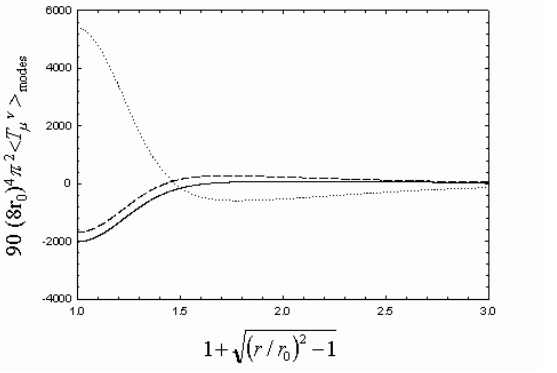

(c) The simple wormhole.

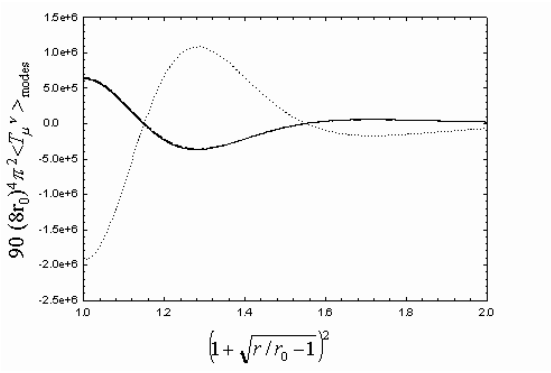

(d) The proximal Schwarzschild wormhole.

Figure 3.13: The modes contribution to the full stress-energy tensor for the massless spin one-half field for the extreme Reissner-Nordström and the three wormhole spacetimes studied. In all figures a solid line, dotted line, and a dashed line are $\langle T_t{}^t(x)\rangle_{\rm modes}$, $\langle T_r{}^r(x)\rangle_{\rm modes}$, and $\langle T_\theta{}^\theta(x)\rangle_{\rm modes} = \langle T_\phi{}^\phi(x)\rangle_{\rm modes}$ respectively.

3.5 Results for $\langle T_\mu{}^\nu(x)\rangle_{\rm ren}$ and $\langle T_\mu{}^\nu(x)\rangle_{\rm analytic}$ for the extreme Reissner-Nordström black hole

With all relevant quantities now discussed, we are now ready to form the full stress-energy tensor for the massless spin one-half field via the earlier expression

$$\langle T_{\mu\nu}(x)\rangle_{\rm ren} = \langle T_{\mu\nu}(x)\rangle_{\rm modes} + \langle T_{\mu\nu}(x)\rangle_{\rm WKBfin} + \langle T_{\mu\nu}(x)\rangle_{\rm analytic}. \tag{3.85}$$

Our results for all nonzero components of $\langle T_\mu{}^\nu\rangle_{\rm ren}$ and $\langle T_\mu{}^\nu\rangle_{\rm analytic}$ are displayed in Fig. 3.15. All components of $\langle T_\mu{}^\nu\rangle_{\rm ren}$ were computed to at least ten decimal places and were finite at all distances, including the event horizon. Recall that a divergence in one of its components may imply that the black hole metric breaks down. Notice that the analytic approximation is very poor indeed, not even producing the correct sign for

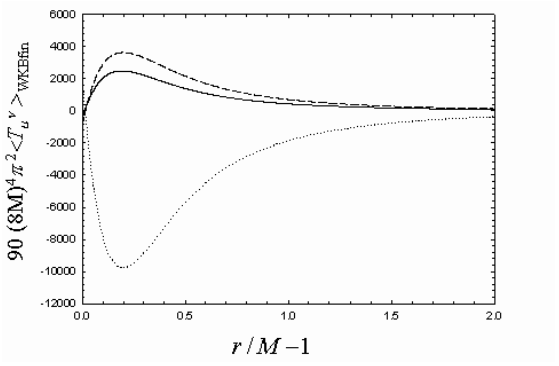

(a) The extreme Reissner-Nordström black hole.

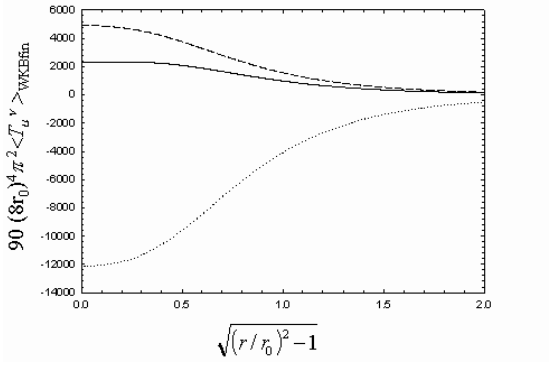

(b) The zero radial tides wormhole.

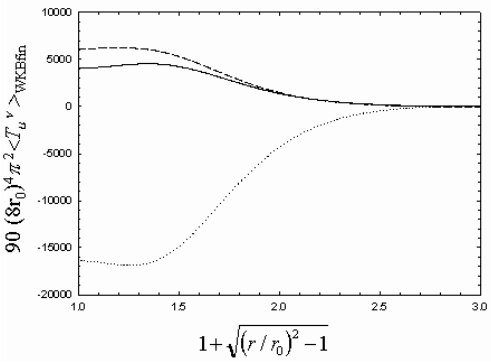

(c) The simple wormhole.

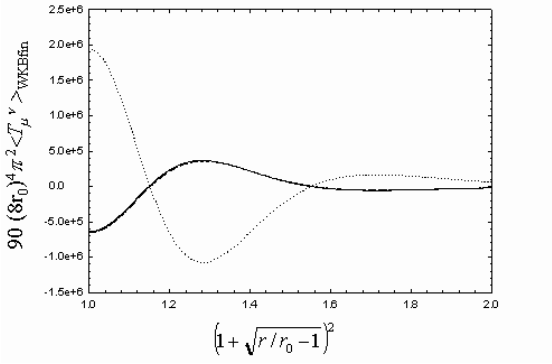

(d) The proximal Schwarzschild wormhole.

Figure 3.14: The WKBfin contribution to the full stress-energy tensor for the massless spin one-half field for the extreme Reissner-Nordström and the three wormhole spacetimes studied. In all figures, a solid line, dotted line, and a dashed line are $\langle T_t{}^t(x)\rangle_{\rm WKBfin}$, $\langle T_r{}^r(x)\rangle_{\rm WKBfin}$, and $\langle T_\theta{}^\theta(x)\rangle_{\rm WKBfin} = \langle T_\phi{}^\phi(x)\rangle_{\rm WKBfin}$ respectively.

the components of $\langle T_\mu{}^\nu\rangle_{\rm ren}$ in the majority of distances from the event horizon shown. The analytic approximation gets the same value on the horizon for $\langle T_t{}^t\rangle$, $\langle T_r{}^r\rangle$, and $\langle T_\theta{}^\theta\rangle = \langle T_\phi{}^\phi\rangle$ as the renormalized calculation, but elsewhere it is in great error. At large distance, the analytic approximation approaches zero, but does not have the correct asymptotic behavior. The analytic approximation should give the exact result for a conformally flat spacetime such as ERN showing that the approximation is in great error. Note that the sign of $\langle T_t{}^t\rangle_{\rm ren}$ in Fig. 3.15(a) is positive for all distances meaning that the energy density is negative. This result adds to the list of violations of the weak energy condition due to quantum effects.

We also further validated our result for the energy density by comparing our result to data found by Carlson *et al.* for the Reissner-Nordström black hole in [33]. Figure

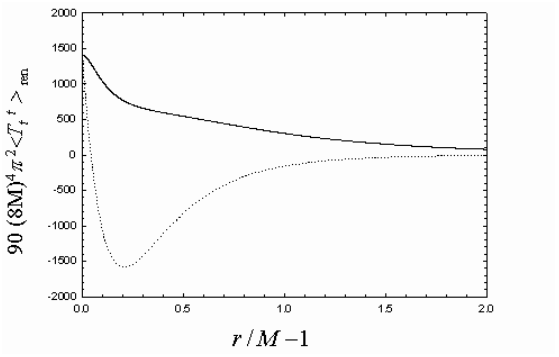

(a) $\langle T_t{}^t \rangle_{\rm ren}$ and $\langle T_t{}^t \rangle_{\rm analytic}$

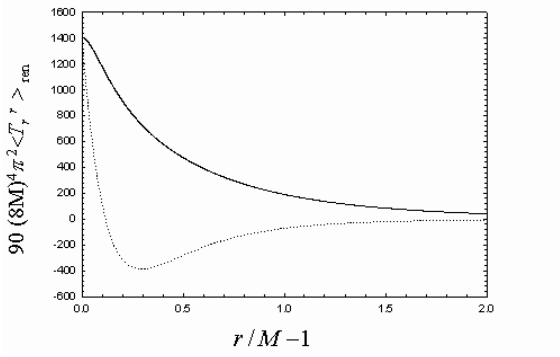

(b) $\langle T_r{}^r \rangle_{\rm ren}$ and $\langle T_r{}^r \rangle_{\rm analytic}$

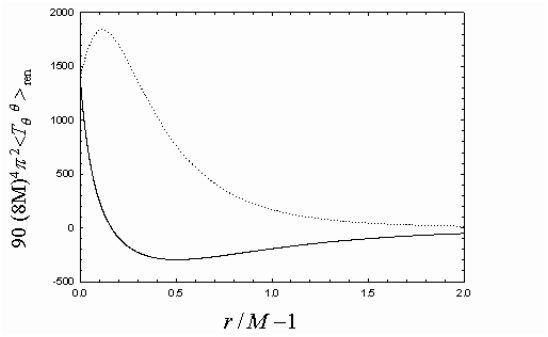

(c) $\langle T_\theta{}^\theta \rangle_{\rm ren}$ and $\langle T_\theta{}^\theta \rangle_{\rm analytic}$

Figure 3.15: The components of the full stress-energy tensor and the analytic approximation for the massless spin one-half field around the extreme Reissner-Nordström black hole plotted as a function of distance from the event horizon. In all figures a solid curve is the renormalized calculation, a dotted curve is the analytic approximation. Note that $\langle T_\phi{}^\phi \rangle = \langle T_\theta{}^\theta \rangle$ for both the renormalized and analytic calculation. The renormalization constant μ has been chosen so that $\mu M = 1$.

3.16 shows the steady progression of the RN result to ERN for increasing Q/M.

Carlson *et al.* also found the analytic approximation to be untrustworthy near the event horizon for the Schwarzschild and RN black hole [33]. My collaborators reported finding negative energy density on and near the event horizons. Our results are also in agreement with the calculations done by Anderson *et al.* for the massless scalar field [89] who found all components of the full stress-energy tensor to be regular on the event horizon of the ERN black hole. Also, the spin 1 field calculation by Jensen and Ottewill [79] in Schwarzschild spacetime is in contrast with our results, since they found that the analytic approximation was very good on and away from the event horizon.

We decided to investigate the large r structure of our numerical results for $\langle T_\mu{}^\nu \rangle_{\rm ren}$

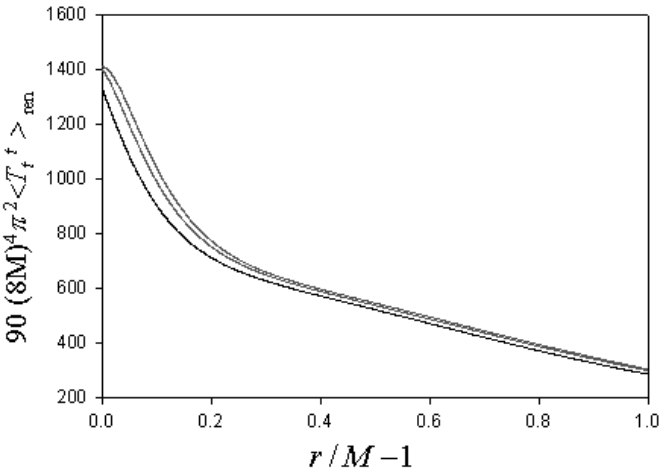

Figure 3.16: $\langle T_t{}^t \rangle_{\rm ren}$ for the massless spin one-half field around an extreme Reissner-Nordström black hole compared to data for the same calculation for a Reissner-Nordström black hole. From top to bottom the curves are $Q/M = 1.00, 0.9999, 0.999$.

for the ERN spacetime. After multiplying the results for the full stress-energy tensor for ERN by r^5/M, we obtain Fig. 3.17 and indeed find that far from the event horizon $\langle T_\mu{}^\nu \rangle_{\rm ren}$ is proportional to (M/r^5) with the curves levelling off. The curves in Fig. 3.17 were extended out to very large distances to ensure accuracy when performing a fifth order rational interpolation. We found for large r that:

$$\begin{aligned} 90\,(8M)^4\,\pi^2 \langle T_t{}^t \rangle_{\rm ren} &= a\frac{M}{r^5}, \\ 90\,(8M)^4\,\pi^2 \langle T_r{}^r \rangle_{\rm ren} &= b\frac{M}{r^5}, \\ 90\,(8M)^4\,\pi^2 \langle T_\theta{}^\theta \rangle_{\rm ren} &= c\frac{M}{r^5}, \end{aligned} \tag{3.86}$$

with $a \simeq 37600$, $b \simeq 18700$, and $c \simeq -28100$. Recently, Anderson *et al.* [41] numerically studied $\langle T_\mu{}^\nu \rangle_{\rm ren}$ for the massless scalar field in the Boulware state around a Schwarzschild black hole to see if they could reproduce the form of the gravitational potential Φ needed to prove the conjecture. The form of the stress-energy tensor needed is such that at large r it must fall off as M/r^5 as opposed to that given by the analytical approximation, namely M^2/r^6.

The last quantity of interest for our study of the ERN spacetime was to look at a component of the full stress-energy tensor that is related to the energy density observed by a freely falling observer approaching the event horizon. It is [33]

$$\frac{\langle T_r{}^r \rangle - \langle T_t{}^t \rangle}{f(r)}, \tag{3.87}$$

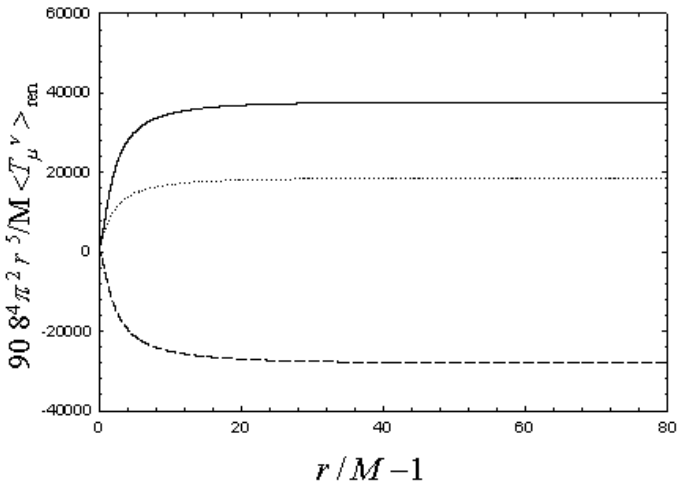

Figure 3.17: The previous results for the full stress-energy tensor for the massless spin one-half field around an extreme Reissner-Nordström black hole multiplied by r^5/M. From top to bottom the curves are $\langle T_t{}^t \rangle_{\rm ren}$, $\langle T_r{}^r \rangle_{\rm ren}$, and $\langle T_\theta{}^\theta \rangle_{\rm ren}$.

where $f(r)$ is the standard metric function from earlier for ERN. Trivedi found using two dimensional calculations of $\langle T_\mu{}^\nu \rangle_{\rm analytic}$ for the scalar field [32] a divergence of this quantity on the event horizon of the form

$$\frac{M^2(32M - 23r)}{180\pi^2 r^6 (r - M)}. \tag{3.88}$$

Also, the four dimensional analytic approximation predicts such a divergence. If this result were true it would very likely rule out the existence of the ERN spacetime. We find using the full renormalized calculation that the quantity in Eq. (3.87) is finite on the event horizon. This result is shown with the analytic prediction and a comparison to several Reissner-Nordström black hole spacetimes in Fig. 3.18. The results for the RN metric have been taken from the calculations done by Carlson and Obermayer [33]. Notice that the analytic approximation diverges at the event horizon while the renormalized calculation produces a finite value. Further validity of this result is indicated by the progression of the Reissner-Nordström result to ERN.

To check our results for $\langle T_\mu{}^\nu \rangle_{\rm ren}$ for ERN we calculated the trace anomaly and the total trace of our numerical answer. The two quantities were found to agree extremely well. This data appears in Fig. 3.19.

Next we checked the conservation condition $\nabla_\mu \langle T_\nu{}^\nu \rangle_{\rm ren} = 0$. This was done by expanding the covariant derivative of the full stress-energy tensor such that we arrived

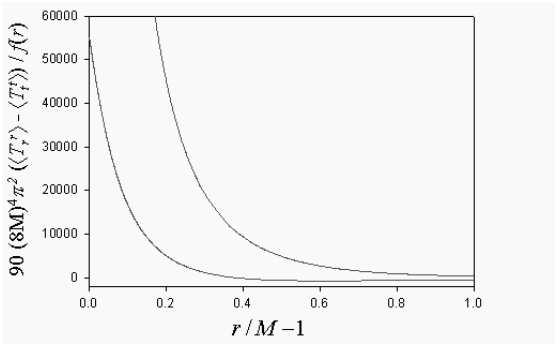

(a) The left curve utilizes $\langle T_\mu{}^\nu \rangle_{\rm ren}$ while the right utilizes $\langle T_\mu{}^\nu \rangle_{\rm analytic}$.

(b) From top to bottom the curves are $Q/M = 1.00, 0.9999, 0.999$.

Figure 3.18: The left graph shows the renormalized calculation and analytic approximation of $\frac{\langle T_r{}^r \rangle - \langle T_t{}^t \rangle}{f(r)}$ plotted for the extreme Reissner-Nordström spacetime. The right graph compares this same quantity for the extreme Reissner-Nordström spacetime to that of several Reissner-Nordström spacetimes.

at

$$\left[\partial_r + \frac{2}{r} + \frac{f'}{2f}\right] \langle T_r{}^r \rangle = \frac{f'}{2f} \langle T_t{}^t \rangle + \frac{2}{r} \langle T_\theta{}^\theta \rangle. \tag{3.89}$$

The left and right sides of Eq. (3.89) were then plotted and found to be in very good agreement, especially when close to the event horizon. This is depicted in Fig. 3.20. Note that the derivative appearing in Eq. (3.89) was computed numerically; the error in this procedure leads to the small region where the two curves do not exactly overlap in Fig. 3.20. The relative error in that region is about 0.01, elsewhere it is on the order of 10^{-9}. Specifically, this error is caused by the larger steps in r taken in this region while performing the numerical derivative.

3.6 Results for $\langle T_\mu{}^\nu(x) \rangle_{\rm ren}$ and $\langle T_\mu{}^\nu(x) \rangle_{\rm analytic}$ for the three wormhole spacetimes studied

We are now in a position to present and interpret our results for $\langle T_\mu{}^\nu \rangle_{\rm ren}$ for the three wormholes studied. These results appear in Figs. 3.21, 3.22, and 3.23 below along with those for the analytic approximation. For all of these plots we have implemented $\mu r_0 = 1$ for consistency, although we shall change its value when we look at the exotic energy condition. We again find that $\langle T_\mu{}^\nu \rangle_{\rm analytic}$ is not very useful. In contrast to ERN, the analytic approximation is wildly inaccurate at the throats of the zero radial

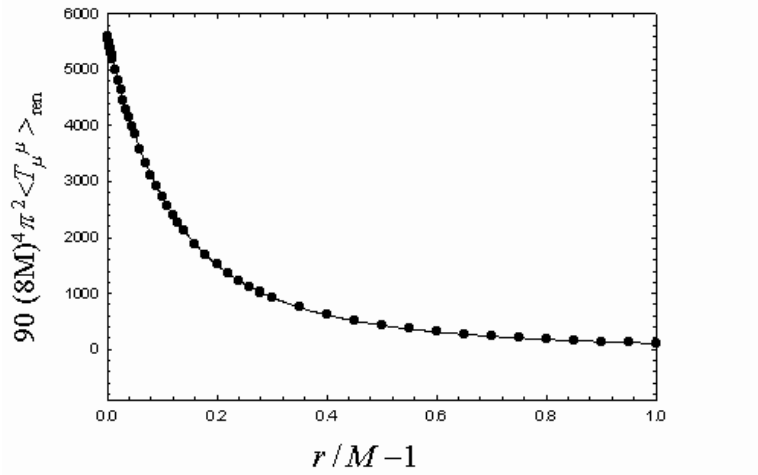

Figure 3.19: The trace of $\langle T_\mu{}^\nu \rangle_{\rm ren}$ and the trace anomaly for the extreme Reissner-Nordström black hole. The dotted line is the calculated trace anomaly and the solid line is $\langle T_\mu{}^\mu \rangle_{\rm ren}$.

tide and simple wormholes.

As in the ERN results, we also looked at the trace anomaly and the conservation of $\langle T_\mu{}^\nu \rangle_{\rm ren}$ to check these results. The trace anomaly was again found to be in excellent agreement with $\langle T_\mu{}^\mu \rangle_{\rm ren}$ as can be seen in Fig. 3.24. The conservation of the full stress-energy tensor was checked by plotting the left and right sides of Eq. 3.89 on the same graph for each wormhole studied. The results for the conservation of $\langle T_\mu{}^\nu \rangle_{\rm ren}$ were again satisfactory as can be seen in Figs. 3.25, 3.26, and 3.27.

After checking to see that our results were reliable, we wanted to see if for any of the wormholes studied satisfied the exotic energy condition

$$\tau_0 - \rho_0 > 0, \tag{3.90}$$

and the condition

$$\tau_0 > 0, \tag{3.91}$$

simultaneously for any values of the renormalization parameter μ to see if any wormhole geometry would be supported by quantum fluctuations of the massless spin one-half field. Using our sign conventions the energy density is $\rho = -\langle T_t{}^t \rangle$, and the radial tension is $\tau = -\langle T_r{}^r \rangle$. Note that τ must be positive by definition or it is instead a radial pressure. We recalculated $\langle T_\mu{}^\nu \rangle_{\rm ren}$ and $\langle T_\mu{}^\nu \rangle_{\rm analytic}$ for various values of μr_0 to see if a value existed where the exotic energy condition was met. These results appear in Figs. 3.28, 3.29, and 3.30 below. The data in these figures is such

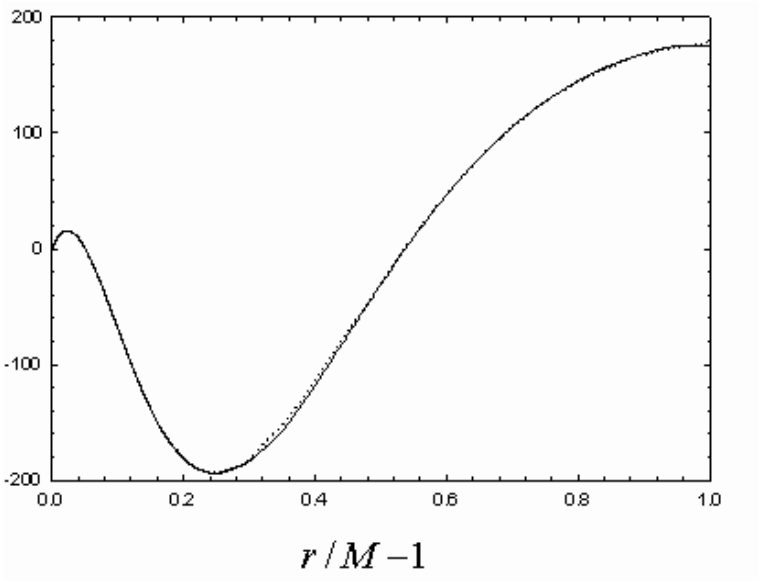

Figure 3.20: The conservation of $\langle T_\mu{}^\nu \rangle_{\rm ren}$ for the extreme Reissner-Nordström black hole. $\nabla_\nu \langle T_\mu{}^\nu \rangle_{\rm ren}$ has been expanded such that the solid line and dotted line are the left and right sides of Eq. (3.89) respectively.

that to have a self-consistent wormhole solution a single value of μr_0 must exist such that both plotted quantities are positive. This leads us to our major numerical result for all three wormhole spacetimes analyzed. The exotic energy condition can not be met for any value of μr_o for the full renormalized calculation. Even the analytic approximation only makes the wrong prediction once; specifically, in the case of the zero radial tides wormhole. These results are discouraging to attempts to find self-consistent solutions. None of our results satisfy the two inequalities given in Eqs. (3.90) and (3.91) simultaneously that must be met to obtain a self-consistent solution to the semi-classical Einstein equations.

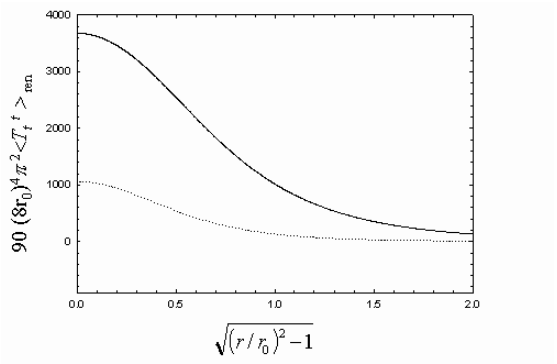

(a) $\langle T_t{}^t\rangle_{\rm ren}$ and $\langle T_t{}^t\rangle_{\rm analytic}$

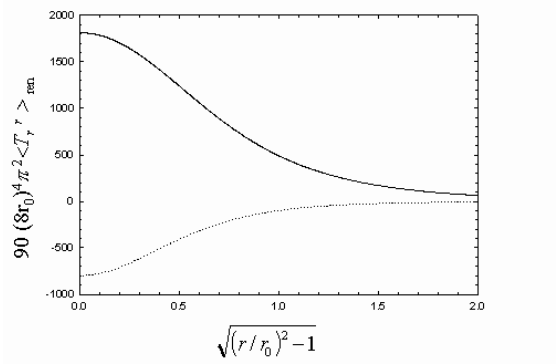

(b) $\langle T_r{}^r\rangle_{\rm ren}$ and $\langle T_r{}^r\rangle_{\rm analytic}$

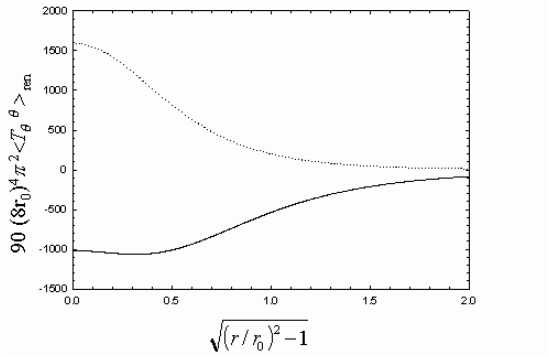

(c) $\langle T_\theta{}^\theta\rangle_{\rm ren}$ and $\langle T_\theta{}^\theta\rangle_{\rm analytic}$

Figure 3.21: The components of the full stress-energy tensor and the analytic approximation for the massless spin one-half field around the zero radial tide wormhole plotted as a function of distance from the throat for $\mu r_0 = 1$. In all figures a solid curve is the renormalized calculation, a dotted curve is the analytic approximation.

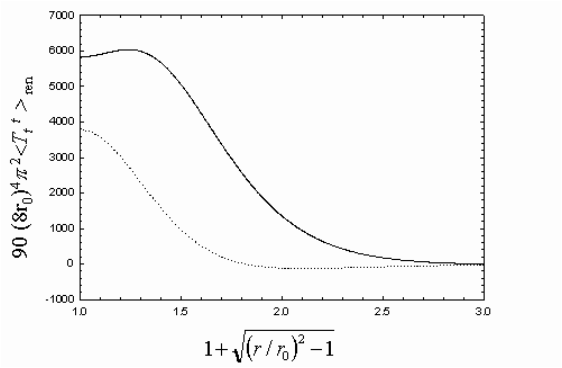

(a) $\langle T_t{}^t\rangle_{\rm ren}$ and $\langle T_t{}^t\rangle_{\rm analytic}$

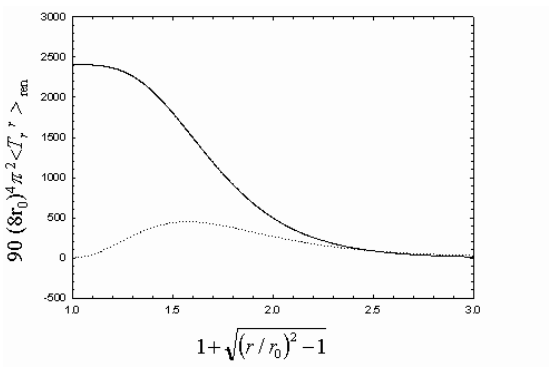

(b) $\langle T_r{}^r\rangle_{\rm ren}$ and $\langle T_r{}^r\rangle_{\rm analytic}$

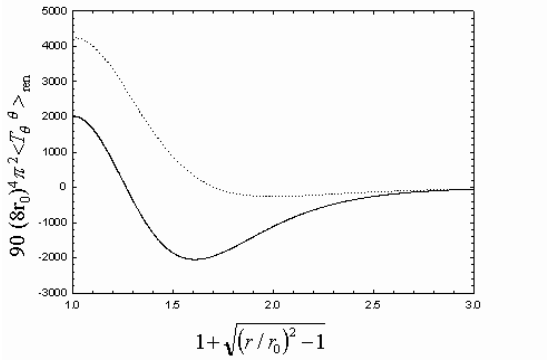

(c) $\langle T_\theta{}^\theta\rangle_{\rm ren}$ and $\langle T_\theta{}^\theta\rangle_{\rm analytic}$

Figure 3.22: The components of the full stress-energy tensor and the analytic approximation for the massless spin one-half field around the simple wormhole plotted as a function of distance from the throat for $\mu r_0 = 1$. In all figures a solid curve is the renormalized calculation, a dotted curve is the analytic approximation.

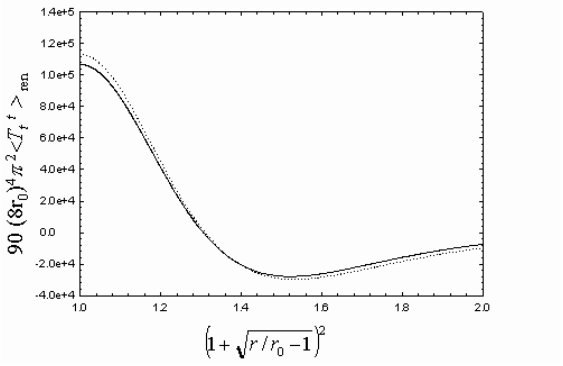

(a) $\langle T_t{}^t\rangle_{\rm ren}$ and $\langle T_t{}^t\rangle_{\rm analytic}$

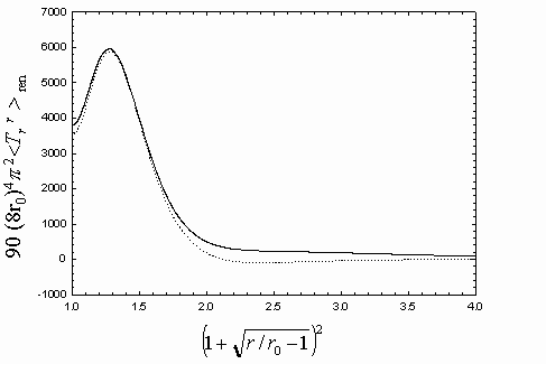

(b) $\langle T_r{}^r\rangle_{\rm ren}$ and $\langle T_r{}^r\rangle_{\rm analytic}$

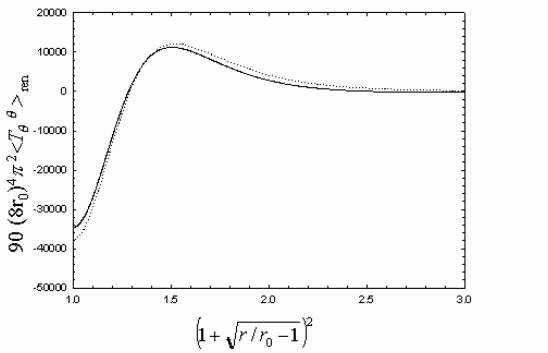

(c) $\langle T_\theta{}^\theta\rangle_{\rm ren}$ and $\langle T_\theta{}^\theta\rangle_{\rm analytic}$

Figure 3.23: The components of the full stress-energy tensor and the analytic approximation for the massless spin one-half field around the proximal Schwarzschild wormhole plotted as a function of distance from the throat for $\mu r_0 = 1$. In all figures a solid curve is the renormalized calculation, a dotted curve is the analytic approximation.

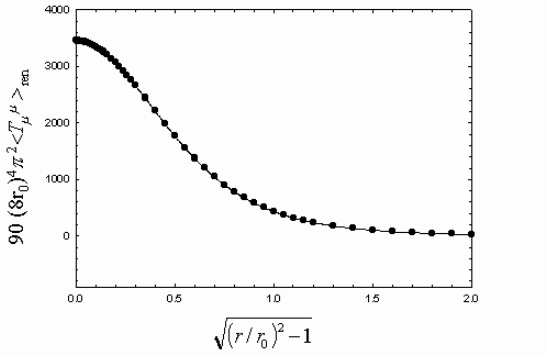

(a) The zero radial tide wormhole.

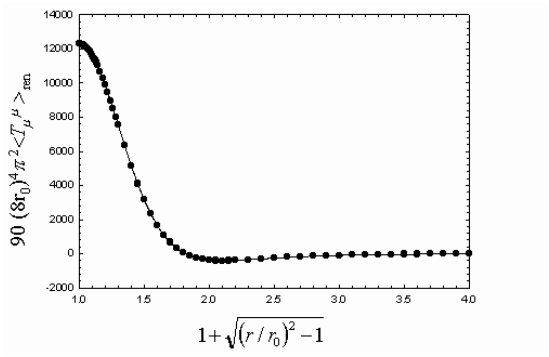

(b) The simple wormhole.

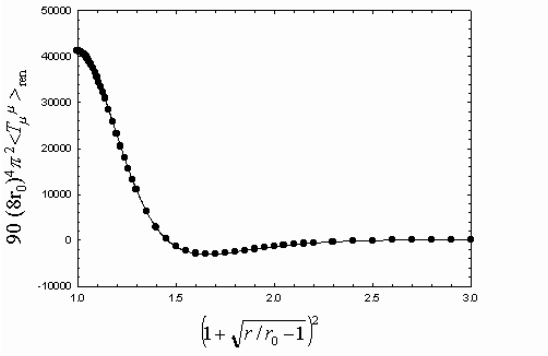

(c) The proximal Schwarzschild wormhole.

Figure 3.24: The trace of $\langle T_\mu{}^\nu \rangle_{\rm ren}$ and the trace anomaly for the three wormhole metrics studied. The dotted line in each graph is the calculated trace anomaly and the solid line is $\langle T_\mu{}^\mu \rangle_{\rm ren}$.

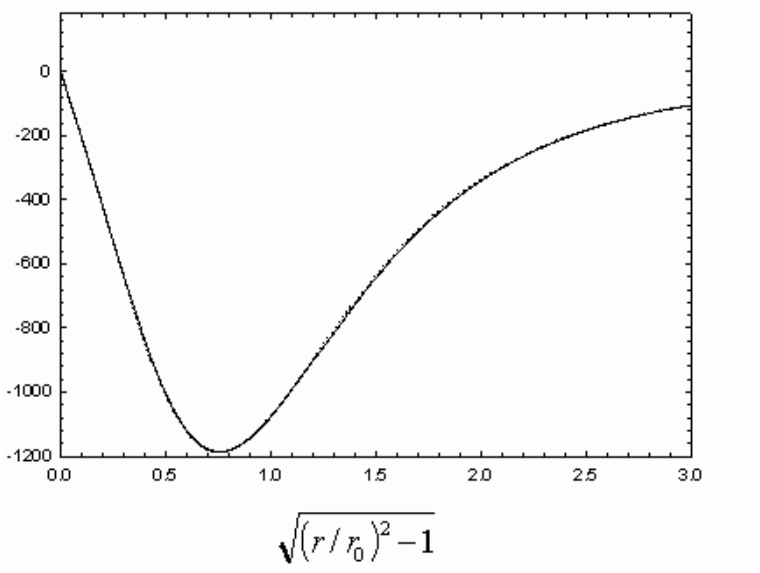

Figure 3.25: The conservation of $\langle T_\mu{}^\nu \rangle_{\rm ren}$ for the zero radial tide wormhole. $\nabla_\nu \langle T_\mu{}^\nu \rangle_{\rm ren}$ has been expanded such that the solid line and dotted line are the left and right sides of Eq. (3.89) respectively.

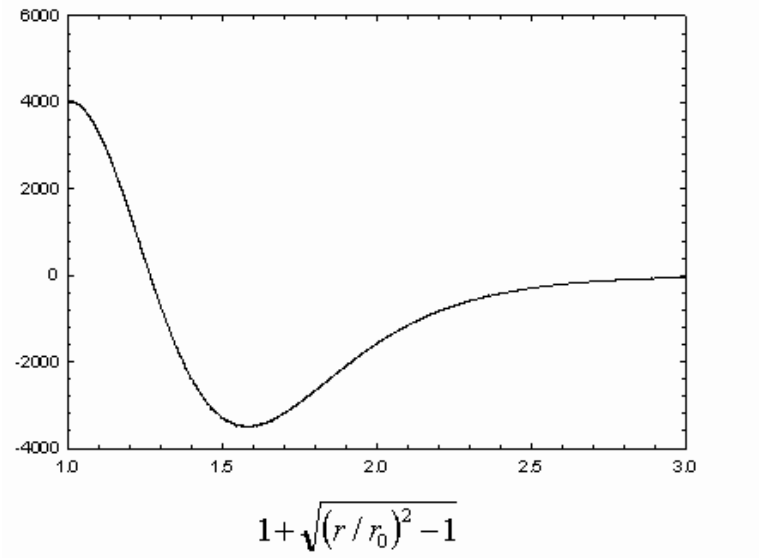

Figure 3.26: The conservation of $\langle T_\mu{}^\nu \rangle_{\rm ren}$ for the simple wormhole. $\nabla_\nu \langle T_\mu{}^\nu \rangle_{\rm ren}$ has been expanded such that the solid line and dotted line are the left and right sides of Eq. (3.89) respectively.

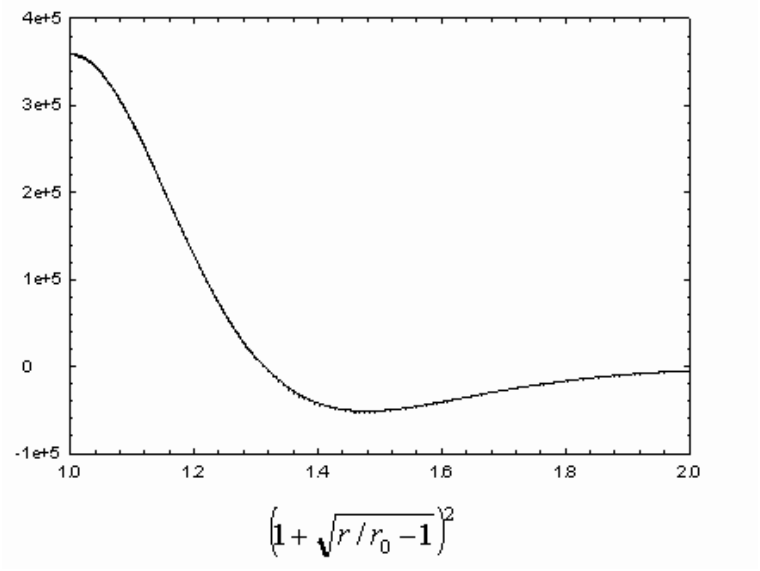

Figure 3.27: The conservation of $\langle T_\mu{}^\nu \rangle_{\rm ren}$for the proximal Schwarzschild wormhole. $\nabla_\nu \langle T_\mu{}^\nu \rangle_{\rm ren}$ has been expanded such that the solid line and dotted line are the left and right sides of Eq. (3.89) respectively.

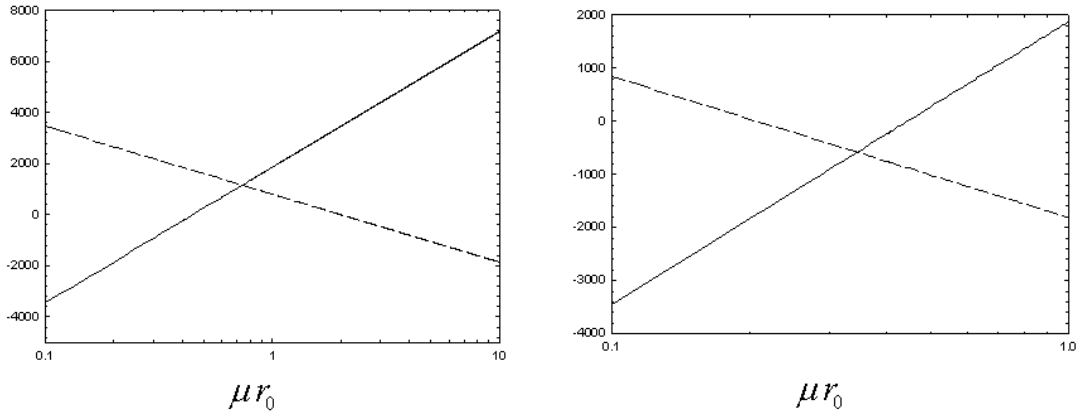

(a) The analytic results.

(b) The renormalized results.

Figure 3.28: The study of the exotic energy condition utilizing τ and $\tau - \rho$ as a function of μr_0 on a logarithmic scale at the throat of the zero radial tide wormhole. The dashed and solid curves are τ and $\tau - \rho$ respectively. To have a self-consistent wormhole solution a single value of μr_0 must exist such that both plotted quantities are positive.

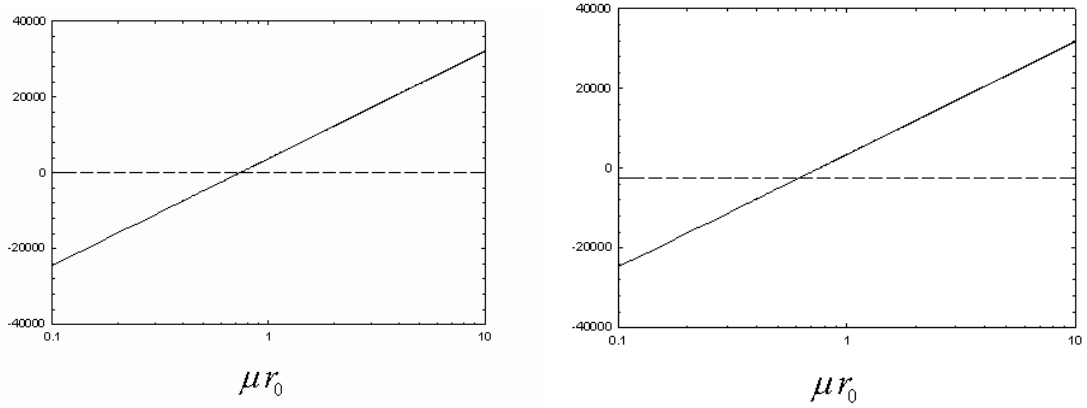

(a) The analytic results. (b) The renormalized results.

Figure 3.29: The study of the exotic energy condition utilizing τ and $\tau - \rho$ as a function of μr_0 on a logarithmic scale at the throat of the simple wormhole. The dashed and solid curves are τ and $\tau - \rho$ respectively. Note that in the analytic case $\tau - \rho$ is of order 10^{-6} and not zero. To have a self-consistent wormhole solution a single value of μr_0 must exist such that both plotted quantities are positive.

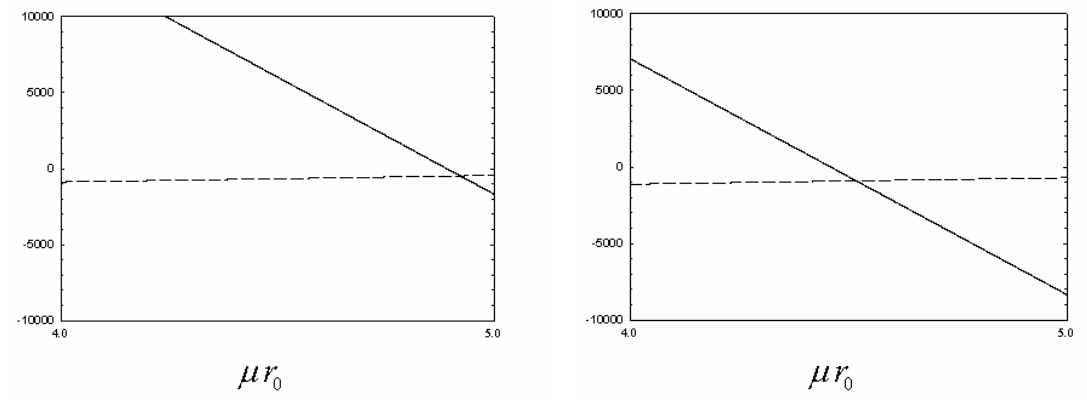

(a) The analytic results. (b) The renormalized results.

Figure 3.30: The study of the exotic energy condition utilizing τ and $\tau - \rho$ as a function of μr_0 on a logarithmic scale at the throat of a proximal Schwarzschild wormhole. The dashed and solid curves are τ and $\tau - \rho$ respectively. To have a self-consistent wormhole solution a single value of μr_0 must exist such that both plotted quantities are positive.

Chapter 4

Conclusion

4.1 $\langle T_\mu{}^\nu \rangle_{\rm ren}$ in general

The full renormalized stress-energy tensors for the extreme Reissner-Nordström black hole and the zero radial tides, simple, and proximal Schwarzschild wormholes have been successfully calculated. All components of $\langle T_\mu{}^\nu \rangle_{\rm ren}$ were found to be finite on and outside of the event horizon of the ERN black hole, and were computed to at least ten digits. Also, the full stress-energy tensor for all wormholes studied was determined to be finite everywhere including the throat. In addition, all results for $\langle T_\mu{}^\nu \rangle_{\rm ren}$ were shown to satisfy the trace anomaly and conservation conditions. The utilization of only the analytic portion of the full stress-energy tensor as an approximation was determined to be very inaccurate in general when compared to its use in conjunction with a full renormalized calculation. We find that using only the analytic portion of the full stress-energy tensor produces results that very often even have the sign wrong. It only predicts correct values of $\langle T_t{}^t \rangle_{\rm ren}$, $\langle T_r{}^r \rangle_{\rm ren}$, and $\langle T_\theta{}^\theta \rangle_{\rm ren} = \langle T_\phi{}^\phi \rangle_{\rm ren}$ on the event horizon of the ERN spacetime. It did, however, succeed in predicting that quantum fluctuations of the massless spin one-half field would make two of the three wormholes (simple and proximal Schwarzschild) studied not self-consistent. Also, the energy density close to the event horizon of the ERN black hole and throats of the wormholes was found to be negative, violating the weak energy condition.

4.2 The extreme Reissner-Nordström black hole

The extreme Reissner-Nordström black hole calculations lead to some interesting results. A previous prediction of a renormalized calculation by Trivedi in two dimensions

[32] for the massless scalar field finds that the component that is related to the energy density observed by a freely falling observer approaching the event horizon diverges. This divergence is also predicted for ERN black hole by various analytic approximations for the massless spin 0, 1/2, and 1 fields [23, 26, 33]. Our results indicate that all components of the full stress-energy tensor are actually finite on the event horizon in contrast to the above predictions, but in agreement with full numerical results for the stress-energy tensor for the massless spin-0 field [26]. All of these calculations were also in agreement with previous work done for the Reissner-Nordström black hole in the limit $Q/M \to 1$ [33]. In addition, at large distances all components of the full stress-energy tensor were shown to be proportional to M/r^5.

4.3 Wormholes

Even though negative energy density was found close to the throat of each wormhole studied, the components determined for $\langle T_\mu{}^\nu \rangle_{\rm ren}$ for each wormhole could not simultaneously satisfy the exotic energy condition inequality

$$\tau_0 - \rho_0 > 0, \tag{4.1}$$

and the condition

$$\tau_0 > 0, \tag{4.2}$$

required for a self-consistent solution. Our results are similar to those previously found by Anderson *et al.* [34] who, for the same wormholes studied in this work, utilized an analytic approximation for the full stress-energy tensor for the massless minimally and conformally coupled scalar field. They found the stress-energy tensor failed to satisfy the exotic energy condition for minimal and covariant coupling. These results are discouraging to attempts to find self-consistent solutions to the semi-classical Einstein equations for the wormholes under study.

Bibliography

[1] S.W. Hawking and W. Israel. *'Introductory Survey' in General Relativity: An Einstein Centenary Survey.* Cambridge University Press, 1979.

[2] B.S. DeWitt. *Phys. Rev.*, 162:1834, 1967.

[3] R.P. Feynman. *Acta. Phys. Polon.*, 24:697, 1963.

[4] L.D. Faddeev and V.N. Popov. Feynman diagrams for the Yang-Mills field. *Phys. Lett. B*, 25:29, 1967.

[5] M.J. Duff. *'Covarient Quantization in Quantum Gravity,' in Quantum Gravity: An Oxford Symposium.* Oxford University Press, 1975.

[6] S. Weinberg. *'Ultraviolet Divergences in Quantum Theories of Gravitation' in General Relativity: An Einstein Centenary Survey.* Cambridge University Press, 1979.

[7] G. 't Hooft. An algorithm for the poles at dimension four in the dimensional regularization procedure. *Nucl. Phys. B*, 62:444, 1973.

[8] G. 't Hooft and M. Veltman. *Ann. Inst. Poincare*, 20:69, 1974.

[9] S. Deser and P. van Nieuwenhuizen. Nonrenormalizability of the quantized Einstein-Maxwell system. *Phys. Rev. Lett.*, 32:245, 1974.

[10] S. Deser and P. van Nieuwenhuizen. One-loop divergences of quantized Einstein-Maxwell fields. *Phys. Rev. D*, 10:401, 1974.

[11] S. Deser, H-S Tsao, and P. van Nieuwenhuizen. *Phys. Lett. B*, 50:491, 1974.

[12] L.M. Brown. *Renormalization: From Lorentz to Landau.* Springer-Verlog, 1993.

[13] B. Greene. *The Elegant Universe : Superstrings, Hidden Dimensions, and the Quest for the Ultimate Theory.* W.W. Norton and Co., 2003.

[14] L. Smolin. *The Trouble With Physics: The Rise of String Theory, the Fall of a Science, and What Comes Next.* Houghton Mifflin, 2006.

[15] A. Ashtekar. Quantum geometry and gravity: Recent advances. *LANL*, arXiv:gr-qc/0112038v1:24 pgs, 2001.

[16] P. Brax and C. Bruck. *Class. Quant. Grav.*, 20:201, 2003.

[17] J. Wess and J. Bagger. *Supersymmetry and Supergravity.* Princeton University Press, 1992.

[18] A. Ashtekar. The winding road to quantum gravity. *Current Science*, 89:2064, 2005.

[19] C.W. Misner, K.S. Thorne, and J.A. Wheeler. *Gravitation.* W. H. Freeman and Co., 1982.

[20] H. Reissner. *Ann. Phys. (Germany)*, 50:106, 1916.

[21] G. Nordström. On the energy of the gravitational field in Einstein's theory. *Proc. Kon. Ned. Akad. Wet.*, 20:1238, 1918.

[22] B. Carter. *Phys. Lett.*, 21:423, 1966.

[23] V.P. Frolov and A.I. Zel'nikov. *Phys. Rev. D*, 35:3031, 1987.

[24] T. Zannias. *Phys. Rev. D*, 30:1161, 1984.

[25] C. Huang. *Phys. Lett. A*, 164:384, 1992.

[26] P. R. Anderson, W. A. Hiscock, and D.J. Loranz. *Phys. Rev. Lett.*, 74:4365, 1995.

[27] M.S. Morris and K.S. Thorne. Wormholes in spacetime and their use for interstellar travel: a tool for teaching general relativity. *Am. J. Phys.*, 56:395, 1988.

[28] E. Tomboulis. *Phys. Lett. B*, 70:361, 1977.

[29] D. Hochberg, A. Popov, and S. Sushkov. *Phys. Rev. Lett.*, 78:2050, 1997.

[30] P.B. Groves, P.R. Anderson, and E.D. Carlson. Method to compute the stress-energy tensor for the massless spin 1/2 field in a general static spherically symmetric spacetime. *Phys. Rev. D*, 66:124017, 2002.

[31] N.D. Birrell and P.C.W. Davies. *Quantum Fields in Curved Space*. Cambridge University Press, 1982.

[32] S.P. Trivedi. *Phys. Rev. D*, 47:4233, 1993.

[33] E.D. Carlson, W.H. Hirsch, B. Obermayer, P.R. Anderson, and P.B. Groves. Stress-energy tensor for a massless spin 1/2 field in static black hole spacetimes. *Phys. Rev. Lett.*, 91:051301, 2003.

[34] B.E. Taylor, W.A. Hiscock, and P.R. Anderson. Stress-energy of a quantized scalar field in static wormhole spacetimes. *Phys. Rev. D*, 55:6116, 1997.

[35] N.R. Khusnutdinov and S.V. Sushkov. *Phys. Rev. D*, 65:084028, 2002.

[36] A.A. Popov. *Phys. Rev. D*, 64:104005, 2001.

[37] C. Barcelo and M. Visser. *Class. Quant. Grav.*, 17:3843, 2000.

[38] S. Weinberg. *Gravitation and Cosmology: Principles and Applications of the General Theory of Relativity*. John Wiley and Sons, Inc., 1972.

[39] R. Penrose. *'The Question of Cosmic Censorship' in Black Holes and Relativistic Stars, ed. R. Wald*. University of Chicago Press, 1994.

[40] A. Chamblin, H.S. Reall, H. Shinkai, and T. Shiromizu. Charged brane-world black holes. *Phys. Rev. D*, 63:064015, 2001.

[41] P.R. Anderson, R. Balbinot, and A. Fabbri. Cutoff antide sitter space/conformal-field-theory duality and the quest for braneworld black holes. *Phys. Rev. Lett.*, 94:061301, 2005.

[42] N. Hambli. More on four-dimensional extremal black holes. *Phys. Rev. D*, 54:5129, 1996.

[43] A. Einstein and N. Rosen. The particle problem in the general theory of relativity. *Phys. Rev.*, 48:73, 1935.

[44] R.W. Fuller and J.A. Wheeler. *Phys. Rev.*, 128:919, 1962.

[45] J.A. Wheeler. *Geometrodynamics*. Academic Press, 1962.

[46] M. Visser. *Lorentzian Wormholes: From Einstein to Hawking*. American Institute of Physics, 1995.

[47] F. Lobo. *Cassical and Quantum Gravity Research Progress*. Nova Science, 2008.

[48] S.W. Hawking and G.F.R. Ellis. *The Large Scale Structure of Space-time*. Cambridge University Press, 1973.

[49] L.H. Ford and T.A. Roman. *Phys. Rev. D*, 53:5496, 1996.

[50] B.S. DeWitt. Quantum field theory in curved spacetime. *Phys. Rep.*, 19:296, 1975.

[51] R.M. Wald. *Quantum Field Theory in Curved Spacetime and Black Hole Thermodynamics*. University of Chicago Press, 1994.

[52] S.A. Fulling. *Aspects of Quantum Field Theory in Curved Space-time*. Cambridge University Press, 1989.

[53] L.H. Ford. Quantum field theory in curved spacetime. *LANL*, arXiv:gr-qc/9707062v1:44 pgs, 1997.

[54] T. Jacobson. Introduction to quantum fields in curved spacetime and the Hawking effect. *LANL*, arXiv:gr-qc/0308048v1:59 pgs, 2003.

[55] M. Bander and C. Itzykson. Group theory and the hydrogen atom (II). *Rev. Mod. Phys.*, 38:346, 1966.

[56] J.S. Dowker and R. Critchley. Scalar effective lagrangian in de Sitter space. *Phys. Rev. D*, 13:224, 1976.

[57] J.S. Dowker and R. Critchley. Effective lagrangian and energy-momentum tensor in de Sitter space. *Phys. Rev. D*, 13:3224, 1976.

[58] G. Grensing. Quantized fields over de Sitter space. *J. Phys. A: Gen. Phys.*, 10:1687, 1977.

[59] N.D. Birrell. Stress tensor conformal anomaly for Weinberg-type fields in curved spacetimes. *J. Phys. A: Gen. Phys.*, 12:337, 1979.

[60] S.W. Hawking. Particle creation by black holes. *Commun. Math. Phys.*, 43:199, 1975.

[61] J.S. Schwinger. On gauge invariance and vacuum polarization. *Phys. Rev.*, 82:664, 1951.

[62] H.B.G. Casimir. On the attraction between two perfectly conducting plates. *Proceedings of the Royal Netherlands Academy of Arts and Sciences*, 51:793, 1948.

[63] H.B.G. Casimir and D. Polder. The influence of retardation on the London-van der Waals forces. *Phys. Rev.*, 73:360, 1948.

[64] S.K. Lamoreaux. *Phys. Rev. Lett.*, 78:5, 1997.

[65] R. Balian and B. Duplantier. *Ann. Phys.*, 104:300, 1977.

[66] R. Balian and B. Duplantier. *Ann. Phys.*, 112:165, 1978.

[67] W.G. Unruh. Notes on black hole evaporation. *Phys. Rev. D*, 14:870, 1976.

[68] N.N. Bogolubov. *Zh. Eksp. Teor. Fiz.*, 34:58, 1958.

[69] R. Mueller. Decay of accelerated particles. *Phys. Rev. D*, 56:953, 1997.

[70] L.I. Schiff. *Quantum Mechanics*. McGraw-Hill, 1949.

[71] S.M. Christensen. Vacuum expectation value of the stress tensor in an arbitrary curved background: The covariant point-separation method. *Phys. Rev. D*, 14:2490, 1976.

[72] S.M. Christensen. Regularization, renormalization, and covariant geodesic point separation. *Phys. Rev. D*, 17:946, 1978.

[73] R.M. Wald. *Commun. Math. Phys.*, 45:9, 1977.

[74] C. Itzykson and J. Zuber. *Quantum Field Theory*. McGraw-Hill Inc., 1980.

[75] J.D. Bjorken and S.D. Drell. *Relativistic Quantum Fields*. McGraw-Hill, 1965.

[76] B. Thaller. *The Dirac Equation*. Springer-Verlag, 1992.

[77] P. Candelas. *Phys. Rev. D*, 21:2185, 1980.

[78] K.W. Howard and P. Candelas. *Phys. Rev. Lett.*, 53:403, 1984.

[79] B.P. Jensen and A. Ottewill. Renormalized electromagnetic stress tensor in Schwarzschild spacetime. *Phys. Rev. D*, 39:1130, 1989.

[80] M.R. Brown, A.C. Ottewill, and D.N. Page. *Phys. Rev. D*, 33:2840, 1986.

[81] J. Matyjasek. *Phys. Rev. D*, 71:27504, 2005.

[82] S.M. Christensen. *Ph.D. dissertation*. University of Texas at Austin, unpublished, 1975.

[83] M.J. Duff. *Nucl. Phys. B*, 125:334, 1977.

[84] S.M. Christensen and M.J. Duff. *Phys. Lett. B*, 76:571, 1978.

[85] S.M. Christensen and M.J. Duff. *Nucl. Phys. B*, 154:301, 1979.

[86] S.M. Christensen and M.J. Duff. *Nucl. Phys. B*, 170:480, 1980.

[87] W.H. Press, B.P. Flannery, S.A. Teukolsky, and W.T. Vetterling. *Numerical Recipes: The Art of Scientific Computing*. Cambridge University Press, 1986.

[88] C.H. Edwards and D.E. Penney. *Calculus with Analytic Geometry*. Prentice Hall, 1995.

[89] P.R. Anderson, W.A. Hiscock, and D.A. Samuel. *Phys. Rev. D*, 51:4337, 1995.

[90] P.R. Anderson, W.A. Hiscock, and D.A. Samuel. *Phys. Rev. Lett.*, 70:1739, 1993.